ABSTRACT

Title of dissertation: SYNCHRONIZATION OF NETWORK
                           COUPLED CHAOTIC AND OSCILLATORY
                           DYNAMICAL SYSTEMS

                           Gilad Barlev, Doctor of Philosophy, 2013

Dissertation directed by: Professor Edward Ott
                           Department of Physics

We consider various problems relating to synchronization in networks of coupled oscillators. In Chapter 2 we extend a recent exact solution technique developed for all-to-all connected Kuramoto oscillators to certain types of networks by considering large ensembles of system realizations. For certain network types, this description allows for a reduction to a low dimensional system of equations. In Chapter 3 we compute the Lyapunov spectrum of the Kuramoto model and contrast our results both with the results of other papers which studied similar systems and with those we would expect to arise from a low dimensional description of the macroscopic system state, demonstrating that the microscopic dynamics arise from single oscillators interacting with the mean field. Finally, Chapter 4 considers an adaptive coupling scheme for chaotic oscillators and explores under which conditions the scheme is stable, as well as the quality of the stability.

SYNCHRONIZATION OF NETWORK COUPLED CHAOTIC AND OSCILLATORY DYNAMICAL SYSTEMS

by

Gilad Barlev

Dissertation submitted to the Faculty of the Graduate School of the
University of Maryland, College Park in partial fulfillment
of the requirements for the degree of
Doctor of Philosophy
2013

Advisory Committee:
Professor Edward Ott, Chair/Advisor
Professor Rajarshi Roy
Professor Michelle Girvan
Professor Thomas Antonsen
Professor Thomas Murphy

Dedication

For Jen, who reminds me why I do this work, who puts it in perspective, and who gives me something to look forward to at the end of each day.

Acknowledgments

Table of Contents

List of Figures

vii

Chapter 1:   Introduction

Synchronization is an important behavior in systems of coupled units. Some-times, as in communications, it is desirable for multiple units to behave in a coor-dinated fashion. In other circumstances, such collective behavior in large systems can be disastrous, as in epileptic seizures. The Kuramoto model is perhaps the simplest system used to study synchronization in large populations, and it is the focus of Chapters 2 and 3. Chapter 4 analyzes the stability of an adaptive method for synchronizing chaotic oscillators. This is done through use of a Master Stability Function which relies on Lyapunov analysis, which is also used to characterize the microscopic behavior of the Kuramoto model in Chapter 3.

1.1   The Kuramoto Model and Order

The Kuramoto model is a simple phase oscillator model in which each oscillator i in a system of N oscillators is represented by a phase angle θ_i, with dynamics given by

$$\frac{d\theta_j(t)}{dt} = \omega_j + \frac{k}{N} \sum_{j=1}^{N} \sin\left(\theta_j(t) - \theta_i(t)\right), \tag{1.1}$$

with each oscillator having its own so-called "natural frequency" ω_i which gives the rate at which the oscillator evolves in the absence of coupling ($k = 0$). This system
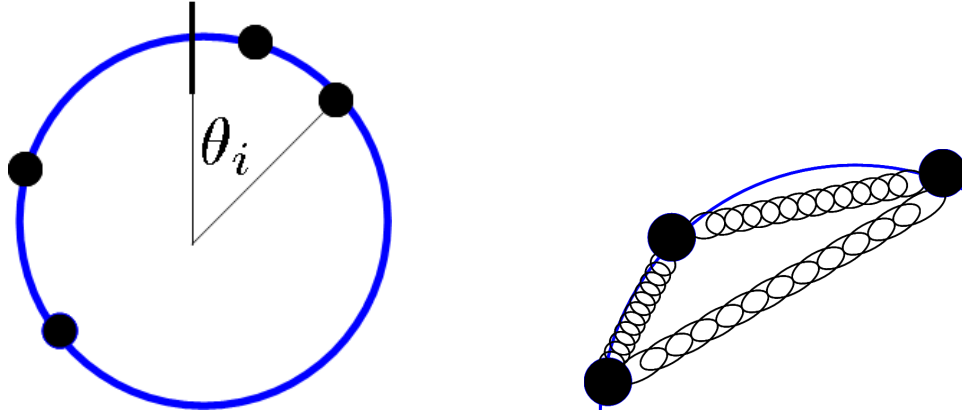
Figure 1.1: The Kuramoto model is often visualized as beads on a ring, coupled by an attractive pseudo-force whose magnitude is proportional to the distance between the oscillators.

is commonly visualized, as shown in Fig. 1.1, by picturing identical beads confined to a ring and coupled by an attractive "force" (Eq. (1.1) is a set of *first*-order ODEs) whose magnitude grows in proportion to the distance between the oscillators.

This thesis will primarily focus on systems where the number of oscillators N is large, $N >> 1$, in which case the collective dynamics of the system, which depend on the selection of natural frequencies $\{\omega_j\}$ and the overall coupling strength k, are of interest. To that end, we will make use of the system's "order parameter," a global measure of synchrony, defined as

$$R \equiv \frac{1}{N} \sum_{j=1}^{N} e^{i\theta_j}.$$

(1.2)

Returning to our picture of beads on a ring, if that ring has radius 1, then the magnitude of the order parameter will be the distance from the center of the ring to the center of mass of the collection of beads, as shown in Fig. 1.2. The magnitude
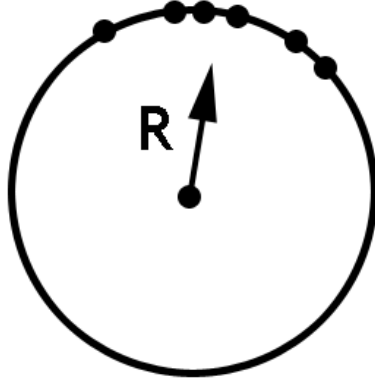
Figure 1.2: The order parameter R (Eq. (1.2)) can be visualized as the vector from the center of the ring to the center of mass of the system.

of R will thus take on values between 0 and 1, with larger $|R|$ corresponding to states where the oscillator phases are more closely bunched; that is, more heavily synchronized.

1.2 Lyapunov Exponents and Stability

Chapters 3 and 4 both make heavy use of Lyapunov analysis, which we describe briefly here. Consider an initial condition for a system of N units $\vec{x}(0)$, and then consider a differential perturbation from this initial condition $\vec{x}'(0) = \vec{x}(0) + \delta\vec{x}(0)$. We define the differential $\delta\vec{x}(t)$ as

$$\delta\vec{x}(t) = \vec{x}'(t) - \vec{x}(t).$$

The magnitude of $\delta\vec{x}(t)$ may increase or decrease with time, and in the limit, $t \to \infty$, this rate of increase or decrease will be characterized by the Lyapunov exponent
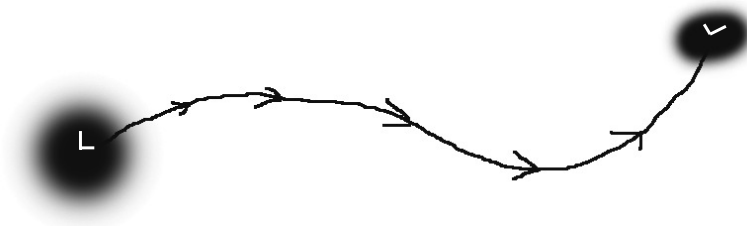
Figure 1.3: Example of Lyapunov dynamics. As a cloud of states around some initial condition are evolved, that cloud will expand in some directions and contract in others. The rates of expansion and contraction along different orthogonal axes give the Lyapunov exponents of the system.

associated with $\delta\vec{x}(0)$ is

$$h\left(\vec{x}(0), \delta\vec{x}(0)\right) = \lim_{\tau\to\infty} \frac{1}{\tau} \log \frac{||\delta\vec{x}(\tau)||}{||\delta\vec{x}(0)||}, \tag{1.3}$$

where $||\vec{v}||^2 = \vec{v}^T\vec{v}$. In principle, different choices for the direction of $\delta\vec{x}(0)$ will yield different Lyapunov exponents. In practice, however, any choice of $\delta\vec{x}(0)$, save a subset with Lebesgue measure zero, will evolve at a rate given by the largest Lyapunov exponent, which we will designate h_1. This largest exponent is often used in stability analysis: if $h_1 > 0$, it indicates that a trajectory is unstable, whereas if $h_1 < 0$ (and thus all other Lyapunov exponents are negative), the trajectory is stable and attracting, at least over small scales. In Chapter 4, Lyapunov analysis forms the basis of a master stability function, which associates h_1 with the parameters of the system.

In Chapter 3 we are interested in more than just the largest Lyapunov exponent, so instead of considering a single perturbation, we consider N mutually

orthogonal tangent vectors $\{\vec{v}_m\}$ which form a complete basis for the space. If $\{\vec{v}_m\}$ are chosen such that they evolve orthornormally, then perturbations in the directions of these tangent vectors will give a set of N Lyapunov exponents $\{h_m\}$ which characterize the microscopic evolution of the system.

1.3   Outline

The problems addressed and main results are as follows.

Chapter 2: In this chapter we consider a variant of the Kuramoto problem (Eq. (1.1)) in which the coupling between oscillators, rather than being all-to-all and equal strength, is determined by a network. That is, the coupling term in Eq. (1.1) is replaced by

$$\frac{k}{N} \sum_{j=1}^{N} A_{ij} \sin\left(\theta_j(t) - \theta_i(t)\right),$$

where $A_{ij} = 1$ if there is a network edge from j to i and $A_{ij} = 0$ if not. The main result is that for large N a recent exact solution technique for the all-to-all case can be extended to obtain results for certain types of newtorks.

Chapter 3: In this chapter we compute the full N-dimensional Lyapunov spectrum for a system of Kuramoto oscillators and show that the majority of Lyapunov exponents and their associated vectors are well-described as arising from the evolution of single oscillators interacting with the mean field. We contrast our results both with the results of other papers which studied similar systems and with those we would expect to arise from a low dimensional description of the macroscopic system state.

Chapter 4: In the final chapter we consider an adaptive coupling scheme for nearly-identical chaotic oscillators and explore through numerical simulations the conditions under which the scheme is stable. Using Master Stability analysis, we differentiate between "high quality" synchronization, in which the oscillators remain synchronized through the entire attractor, and conditions where "bubbling" (occasional bursts of desynchrony) occurs.

Chapter 2: The Dynamics of Network Coupled Phase Oscillators: An Ensemble Approach

2.1 Overview

We consider the dynamics of many phase oscillators that interact through a coupling network. For a given network connectivity we further consider an ensemble of such systems where, for each ensemble member, the set of oscillator natural frequencies is independently and randomly chosen according to a given distribution function. We then seek a statistical description of the dynamics of this ensemble. Use of this approach allows us to apply the recently developed ansatz of Ott and Antonsen [Chaos **18**, 037113 (2008)] to the marginal distribution of the ensemble of states at each node. This, in turn, results in a reduced set of ordinary differential equations determining these marginal distribution functions. The new set facilitates the analysis of network dynamics in several ways: (i) the time evolution of the reduced system of ensemble equations is much smoother, and thus numerical solutions can be obtained much faster by use of longer time steps; (ii) the new set of equations can be used as a basis for obtaining analytical results; and (iii) for a certain type of network, a reduction to a low dimensional description of the entire network

dynamics is possible. We illustrate our approach with numerical experiments on a network version of the classical Kuramoto problem, first with a unimodal frequency distribution, and then with a bimodal distribution. In the latter case, the network dynamics is characterized by bifurcations and hysteresis involving a variety of steady and periodic attractors.

2.2 Introduction

2.2.1 Background

Dynamical processes on networks are a central theme in the study of large complex systems. Issues in this general class of problems include disease spread, communications, opinion formation and synchronization, among others [1, 2]. In this chapter we will be concerned with synchronization of $N >> 1$ nonidentical oscillatory dynamical systems that are coupled to each other via a network whose adjacency matrix we denote A ($A_{ij} = 1$ if there is a link from j to i and $A_{ij} = 0$ if there is no link). Furthermore, we will assume that the state of each oscillator i is completely described by its phase θ_i ($0 \leq \theta_i < 2\pi$). Such oscillators are called "phase oscillators."

For the examples treated in this chapter, the dynamics will be taken to be described by

$$\frac{d\theta_i(t)}{dt} = \omega_i + \frac{k}{N} \sum_{j=1}^{N} A_{ij} \sin(\theta_j - \theta_i). \tag{2.1}$$

In the special case where $A_{ij} = 1$ for all i and j, we recover the classical, globally coupled, all-to-all Kuramoto model [3–7]. We emphasize that, although our

examples in Secs. 2.3 and 2.4 are of the form specified in Eq. (2.1), the general technique that our chapter will present is also applicable to other types of coupling and other types of systems (see Refs. [7–9] for a discussion of various system types and problems in the special context of global all-to-all coupling).

The case of network coupling (*i.e.*, nontrivial A in Eq. (2.1)) has recieved much recent attention (*e.g.* Refs. [10–14]), but general methods for facilitating analysis and understanding of large network coupled systems of phase oscillators (either of the type of Eq. (2.1) or more generally) have been lacking. In contrast, Refs. [8] and [9] have recently provided a broadly applicable analytical technique for various types of *globally all-to-all* coupled systems. This technique has so far been applied to a diverse set of issues. These include modeling of birdsong [15], bursting neurons [16], pedestrian induced shaking of London's Millennium Bridge [17], circadian rhythm [18], Josephson junction circuits [19], coupled excitable systems [20], noise [21], bimodal distributions of oscillator frequencies [22, 23], interaction time delay [24], phase resetting [25], time dependent connectivity [26], groups of coupled oscillators [27] and chimera states [28–33] (*i.e.*, states where one oscillator group is coherent while another is incoherent).

The utility of Refs. [8] and [9] for treating all-to-all coupled systems of phase oscillators suggests that an extension to network coupling, if possible, might prove useful. This chapter addresses the goal of making such an extension, and we test and illustrate our approach by application to the system of equations given by Eq. (2.1).

In defining the system (Eq. (2.1)), most previous works assign the values of

9

the oscillator natural frequencies ω_i by choosing them randomly and independently from some prespecified distribution function. Behavior of the system with these specified natural frequencies can then be investigated, *e.g.*, by numerical solution of Eq. (2.1). If one is interested in the statistics of the behavior originating from many different random choices of the natural frequencies, one could, in principle, integrate Eq. (2.1) with many such choices, and then examine the results. Here we consider a procedure related to this. In particular, we imagine an ensemble of systems, all with the same adjacency matrix A, but with each ensemble member having a different randomly chosen collection $\{\omega_i\}$ of natural frequencies, and we consider the evolution of this entire ensemble. This evolution can be thought of as being characterized by the set of marginal oscillator state distributions, $f_i(\theta_i, \omega_i, t)$, giving the probability density that oscillator i of a randomly selected ensemble member has natural frequency ω_i and, at time t, has the phase θ_i. At first sight, this appears to be a much more demanding problem than Eq. (2.1), since the time t state of node i of the ensemble is now described by a distribution *function*, while in Eq. (2.1) the time t state of node i is described by the *single scalar* variable θ_i. However, by use of the method of Refs. [8] and [9], we will show that, under appropriate conditions, the ensemble problem can be reduced to a set of ordinary differential equations whose size is similar to that of the original system; that is, for the case considered in Sec. 2.3 our formulation leads to a system of equations describing the ensemble that is of the same dimensionality as Eq. (2.1) (*i.e*, N, the number of oscillators), while in the case considered in Sec. 2.4 the dimensionality of the reduced description of the ensemble is $2N$.

Although this reduced ensemble description has, so far, not lead to a reduction of system dimensionality, we will show that it has advantages. These include:

(i) The time evolution of the reduced ensemble system is much smoother than is the case for Eq. (2.1), and thus numerical integrations of the reduced system can be done faster using much larger time steps.

(ii) In certain cases the reduced ensemble description is amenable to analysis that can enhance understanding and facilitate approximate quantitative results.

(iii) For the special case of networks with uniform in-degree, the reduced ensemble description leads to a massive reduction in dimensionality from $\mathcal{O}(N)$ to $\mathcal{O}(1)$.

The rest of this chapter will be devoted to justifying, illustrating and testing the above points through two examples (Sec. 2.3 and 2.4). Specifically, Sec. 2.3 considers Eq. (2.1) with a unimodal natural frequency distribution, while Sec. 2.4 considers the case of a bimodal natural frequency distribution (similar to the all-to-all case investigated in Ref. [22]). We note that in the bimodal case, the network dynamics is characterized by fairly complicated behavior including bifurcations and hysteresis involving a variety of steady and periodic attractors. Section 2.5 gives final discussion and conclusions.

2.2.2 Numerical Methods

To test the results of this chapter, we carried out numerical simulations on a variety of simulated networks. The code for all simulations was written in C, with

parallelization done using either OpenMP to take advantage of multiple CPU cores (4x 3.2 GHz AMD Phenom II) or CUDA to utilize our Nvidia Tesla C1060 GPGPU (240x 1.3 GHz stream processors). Any scripts were written in Bash. Eigenspectum computation was done in Python using the LAPACK package for NumPy.

In performing our numerical simulations, we used three different adjacency matrices: a directed network of uniform in-degree, an undirected Erdös-Renyi random graph and an undirected scale-free network. The same network size, $N = 10^4$, was used throughout.

The uniform in-degree network was generated in such a way as to have an in-degree $d^{in} = 100$ for all nodes: for each node i, exactly d^{in} other discrete nodes j were randomly selected. For each of those nodes j, A_{ij} was set to 1. The largest eigenvalue of this matrix is $\lambda_1 = d^{in} = 100$, and each entry of the corresponding right eigenvector $\vec{u}_1$ is $u_{1_i} = 1/\sqrt{N}$, for the normalization $\vec{u}_1^T \vec{u}_1 = 1$.

The Erdös-Renyi network was generated in such a way as to have the same average in-degree as the previous matrix. For each entry in the adjacency matrix A_{ij} (only looking at $j < i$), the probability of setting $A_{ij} = 1$ was uniform at $d_{\text{avg}}/(N-1)$. Once this upper triangle of the matrix had been generated, the remaining entries were set so as to make the matrix symmetric. That is, $A_{ji} \equiv A_{ij}$. For the particular random realization we used, the resulting matrix had largest eigenvalue $\lambda_1 = 100.97$.

The scale-free network was designed to have a largest eigenvalue approximately equal to that of the other two. It was generated using the configuration model [34]: first, the desired degree distribution was selected, $k_i = (i_0 + i)^{-1/(\gamma-1)}$, where i_0 is a parameter that gives the minimum degree and γ gives the resulting power of

the power-law degree distribution; then, for each entry of the adjacency matrix A_{ij}, $j < i$, the probability of setting $A_{ij} = 1$ was taken to be ck_ik_j where c is a renormalizing factor that allows us to control the number of edges in the network. As with the Erdös-Renyi network, once the upper triange of the matrix was generated, the lower triangle was set so that $A_{ji} \equiv A_{ij}$. The scale-free matrix we used had $\gamma = 2.5$ and largest eigenvalue $\lambda_1 = 100.34$.

Figure 2.1 shows the in-degree distributions for our Erdös-Renyi and scale-free networks, while Fig. 2.2 shows the eigenvalue spectra for the connectivity matrices of all three networks. As seen in Fig. 2.2 the eigenvalue of largest magnitude is real and positive and is well-separated from the other $N - 1$ eigenvalues (*cf.* Refs. [30,31]). This separation between the largest eigenvalue and the next-largest will be important in understanding the results stemming from Sec. 2.3.4.

2.3   Unimodal Frequency Distribution

2.3.1   Formulation

Consider a network of N discrete connected phase oscillators (nodes) whose phases are described by the vector $\vec{\theta} = [\theta_1, \theta_2, ..., \theta_N]^T$, where each node $i = 1, 2, ..., N$ has its own intrinsic frequency ω_i, and each ω_i is randomly chosen from a prescribed distribution function $g(\omega)$. If the connectivity matrix for the network is denoted by A and the nodes are influenced via the standard Kuramoto interaction, then the system is completely described by the set of N coupled, first order, ordinary differential equations (ODEs) given by Eq. (2.1).
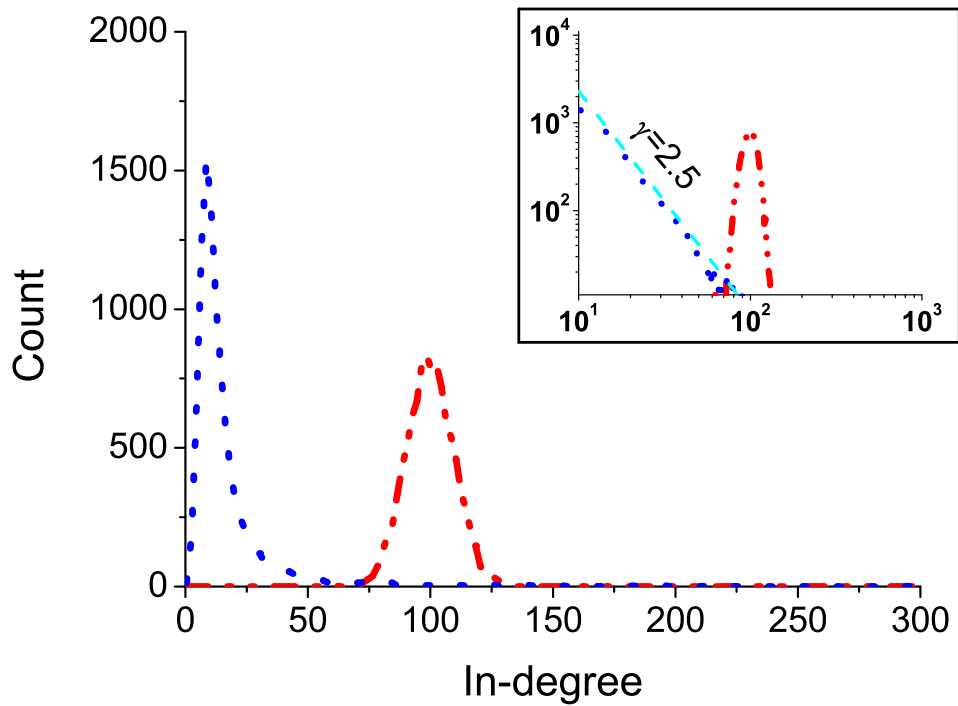
Figure 2.1: In-degree distributions for the the Erdös-Renyi and scale-free networks used in this chapter. The Erdös-Renyi network's degree distribution (dot-dashed line) is peaked around 100. Past a minimum degree, the scale-free network takes on a degree distribution (dotted line) of the form $P(d) \sim d^{-2.5}$, as is more clearly seen in the inset, which is the same plot shown on a log-log scale.
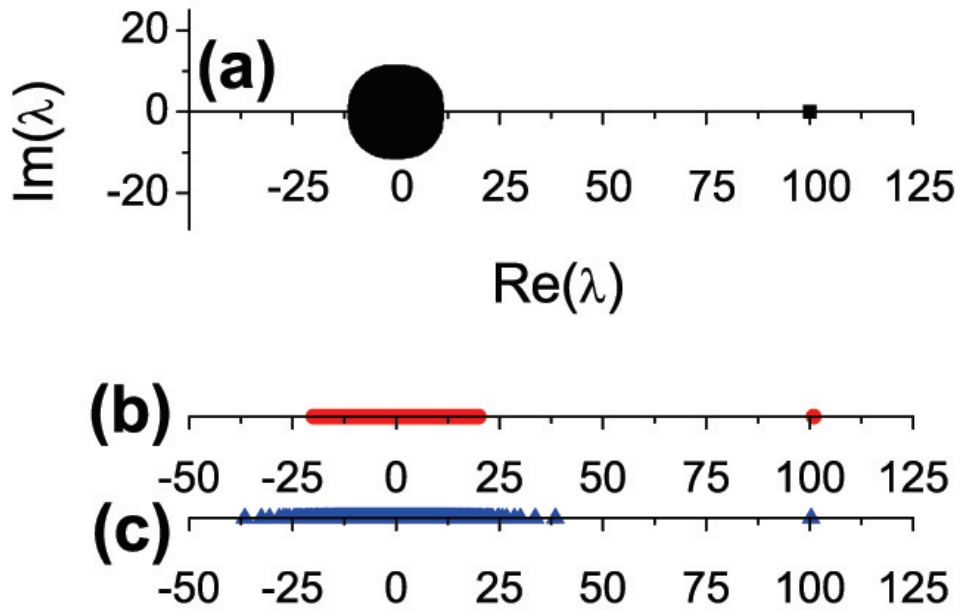
Figure 2.2: Eigenspectrum plots for the the three networks used in this chapter: (a) a directed network with uniform in-degree, (b) an undirected Erdös-Renyi network and (c) an undirected scale-free network ($\gamma = 2.5$). In all cases, $N = 10^4$ and $\lambda_1 \simeq 100$. Since the Erdos-Renyi and scale-free graphs are undirected, all eigenvalues in those cases are real.

Defining the order parameter R_i for each oscillator i,

$$R_i \equiv \frac{1}{N} \sum_{j=1}^{N} A_{ij} e^{i\theta_j}, \tag{2.2}$$

we can rewrite Eq. (2.1) as

$$\frac{d\theta_i}{dt} = \omega_i + k\text{Im}\left[e^{-i\theta_i} R_i\right]. \tag{2.3}$$

We now consider an ensemble of systems of the form of Eq. (2.3), where each member of the ensemble has the same fixed network as specified by its adjacency matrix A, and each member of the ensemble has a different randomly chosen set of nodal frequencies $\{\omega_i\}$. Thus we assume that a randomly chosen system ensemble member has nodal natural frequencies in the ranges,

$$\omega_1 \in \left[\omega_1' + d\omega_1'\right],$$

$$\omega_2 \in \left[\omega_2' + d\omega_2'\right],$$

$$\vdots$$

$$\omega_N \in \left[\omega_N' + d\omega_N'\right],$$

with probability

$$g(\omega_1')g(\omega_2')...g(\omega_N')d\omega_1'd\omega_2'...d\omega_N'.$$

We further envision that at $t = 0$ the initial angles are given with some probability distribution,

$$f_N(\theta_1, \theta_2, ..., \theta_N; \omega_1, \omega_2, ..., \omega_N; 0)$$

which evolves into the future $t \geq 0$ according to the oscillator conservation equation,

$$\frac{\partial f_N}{\partial t} + \sum_{i=1}^{N} \frac{\partial}{\partial \theta_i}\left[f_N \dot{\theta}_i\right] = 0. \tag{2.4}$$

In Eq. (2.4) $\dot{\theta}_i \equiv d\theta_i/dt$ is given by Eq. (2.3) (note that $\dot{\omega}_i = 0$), and

$$R_i \equiv \frac{1}{N} \sum_{j=1}^{N} A_{ij} \int e^{i\theta_j} f_N d^N \omega d^N \theta,$$

$$R_i = \frac{1}{N} \sum_{j=1}^{N} A_{ij} \int_{-\infty}^{\infty} d\omega_j \int_{0}^{2\pi} d\theta_j e^{i\theta_j} f_j(\theta_j, \omega_j, t), \qquad (2.5)$$

where f_j is the marginal distribution function

$$f_i(\theta_i, \omega_i, t) = \int f_N(\{\theta_j\}, \{\omega_j\}) \prod_{j \neq i} d\omega_j d\theta_j. \qquad (2.6)$$

Multiplying Eq. (2.4) by $\prod_{j \neq i} d\omega_j d\theta_j$ and integraing, we find that the marginal distribution functions satisfy

$$\frac{\partial f_i}{\partial t} + \frac{\partial}{\partial \theta}(f_i \dot{\theta}_i) = \frac{\partial f_i}{\partial t} + \frac{\partial f_i}{\partial \theta}\dot{\theta}_i + f_i \frac{\partial \dot{\theta}_i}{\partial \theta} = 0. \qquad (2.7)$$

Note that by use of this formulation we calculate the average behavior of the oscillator order parameters R_i over the ensemble [Eq. (2.5)] rather than the oscillator order parameter for a single realization [Eq. (2.2)]. For large systems (in the limit $N \to \infty$), one expects some degree of self-averaging, so that a suitable bulk order parameter (such as the one we introduce later in this section) will be the same, regardless of whether it was calculated from Eqs. (2.2) and (2.3) or from Eqs. (2.5) and (2.7).

Following Ref. [8], we proceed by seeking a special solution in the particular assumed form,

$$f_i(\theta_i, \omega_i, t) = \frac{g(\omega_i)}{2\pi} \left[1 + \sum_{n=1}^{\infty} \left(\alpha_i^n(\omega_i, t) e^{in\theta_i} + \alpha_i^{n*}(\omega_i, t) e^{-in\theta_i} \right) \right], \qquad (2.8)$$

where $|\alpha_i| < 1$ is assumed for convergence.

Inserting Eq. (2.8) in Eq. (2.7), we find that our special assumed form is a solution of Eq. (2.7) if

$$\frac{d\alpha_i}{dt} + i\alpha_i\omega_i + \frac{k}{2}\left[\alpha_i^2 R_i - R_i^*\right] = 0. \tag{2.9}$$

Furthermore, inserting Eq. (2.8) in Eq. (2.5) yields

$$R_i = \frac{1}{N}\sum_{j=1}^{N} A_{ij}\int_{-\infty}^{\infty}\alpha_j^*(\omega_j, t)g(\omega_j)d\omega_j. \tag{2.10}$$

We now consider the case where $g(\omega)$ is Lorentzian,

$$g(\omega) = \frac{1}{\pi}\frac{\Delta}{(\omega - \omega_0)^2 + \Delta^2} = \frac{1}{2\pi i}\left(\frac{1}{\omega - \omega_0 + i\Delta} - \frac{1}{\omega - \omega_0 - i\Delta}\right). \tag{2.11}$$

It has been shown [8] that, under appropriate restrictions in the initial conditions, $\alpha(\omega, t)$ is bounded and analytic in the lower-half ω-plane. Thus, we can close the integral in Eq. (2.10) in the lower-half plane to obtain from the pole at $\omega = \omega_0 - i\Delta$

$$R_i = \frac{1}{N}\sum_{j=1}^{N} A_{ij}\alpha_j^*(\omega_0 - i\Delta, t). \tag{2.12}$$

We define $\hat{\alpha}_i(t) \equiv \alpha_i(\omega_0 - i\Delta, t)$ and set $\omega = \omega_0 - i\Delta$ in Eq. (2.9) to obtain a system of N ordinary differential equations, for the quantities $\hat{\alpha}_i$,

$$0 = \frac{d\hat{\alpha}_i(t)}{dt} + i(\omega_0 - i\Delta)\hat{\alpha}_i(t) + \frac{k}{2}\left[\hat{\alpha}_i^2(t)R_i(t) - R_i^*(t)\right], \tag{2.13}$$

$$R_i = \frac{1}{N}\sum_{j=1}^{N} A_{ij}\hat{\alpha}_j^*(t). \tag{2.14}$$

As shown in Ref. [9], the long-time system behavior of Eqs. (2.5) and (2.7) is attracted to the manifold of solutions of the form of Eq. (2.8), and Eqs. (2.13) and (2.14) thus describe all possible attractors and bifurcations of the system.

By making the transformation $\hat{\alpha}_i \to \hat{\alpha}_i e^{i\omega_0 t}$, the quantity ω_0 is transformed to zero. With this done, Eqs. (2.13) and (2.14) become consistent with the assumption that $\hat{\alpha}_i$ and R_i are real, and we obtain

$$0 = \frac{d\hat{\alpha}_i(t)}{dt} + \Delta\hat{\alpha}_i(t) + \frac{kR_i}{2}\left[\hat{\alpha}_i^2(t) - 1\right], \tag{2.15}$$

$$R_i = \frac{1}{N}\sum_{j=1}^{N} A_{ij}\hat{\alpha}_j(t). \tag{2.16}$$

While this *ensemble formulation* of the Kuramoto problem has not resulted in a decrease in the number of equations compared to the original formulation, Eqs. (2.3) and (2.2) (which we henceforth refer to as the *theta formulation*), the set of equations described in Eqs. (2.15) and (2.16) offer several advantages. One advantage is that the system described by our ensemble formulation equations is more "robust," owing to the fact that the ensemble formulation equations, by their nature, average over a range of initial conditions. Computationally, as shown in Figs. 2.3-2.5, whereas the theta formulation equations require many trials to produce smooth data, the ensemble formulation equations require only one, and may be run using larger timesteps: generally, we found that for ensemble formulation simulations, we could use a time step size ten times larger than the one required for theta formulation simulations.

Another advantage of our ensemble formulation equations is that they facilitate analysis of the system. In particular, in Secs. 2.3.3 and 2.3.4 we will use these equations to obtain information about the fixed-point attractors of the system. Furthermore, in Sec. 2.3.5 we will demonstrate, for the case of uniform in-degree, a reduction of the full system [Eq. (2.15)] of N ODEs to a single ODE.

2.3.2 Bulk Order Parameter

In describing the behavior of the system, we are more concerned with the aggregate behavior, rather than, say, the individual order parameters R_i (as given by Eq. (2.2) and equivalently by Eq. (2.5)). Thus, we define an average order parameter for the entire network,

$$r \equiv |\vec{v}_1^T \vec{R}|, \tag{2.17}$$

where $\vec{v}_1$ is the left eigenvector of the adjacency matrix A corresponding to its eigenvalue of largest magnitude, and is normalized so that $\vec{v}_1^T \vec{u}_1 = \vec{u}_1^T \vec{u}_1 = 1$, where $\vec{u}_1$ is the associated right eigenvector. The reason for this choice of order parameter will be made more clear in Sec. 2.3.4.

Figures 2.3-2.5 shows the time-evolution of r for simulations carried out on the three networks introduced in Sec. 2.2.2, for a selection of coupling strengths k. For the theta formualtion simulations the initial values of θ_i were random in $[0, 2\pi)$; for the ensemble formulation the $\hat{\alpha}_i(0)$ were set to zero, save $\hat{\alpha}_1$, which was initialized small compared to one; to compare the time evolutions, the ensemble formulation curves in Figs. 2.3-2.5 were horizontally shifted to most closely match those of the theta formulation. For all three networks, the ensemble formulation simulations reproduces the results for the theta formulation simulations: not only does r asymptote to the same values, but the evolution takes the same shape, accurately reproducing the transient rise to synchrony. The agreement between the theta and ensemble formulation results is best when r is large, as there is noise

inherent to the theta formulation results. Note that, as previously claimed, these ensemble formulation computations can be carried out at larger time step than the theta formulation computations, and thus are much faster.

2.3.3 Steady State

Setting $d\hat{\alpha}_i/dt = 0$, Eq. (2.15) gives the quadratic equation,

$$0 = \hat{\alpha}_i^2 - 1 + \frac{2\Delta}{kR_i}\hat{\alpha}_i. \tag{2.18}$$

With the requirement that $|\hat{\alpha}_i| \leq 1$, we have the solution,

$$\hat{\alpha}_i = \sqrt{\frac{\Delta^2}{k^2R_i^2} + 1} - \frac{\Delta}{kR_i}. \tag{2.19}$$

Inserting this into Eq. (2.16), we obtain a system of N transcendental equations for the oscillator order parameters,

$$R_i = \frac{1}{N}\sum_{j=1}^{N} A_{ij}\left(\sqrt{\frac{\Delta^2}{k^2R_j^2} + 1} - \frac{\Delta}{kR_j}\right). \tag{2.20}$$

Equations (2.20) can be solved numerically by inserting an initial guess for $\{R_j\}$ on the right side, calculating the new $\{R_i\}$ and iterating this process. This results in steady state values of $\{R_i\}$ with much less computation than would be necessary if the same information were obtained using either our theta formulation or ensemble formulation equations.

Our Eq. (2.20) agrees with Eq. (14) of Ref. [13] for $g(\omega)$ Lorentzian. However, our derivation followed without approximation once the ensemble viewpoint is adopted, while Eq. (14) of Ref. [13] was derived using approximations that, although reasonable, are not easy to justify in a rigorous way. On the other hand,
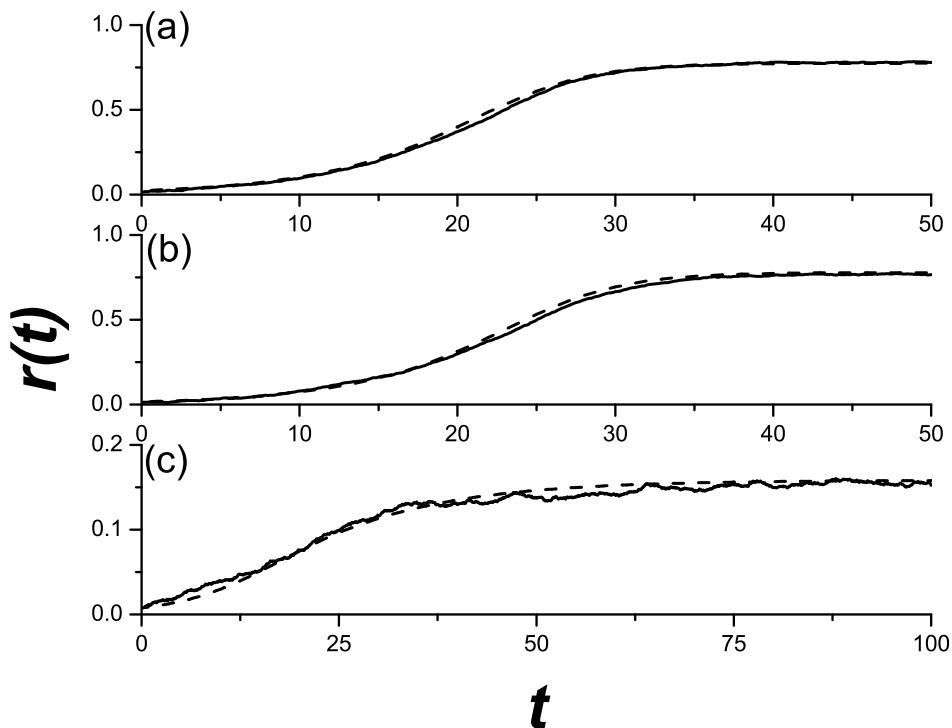
Figure 2.3: Bulk order parameter r vs. time for systems simulated using the theta formulation (Eqs. (2.1) and (2.2)) as well as our ensemble formulation (Eqs. (2.15) and (2.16)), performed on the networks introduced in Sec. 2.2.2: (a) uniform in-degree, (b) Erdös-Renyi and (c) scale-free. Results were generated numerically using a fourth-order Runge-Kutta integration scheme with fixed time step. Each curve represents a single simulation–no curves are averaged. A time step $\Delta t = 0.1$ was used for all theta formulation simulations, save for the scale-free, for which $\Delta t = 0.05$ was used, while all ensemble formulation simulations used a time step ten times larger than was used for the corresponding theta formulation simulations. The width of the frequency distribution was set to $\Delta = 0.1$ and the coupling strength to $k = 50 \simeq 2.5k_c$.
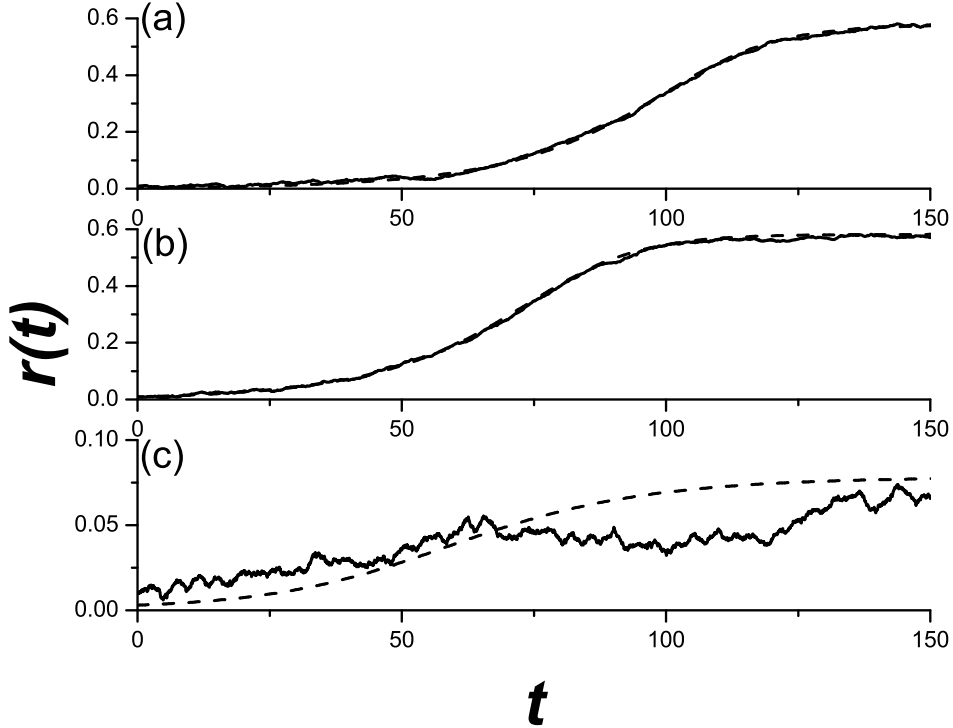
Figure 2.4: Same as Fig. 2.3 but with $k = 30 \simeq 1.5 k_c$

the result of (14) of Ref. [13] is for a general distribution of $g(\omega)$ and is not limited to the Lorentzian. Thus we regard our result [Eq. (2.20)] and that of Ref. [13] as being complementary and reinforcing of each other.

In addition to direct numerical solution of Eq. (2.20), Eq. (2.20) can also be used as a basis for further analysis. In this latter regard we now use Eq. (2.20) to obtain the critical coupling strength $k = k_c$, such that, for $k < k_c$, $R_i \to 0$ (*i.e.*, the network oscillator phases are incoherent) while for $k > k_c$, coherence emerges. Expanding Eq. (2.20) to first order in $k R_j / \Delta << 1$, we obtain

$$\vec{R} \simeq \frac{k}{2N\Delta} A \vec{R}, \tag{2.21}$$

where $\vec{R} = [R_1, R_2, ..., R_N]^T$. This is an eigenvalue problem, and so the smallest
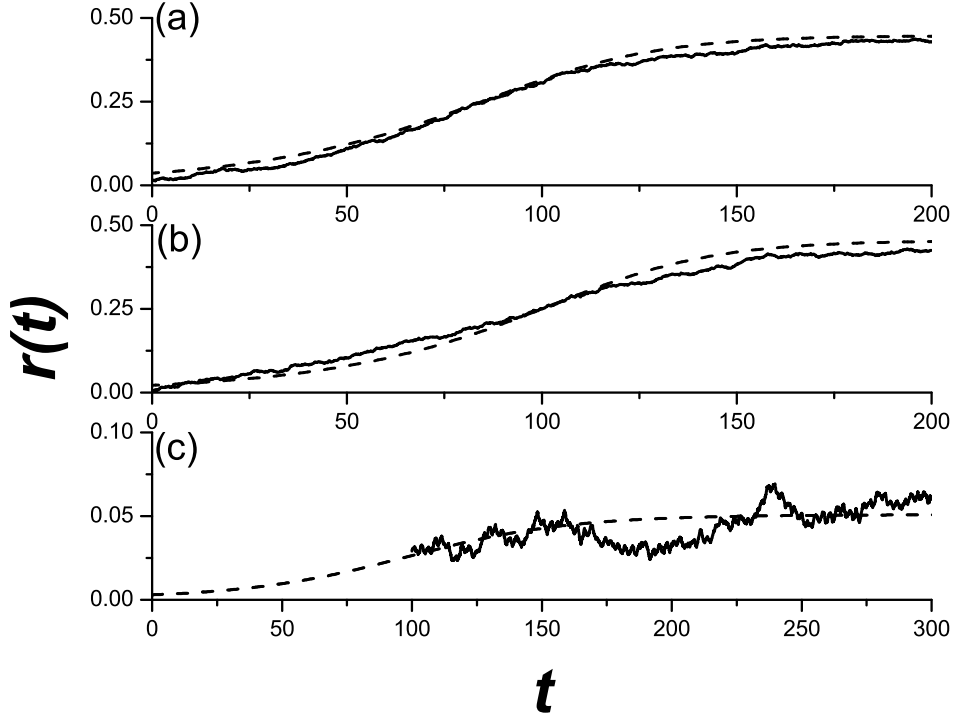
Figure 2.5: Same as Figs. 2.3 and 2.4 but with $k = 25 \simeq 1.25 k_c$

coupling strength to have a nonzero solution to this equation will occur for the largest eigenvalue of A, which we will denote λ_1. Thus, as previously found in Ref. [13], the critical coupling strength is

$$k_c = \frac{2N\Delta}{\lambda_1}. \tag{2.22}$$

2.3.4 Maximum Eigenvalue Approximation

In order to investigate steady state behavior for $k > k_c$, we assume that the eigenvalues of A are distinct and decompose A into the sum,

$$A = \sum_{k=1}^{N} \lambda_k \vec{u}_k \vec{v}_k^T, \tag{2.23}$$

24

where $\{\vec{u}_k\}$ and $\{\vec{v}_k\}$ are, respectively, the sets of right and left eigenvectors of A and $\{\lambda_k\}$ is the set of corresponding eigenvalues (the eigenvectors are normalized such that $\vec{v}_l^T \vec{u}_k = \delta_{kl}$ and $|\vec{u}_k| = 1$). Since all entries of the adjacency matrix are non-negative, the Perron-Frobenius theorem suggests that there is a unique eigenvalue of largest magnitude, which is real and positive. Assuming that this largest eigenvalue is much larger than all the others, we consider only the first term in Eq. (2.23),

$$A \simeq \lambda_1 \vec{u}_1 \vec{v}_1^T. \tag{2.24}$$

As shown in Fig. 2.2, we expect this approximation to be more appropriate for our uniform in-degree network and our Erdös-Renyi graphs, where λ_1 is larger than the magnitude of the second largest eigenvalue λ_2 by a factor of 9.93 and 5.05, respectively, and less so for the scale-free network, where the ratio is only 1.89.

Using Eq. (2.24) in Eq. (2.16) implies that $\vec{R}$ is approximately parallel to $\vec{u}_1$, and thus we define a scalar ρ by

$$\vec{R} = \rho \vec{u}_1, \tag{2.25}$$

where, again using Eq. (2.16), ρ is

$$\rho \equiv \frac{\lambda_1}{N} \sum_{i=1}^{N} v_{1_i} \hat{\alpha}_i(t) \tag{2.26}$$

Note that $\vec{v}_1^T \vec{R} = \rho \vec{v}_1^T \vec{u}_1 = \rho$. Thus, as long as the maximum eigenvalue approximation [Eq. 2.24)] holds, our bulk order parameter [Eq. (2.17)] is given by $r = \rho$.

Using Eq. (2.25) in Eq. (2.20), we obtain to a single transcendental equation for ρ,

$$\rho^2 = \frac{\lambda_1}{N} \sum_{j=1}^{N} \frac{v_{1_j}}{u_{1_j}} \left(\sqrt{\frac{\Delta^2}{k^2} + \rho^2 u_{1_j}^2} - \frac{\Delta}{k} \right) \tag{2.27}$$

25

As shown in Fig. 2.6, this solution matches the steady-state results of running lengthy theta formulation or ensemble formulation simulations only to the extent that the maximum eigenvalue approximation holds. Specifically, we see excellent agreement for our uniform in-degree and Erdös-Renyi networks, while, for scale-free networks, for which the maximum eigenvalue approximation does not hold well, we see discrepancies.

From Eq. (2.27), we can obtain an upper bound to our bulk order parameter by considering the limit where $\Delta/k \to 0$,

$$\rho_{\text{max}} = \frac{\lambda_1}{N} \sum_{j=1}^{N} v_{1_j}. \tag{2.28}$$

We note that for the uniform in-degree and Erdös-Renyi networks, each entry of the right eigenvalue $\{u_{1_i}\}$ is approximately equal, and thus, due to normalization, approximately equal to $1/\sqrt{N}$. Since $\vec{v}_1^T u_1 = 1$, this implies that the sum in Eq. (2.28) is approximately equal to $\sqrt{N}$ and thus, $\rho_{\text{max}} \simeq \lambda_1/\sqrt{N}$. We further note that this does not hold for the scale-free case.

Equation (2.27) may be further simplified if we define $\xi \equiv \rho^2 k^2/\Delta^2$. In terms of this new quantity,

$$\xi = \frac{2k}{k_c} \sum_{j=1}^{N} \frac{v_{1_j}}{u_{1_j}} \left(\sqrt{1 + \xi u_{1_j}^2} - 1 \right) \equiv \frac{k}{k_c} F(\xi). \tag{2.29}$$

We remark that one can show that the function $F(\xi)$ in Eq. (2.29) has $F(0) = 0$, $F'(0) = 1$, $F''(\xi) < 0$ and increases as $\sqrt{\xi}$ for large positive ξ. As illustrated in Fig. 2.7, these properties imply that Eq. (2.29) has no positive solutions if $k < k_c$ and exactly one positive solution if $k > k_c$.
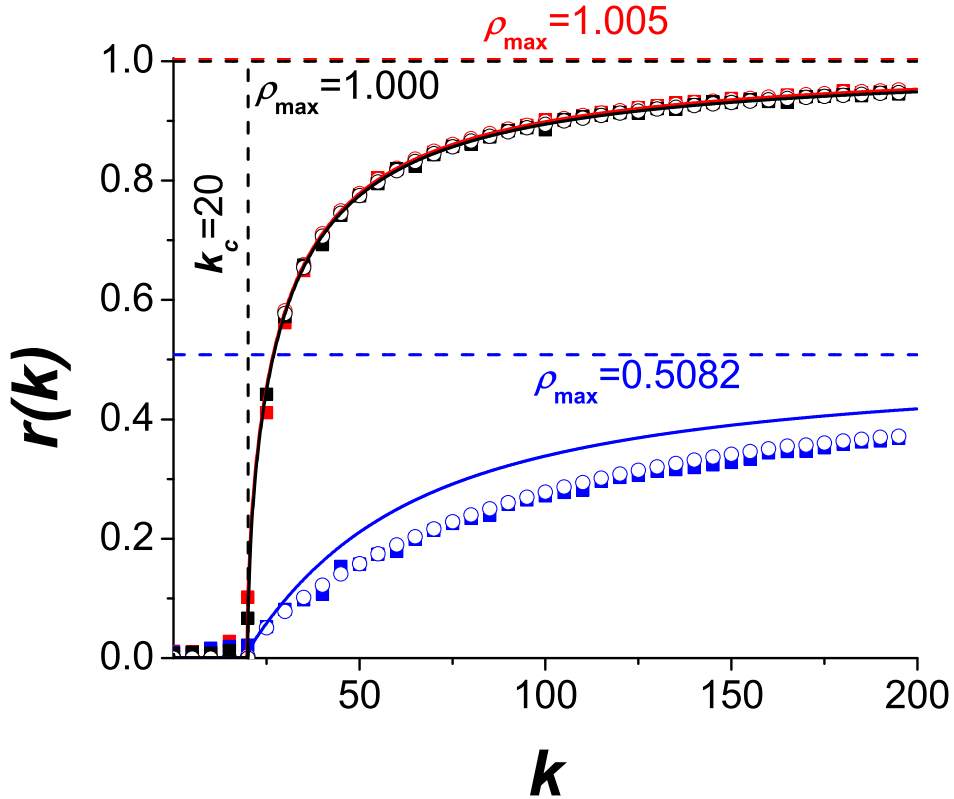
Figure 2.6: Long-time-averaged values of r vs. k for systems simulated using the theta formulation [Eqs. (2.1) and (2.2)] and for identical systems simulated using our ensemble formulation [Eqs. (2.15) and (2.16)] and ρ calculated from the transcendental equation (Eq. (2.27)). Also shown as dashed lines are the critical coupling value k_c, which is approximately the same for all three networks, and the values of $\rho_{\max}$ [Eq. (2.28)] for the three networks. The same integration scheme was used as for Figs. 2.3-2.5. Simulations were generally run for 300 time units for the theta formulation simulations, with averaging done over the last 50 time units, while the ensemble formulation simulations were run until they converged (generally between 200 and 500 time units). Selected points were rerun at smaller time step size and longer simulation runtime to ensure validity.
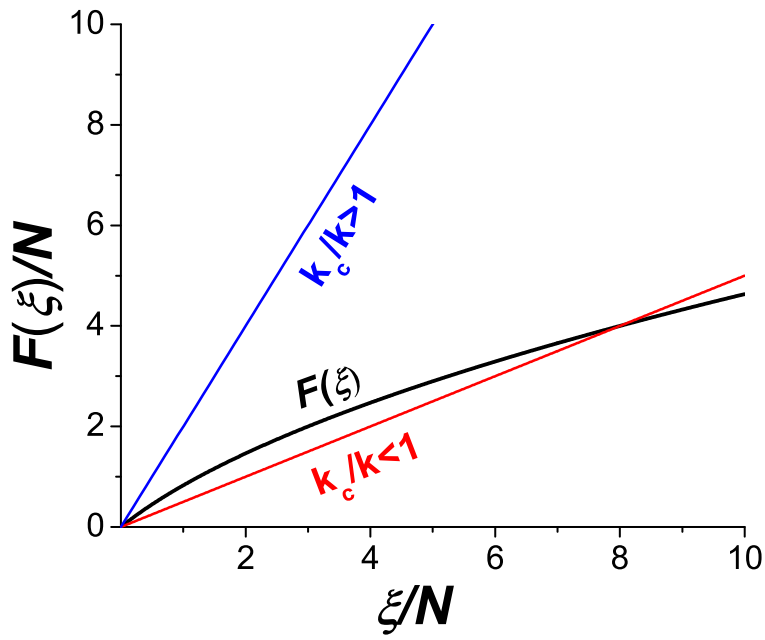
Figure 2.7: $F(\xi)/N$ and $(k_c/k)\xi$ vs. ξ/N for two different values of k_c/k. When $k_c/k > 1$, there is no nonzero intersection of the two curves (thus, no nonzero solution to Eq. (2.29)).

2.3.5 Special case: Uniform in-degree

In the case of networks with uniform in-degree, $d^{in} = \sum_j A_{ij}$ independent of i, Eqs. (2.15) and (2.16) admit a special solution,

$$\hat{\alpha}_1(t) = \hat{\alpha}_2(t) = ... = \hat{\alpha}_N(t) \equiv \alpha(t). \tag{2.30}$$

Restricting Eqs. (2.15) and (2.16) to this manifold yields

$$\frac{1}{\Delta}\frac{d\alpha}{dt} + \alpha + \frac{kd^{in}}{2N\Delta}\left(\alpha^2 - 1\right)\alpha = 0. \tag{2.31}$$

If we define $K \equiv (kd^{in})/(N\Delta)$, Eq. (2.31) becomes identical to Eq. (10) of Ref. [8] which was derived for the all-to-all coupled case. As noted in Ref. [8], the solution to Eq. (2.31) is

$$\frac{\alpha(t)}{\alpha_\infty} = \left\{1 + \left[\left(\frac{\alpha_\infty}{\alpha_0}\right)^2 - 1\right]\exp\left[1 - \frac{K}{2}\Delta t\right]\right\}^{-1/2}, \tag{2.32}$$

where

$$\alpha_\infty = \sqrt{1 - \left(\frac{2}{K}\right)} \tag{2.33}$$

is the value that $\alpha(t)$ approaches as $t \to \infty$ when $k > k_c$ (that is, $K > 2$). Note that this same value of α_∞ follows from the solution of Eq. (2.20) in the uniform in-degree case with all the R_i set equal. To test the relevance of Eq. (2.32), we compare its prediction for $r(t)$ with that from solution of Eq. (2.15) for $k > k_c$, where we initialize Eq. (2.15) with $\hat{\vec{\alpha}}(0)$ far from the manifold given by Eq. (2.30) by setting $\hat{\alpha}_1(0)$ to some nonzero value ($\hat{\alpha}_1(0) = 1$) and $\hat{\alpha}_2(0) = \hat{\alpha}_3(0) = ...\hat{\alpha}_N(0) = 0$. Adjusting $\hat{\alpha}(0)$ in Eq. (2.32) to provide the best apparent fit, we obtain the results for $r(t)$ plotted in Fig. 2.8. The good agreement between Eq. (2.32) (solid line in
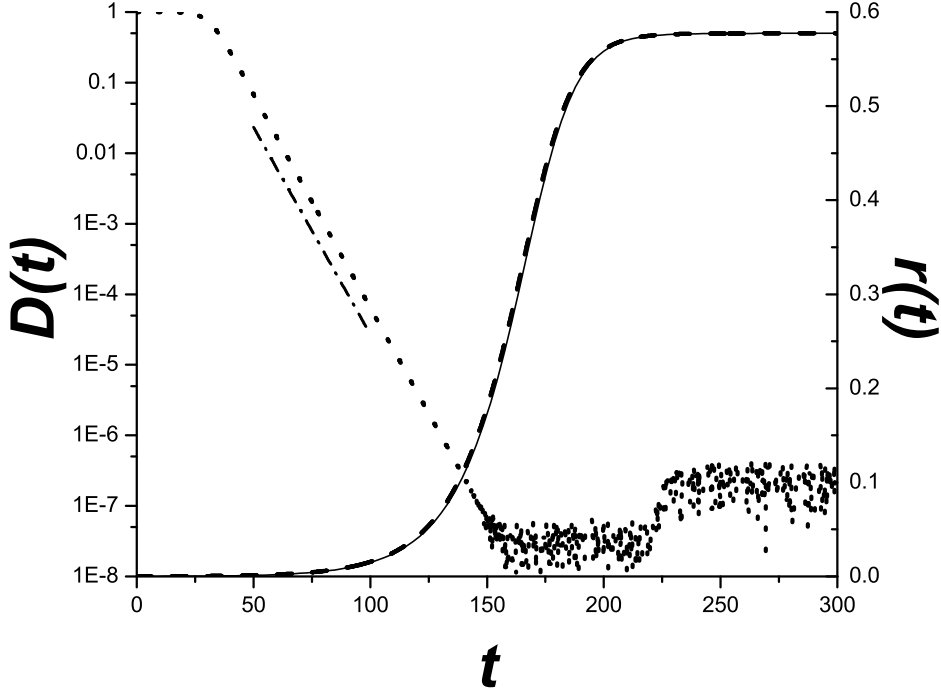
Figure 2.8: Bulk order parameter r vs. t for our uniform in-degree network simulated using our ensemble formulation [Eqs. (2.15) and (2.16)] (dashed line) plotted with ρ calculated from Eq. (2.32) (solid line). The normalized L_2 deviation, D, from the manifold given by Eq. (2.30) is also plotted (dotted line) along with the slope given by Eq. (2.41) (dash-dotted line).

Fig. 2.8) and Eq. (2.15) (dashed line) indicate that the solutions to Eq. (2.15) are rapidly attracted to the solution manifold [Eq. 2.30]. This is further confirmed by computation of the normalized L_2 deviation of $\vec{\alpha}$ from the equal-α manifold, which we define by

$$D \equiv \sqrt{\frac{\sum_i (\alpha_i - \bar{\alpha})^2}{\sum_i \alpha_i^2}}, \tag{2.34}$$

where $\bar{\alpha} = \sum_i \alpha_i / N$. The evolution of D is plotted as a dotted line in Fig. 2.8. It is seen that, after about $t = 60$, $D(t)$ decreases exponentially with time

30

(as indicated by the linear dependence on the semi-log plot of Fig. 2.8), reaching the level of numerical roundoff by $t \simeq 150$. Although the curves in Fig. 2.8 are for a difected network, to explain this exponential decrease, it is somewhat simpler to consider an undirected network, in which case $A^T = A$, λ_k is real, $\vec{v}_k = \vec{u}_k$, $\vec{u}_k^T \vec{u}_l = \delta_{kl}$, and we use the convention, $\lambda_k \geq \lambda_{k+1}$. We note that for uniform in-degree, $\lambda_1 = d^{in}$ and the elements of $\vec{u}_1$ are all equal. Thus, $\vec{u}_1$ corresponds to the manifold given by Eq. (2.30), and, by the orthogonality condition ($\vec{u}_k^T \vec{u}_1 = 0$ for $k \geq 2$), all other eigen-directions are perpendicular to the manifold. Writing $\hat{\vec{\alpha}}$ in the eigenvalue basis, we have

$$\hat{\vec{\alpha}}(t) = \sum_{k=1}^{N} a_k(t)\vec{u}_k, \tag{2.35}$$

with $a_k(0) = \vec{u}_k^T \hat{\vec{\alpha}}(0)$. Thus we obtain

$$D = \sqrt{\frac{\sum_{k=2}^{N} a_k^2}{\sum_{k=1}^{N} a_k^2}} \tag{2.36}$$

Initially the components of $\hat{\vec{\alpha}}$ are small and we may linearize Eq. (2.15) to obtain

$$\frac{d\hat{\vec{\alpha}}}{dt} + \Delta\hat{\vec{\alpha}} - \frac{k}{2N}A\hat{\vec{\alpha}} = 0. \tag{2.37}$$

Inserting Eq. (2.35) into Eq. (2.37) we have

$$a_k(t) = a_k(0)e^{\gamma_k t} \tag{2.38}$$

and

$$\gamma_k(t) = \frac{k\lambda_k}{2N} - \Delta. \tag{2.39}$$

Since $\gamma_k \geq \gamma_{k+1}$, after an inital phase, the sums in Eq. (2.36) are dominated by their first terms,

$$D(t) \simeq \frac{|a_1(t)|}{|a_2(t)|} = c \exp\left[-(\gamma_1 - \gamma_2)t\right], \tag{2.40}$$

31

where c is a constant. Thus we see that $D(t)$ should decrease exponentially at the rate

$$(\gamma_1 - \gamma_2) = k(d^{in} - \lambda_2)/(2N). \tag{2.41}$$

For the case in Fig. 2.8 ($d^{in} = 100$, $\lambda_2 = 9.94$) this predicted slope is plotted as the dash-dotted line segment and is seen to yield excellent agreement with the slope of the dotted curve.

2.4 Bimodal Frequency Distribution

2.4.1 Formulation

We now turn our attention to the case where, instead of a single-peaked Lorentzian for our frequency distribution $g(\omega)$, we choose a bimodal distribution,

$$g(\omega) = \frac{\Delta}{2\pi} \left(\frac{1}{(\omega - \omega_0)^2 + \Delta^2} + \frac{1}{(\omega + \omega_0)^2 + \Delta^2} \right). \tag{2.42}$$

In this case, when we close the integral $\int_{-\infty}^{\infty} \alpha^* g d\omega_j$, in the lower-half plane, we encircle *two* poles, one at $\omega = +\omega_0 - i\Delta$ and one at $\omega = -\omega_0 - i\Delta$. Thus we obtain two residue contributions,

$$R_i = \frac{1}{2N} \sum_{j=1}^{N} A_{ij} \left[\alpha_j^*(\omega_0 - i\Delta, t) + \alpha_j^*(-\omega_0 - i\Delta, t) \right]. \tag{2.43}$$

Evaluating Eq. (2.9) at our two poles, we obtain a set of $2N$ ODEs,

$$\dot{\alpha}_i^{\pm} \equiv \frac{d\alpha_i^{\pm}}{dt} = -(\Delta \pm i\omega_0)\alpha_i^{\pm} + \frac{k}{2} \left[R_i^* - R_i(\alpha_i^{\pm})^2 \right], \tag{2.44}$$

where we have defined

$$\alpha_i^{\pm}(t) \equiv \alpha_i(\pm\omega_0 - i\Delta, t). \tag{2.45}$$

2.4.2 Uniform In-degree

Similar to the analysis in Sec. 2.3.5, by assuming that the network has uniform in-degree $d^{in} = \sum_j A_{ij}$ where d^{in} is independent of i, one finds that one can obtain an exact special solution of Eq. (2.44) by setting

$$\alpha_i^{\pm} = \alpha_j^{\pm} \equiv \alpha^{\pm}, \tag{2.46}$$

in which case the system of $2N$ ODEs given by Eq. (2.44) reduces to a system of only two ODEs:

$$\dot{\rho}^{\pm} = -(\Delta \mp i\omega_0)\rho^{\pm} + \frac{kd^{in}}{4N}\left[(\rho^+ + \rho^-) - \frac{4N}{(d^{in})^2}\left(\rho^{\pm}\right)^2\left(\rho^+ + \rho^-\right)^*\right], \tag{2.47}$$

where

$$\rho^{\pm} \equiv \frac{d^{in}}{2\sqrt{N}}\left(\alpha^{\pm}\right)^*. \tag{2.48}$$

Introducing polar coordinates, $\rho^{\pm} = a^{\pm}\exp\left(i\phi^{\pm}\right)$, we obtain three real ODEs,

$$\dot{a}^{\pm} = -\Delta a^{\pm} + \frac{kd^{in}}{4N}\left(1 - \frac{4N}{(d^{in})^2}\left(a^{\pm}\right)^2\right)\left(a^{\pm} + a^{\mp}\cos\psi\right), \tag{2.49}$$

where $\psi \equiv \phi^+ - \phi^-$, and

$$\dot{\psi} = 2\omega_0 - \frac{kd^{in}}{4N}\left[\frac{a^+}{a^-} + \frac{a^-}{a^+} + \frac{8N}{(d^{in})^2}a^+a^-\right]\sin\psi. \tag{2.50}$$

Thus the set of $2N$ complex first order ODEs [Eq. (2.44)] reduces to a set of just three real ODEs [Eqs. (2.49) and (2.50)].

If we further assume that the solutions of interest obey the symmetry $a^+ = a^- \equiv a$, then the equations simplify further, from 3 ODEs to 2 ODEs,

$$\dot{a} = a\frac{kd^{in}}{4N}\left[1 - \frac{4N\Delta}{kd^{in}} - \frac{4N}{(d^{in})^2}a^2 + (1 - \frac{4N}{(d^{in})^2}a^2)\cos\psi\right] \tag{2.51}$$

and

$$\dot{\psi} = 2\omega_0 - \frac{kd^{in}}{2N} \left[1 + \frac{4N}{(d^{in})^2} a^2 \right] \sin \psi. \tag{2.52}$$

These equations are equivalent to Eqs. (22) and (23) of Ref. [22], in the case where $d^{in} = N$ (representing global all-to-all coupling).

To relate a and ψ to the bulk order parameter used in previous sections, we note that, from Eqs. 2.26 and 2.48,

$$\rho = \rho^+ + \rho^-$$

(with $r \simeq \rho$ as long as the Maximum Eigenvalue approximation holds). From our definitions of a and ψ, then, we find that

$$\rho = 2a \cos \psi/2 \tag{2.53}$$

if we assume that ρ is real.

We stress that, while this is a solution to the reduced system, the ansatz expressed in Eq. (2.46) (as well as the symmetry $a^+ = a^-$) has yet to be justified. In particular, assuming that, by solving Eqs. (2.51) and (2.52), we have found solutions $\alpha_i^{\pm} = \alpha^{\pm}$ of the system of Eq. (2.44), one can ask what happens if we add in small perturbations $\delta\alpha_i^{\pm}$ to this solution; that is, we set $\alpha_i^{\pm} = \alpha^{\pm} + \delta\alpha_i^{\pm}$. Substituting these perturbed states into Eq. (2.44), we can linearize to obtain evolution equations for the perturbations. If these perturbations grow exponentially with time, then our solutions are unstable and are not expected to exist in typical situations. This problem is analogous to that of the stability of the synchronization manifold of coupled chaotic systems, often studied by the master stability function technique

[37,38]. Here we leave the study of the linearized equations for the quantitites $\delta\alpha_i^{\pm}$ as a problem for further study. However, Fig. 2.9 supports the idea that this ansatz is stable. Figure 2.9 plots $r(t)$ for a simulation using the theta formulation for a network with uniform in-degree and for a simulation using Eqs. (2.51) and (2.52). Values for the various parameters were chosen such that the system converged to a limit cycle attractor. The excellent agreement between the two curves at large times, both in magnitude and period of oscillation, indicates that, even if the system did not start on the manifold of Eq. (2.46), then it converged onto it.

In Sec. 2.4.3 we further address the question of the stability of the ansatz (2.46) by comparing long-time solutions of Eqs. (2.51) and (2.52) with full theta formulation simulations [Eq. (2.1)]. As shown in Sec. 2.4.3, these simulations confirm that the manifold (2.46) in the full state space of Eq. (2.44) is stable, and moreover, globally attracting.

2.4.3 Dynamics

We may rescale the parameters of Eqs. (2.51) and (2.52) to make the equations independent of K, N and d^{in} by defining

$$\tilde{\Delta} \equiv 4N\Delta/(kd^{in}), \tag{2.54}$$

$$\tilde{\omega}_0 \equiv 4N\omega_0/(kd^{in}), \tag{2.55}$$

$$\tilde{t} \equiv kd^{in}t/(4N) \tag{2.56}$$

and

$$\tilde{a} \equiv 2\sqrt{N}a/d^{in}, \tag{2.57}$$
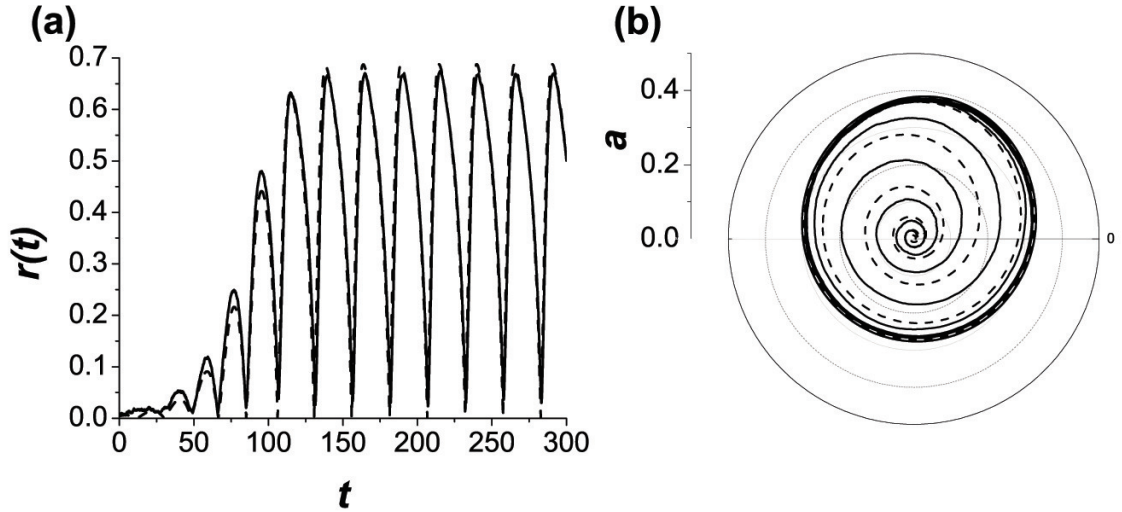
Figure 2.9: (a) Bulk order parameter r plotted vs. time for a theta formulation simulations [Eq. (2.1)] on our uniform in-degree network using a bimodal distribution (solid line) and for a simulation using Eqs. (2.51) and (2.52) (dashed line). A time step of 0.05 was used for both simulations. The parameters of the simulation were $k = 40$, $\Delta = 0.5$ and $\omega_0 = 0.2$. (b) A parametric polar plot (a, ψ) of the same simulations, starting at incoherent initial conditions ($r << 1$).

in which case Eqs. (2.51) and (2.52) become:

$$\frac{d\tilde{a}}{d\tilde{t}} = \tilde{a}\left[1 - \tilde{\Delta} - \tilde{a}^2 + \left(1 - \tilde{a}^2\right)\cos\psi\right] \tag{2.58}$$

and

$$\frac{d\psi}{d\tilde{t}} = 2\left[\tilde{\omega}_0 - \left(1 + \tilde{a}^2\right)\sin\psi\right] \tag{2.59}$$

The dynamics of Eqs. (2.58) and (2.59) have been thoroughly documented in Ref. [22]. Whereas the unimodal problem only exhibited fixed point solutions, the bimodal case allows for such phenomena as hysteresis and limit cycle attractors. These dynamics are summarized in our Fig. 2.10, which is similar to Fig. 2. of Ref. [22]. In Fig. 2.10 we show five distinct regions [labeled (i)-(v)]. For each of the five regions in Fig. 2.10, we have indicated the type of attractor (or types of attractors) that exist in that region using the following notations: I for incoherent, corresponding to a steady state at $r = 0$; SS for coherent steady state, corresponding to a constant nonzero attracting value of r; and LC for a limit cycle attractor for which r varies periodically in time. Note that regions (i)-(iii) are characterized by the presence of a single unique attractor, while regions (iv) and (v) each have two coexisting attractors (SS and I for (iv); LC and SS for (v)). Thus we expect hysteresis to be associated with parameter scans passing through regions (iv) and (v).

Figure 2.11 shows the results of a series of numerical simulations, scanning across a range of values for $\tilde{\omega}_0$, while limiting $\tilde{\Delta}$ to one of four values and keeping the coupling constant fixed at $k = 40$ (the four dashed lines in Fig. 2.10). These plots show the long time system behavior of the bulk order parameter r defined in Eq. (2.17). Vertical dashed lines indicate the values of $\tilde{\omega}_0$ where a scan crosses one of
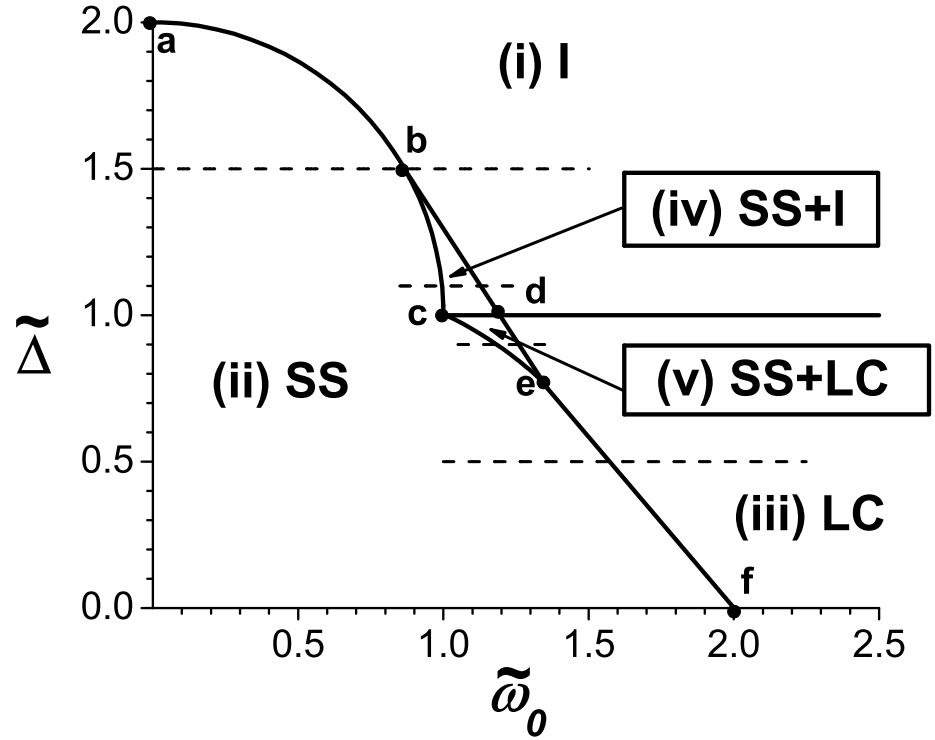
Figure 2.10: Phase diagram in $(\tilde{\omega}_0, \tilde{\Delta})$ parameter space showing regions correspond-ing to different attractor types denoted by I (incoherent steady state attractor at $r = 0$), SS (steady state attractor with $r > 0$), and LC (limit cycle attractor corresponding to time periodic variation of r). Bifurcations of these attractors occur as the region boundaries are crossed [39]. The dashed horizontal lines at $\tilde{\Delta} = 1.5, 1.1, 0.9$ and 0.5 correspond to the scans of parameter $\tilde{\omega}_0$ shown in Fig. 2.11.

the boundaries in Fig. 2.10. Results for the time average of r from theta formulation runs are plotted as solid squares when the attracting solutions are apparently steady states. Results of solutions of our reduced formulation equations, Eqs. (2.51) and (2.52), are plotted in green. Vertical bars and the vertical range of the green indicate the range of oscillation of r when the attracting solutions are apparently periodic. In every case where there is only one attractor, the reduced bimodal ensemble formulation data agrees well with the results of the theta formulation simulations, and the expected behaviors from Fig. 2.10 are reproduced:

(a) For $\tilde{\Delta} = 1.5$, we see coherence for $\tilde{\omega}_0$ before point b in Fig. 2.10 and decoherence past it.

(b) For $\tilde{\Delta} = 1.1$, we see only coherence before crossing the boundary segment bc and only decoherence past crossing of boundary segment bd. In between, the reduced formulation equations indicate that both solutions exist, and which value of r the system asymptotes to depends on the initial conditions (*i.e.,* there is hysteresis).

(c) Similarly, for the scan across $\tilde{\Delta} = 0.9$, we see coherence before the boundary ce is crossed and a limit cycles after the boundary de is crossed, while in between, both solutions exist and are arrived at depending on the initial conditions of the simulation.

(d) Finally, for $\tilde{\Delta} = 0.5$, we see coherence before ef is crossed and a limit cycles after.
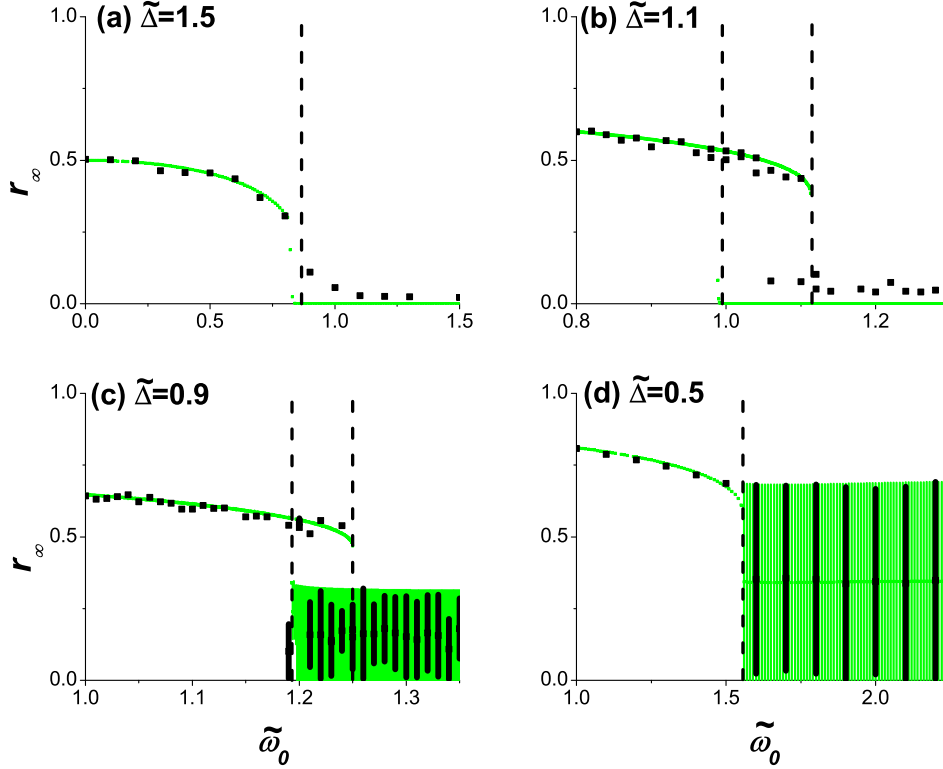
Figure 2.11: Long-time behavior of r vs. $\tilde{\omega}_0$ for systems simulated using the theta formulation [Eqs. (2.1) and (2.2)], plotted in black, and our ensemble formulation [Eqs. (2.51) and (2.52)], plotted in green, for four different values of $\tilde{\Delta}$: (a) $\tilde{\Delta} = 1.5$, (b) $\tilde{\Delta} = 1.1$, (c) $\tilde{\Delta} = 0.9$ and (d) $\tilde{\Delta} = 0.5$. We discard the first $1,000$ time units of our simulations, time average the results over the next $1,000$ time units [40] and plot the averages as solid squares. When the trajectories are apparently limit cycles, the results are plotted as vertical bars indicating the range of r values in the oscillation. Vertical dashed lines represent the region boundaries of Fig. 2.10. The coupling strength k was held fixed at $k = 40$. Simulations were performed on the uniform in-degree network introduced in Sec. 2.2.2. Where needed, simulations in this figure were run twice, once starting from an incoherent state and again from a coherent initial condition (obtained by pre-running the simulations for large k).

We note that our numerical theta formulation data in Fig. 2.11(b) does not show all the attractors across the entire hysteretic range of region (iv). In Fig. 2.11(b), both solutions are observed for the theta formulation simulations only towards the right edge of region (iv). Since the ensemble formulation equations capture both attractors, we postulate that the incoherent attractor can be close enough to its basin boundary that the noise inherent in the theta formulation simulations is enough to knock the system into the coherent attractor for most values of $\tilde{\omega}_0$ in the left part of region (iv).

Support for this view is provided in Figs. 2.12 and 2.13. Figures 2.12(a) and 2.13(a) show polar polots in $(\tilde{a}, \psi)$ of orbits of our reduced formulation with the inital value of $\tilde{a}$ set to $\tilde{a} = 0.5$ for different initial values of ψ in the case where $\tilde{\Delta} = 1.1$, corresponding to Fig. 2.11(b). Figure 2.12 is for $\tilde{\omega}_0 = 1.10$ and Fig. 2.13 is for $\tilde{\omega}_0 = 1.05$. Orbits tending to the I attractor are plotted (*cf.* Fig. 2.11b) as red curves, while orbits lending to the SS attractor are plotted as blue curves. Grey dots mark the attractors and a saddle point. Note that the basin of the I attractor is substantially smaller at $\tilde{\omega}_0 = 1.05$ (Fig. 2.13(a)) as compared to $\tilde{\omega}_0 = 1.10$ (Fig. 2.12(a)). Also, note that the boundary separating these two attractors is apparently the stable manifold of a saddle steady state and that the left and right arms of the saddle's unstable manifold go directly to the I and SS attractors, respectively. Figures 2.12(b) and (c) show blown up regions centered around the SS attractor (Fig. 2.12(b)) and around the I attractor (Fig. 2.12(c)), where the regions are indicated by the rectangles in Fig. 2.12(a). The black curves plotted in Figs. 2.12(b and c) correspond to the theta formulation orbits initialized

41
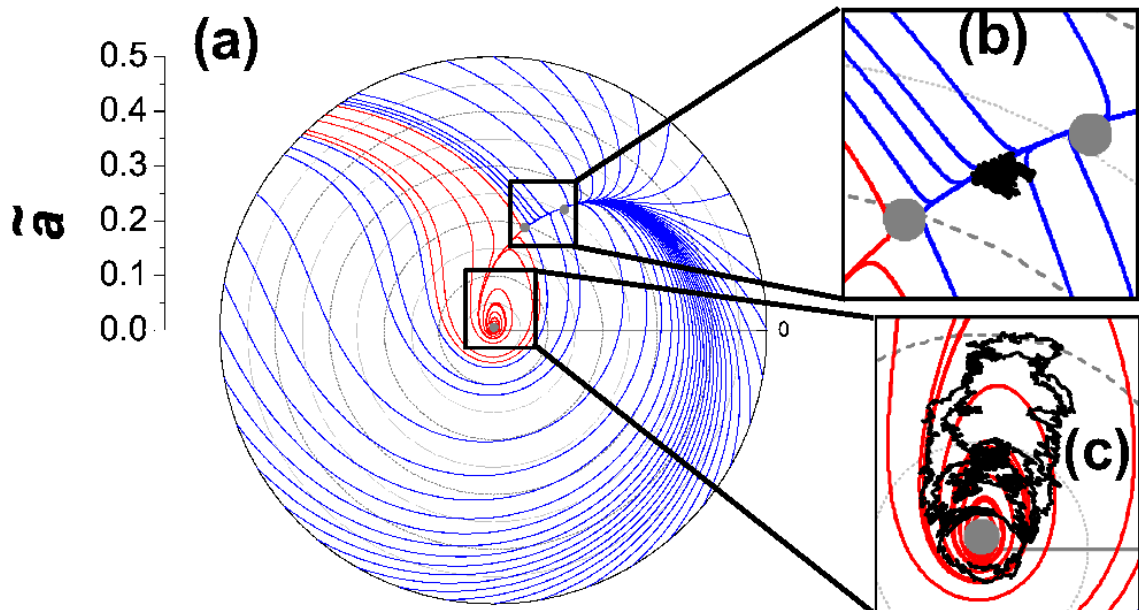
Figure 2.12: Polar plot of $(\tilde{a}, \psi)$ for a variety of initial conditions for $\tilde{\Delta} = 1.1$ and $\tilde{\omega}_0 = 1.10$. The solid lines represent simulations performed using our reduced ensemble equations [Eqs. (2.51) and (2.52)] and are color-coded to indicate which attractor each simulation ended on (blue for synchronized steady-state, red for incoherent). The locations of each attractor and of a saddle point are marked by grey dots. The regions surrounding each attractor are blown up in (b) (SS) and (c) (I), with orbits from theta formulation simulations [Eq. (2.1)] shown in black with transients removed.
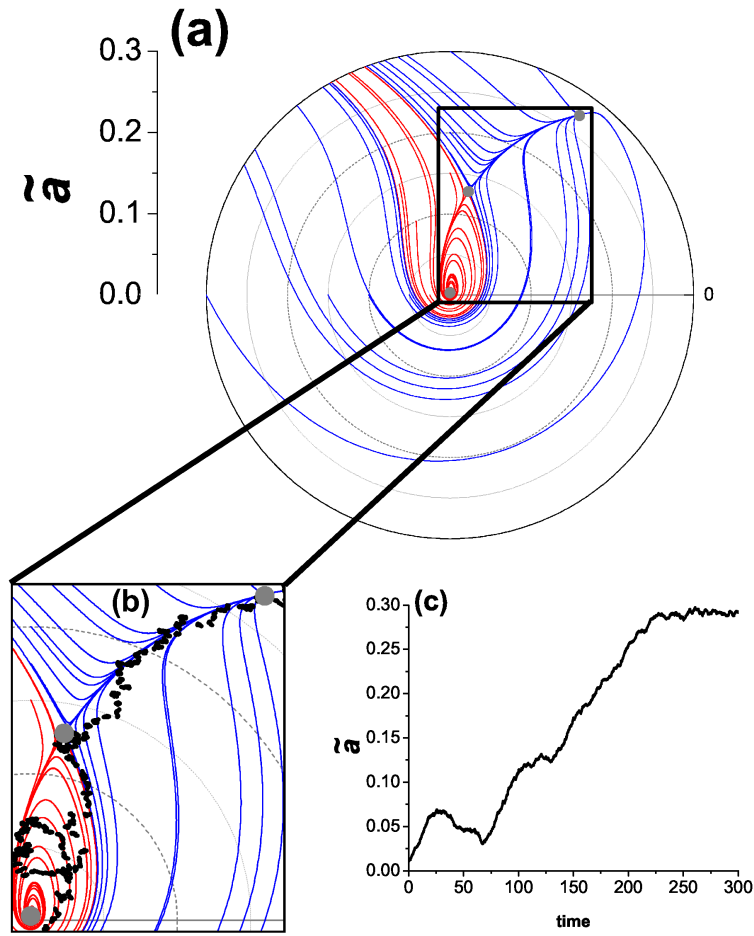
Figure 2.13: Polar plot of $(\tilde{a}, \psi)$ for a variety of initial conditions for $\tilde{\Delta} = 1.1$ and $\tilde{\omega}_0 = 1.05$. The solid lines represent simulations performed using our reduced ensemble equations [Eqs. (2.51) and (2.52)] and are color-coded to indicate which attractor each simulation ended on (blue for synchronized steady-state, red for incoherent). The location of each attractor and of the saddle point is marked by a grey dot. (b) A magnification of the region of interest, with points on the orbit of a theta formulation simulation [Eq. (2.1)] plotted in black, showing the system starting in the incoherent attractor and escaping to the steady-state attractor. (c) $\tilde{a}$ plotted vs. time for the same theta formulation simulation plotted in (b).

43

near the I attractor and near the SS attractor. We see that, although the points stay near their attractors, there is noticeable scatter reflecting the existence of noise.

In Figs. 2.13(b) and (c), we plot points on a theta formulation simulation orbit that was initialized incoherently. As shown, although this orbit initially stays close to the I attractor, it is eventually kicked by noise fluctuations into the SS basin in the vicinity of the boundary saddle and then goes to the SS attractor closely following the right arm of the saddle's unstable manifold. Furthermore, we note that this mode of escape from the I attractor to the SS attractor is characteristic of what is to be expected in a noisy environment [41].

We have also obtained results for our Erdös-Renyi network (described in Sec. 2.2.2), plotted in Fig. 2.14 as red points. Here, we know that the nodes have varying in-degrees (see Fig. 2.1), and thus Eq. (2.46) cannot exactly hold. Figure 2.14 shows, however, that the reduced formulation remains an excellent approximation, with the Erdös-Renyi network exhibiting nearly identical behavior as compared to the uniform in-degree case.

2.5   Conclusion

We summarize our main results by referring to the three advantages of our formulation that were claimed in Sec. 2.2.1,

(i) *The time evolution of the reduced ensemble system is much smoother than is the case for Eq. (2.1), and thus numerical integrations of the reduced system can be done faster using much larger time steps.* Figs. 2.3-2.5 show that,

44
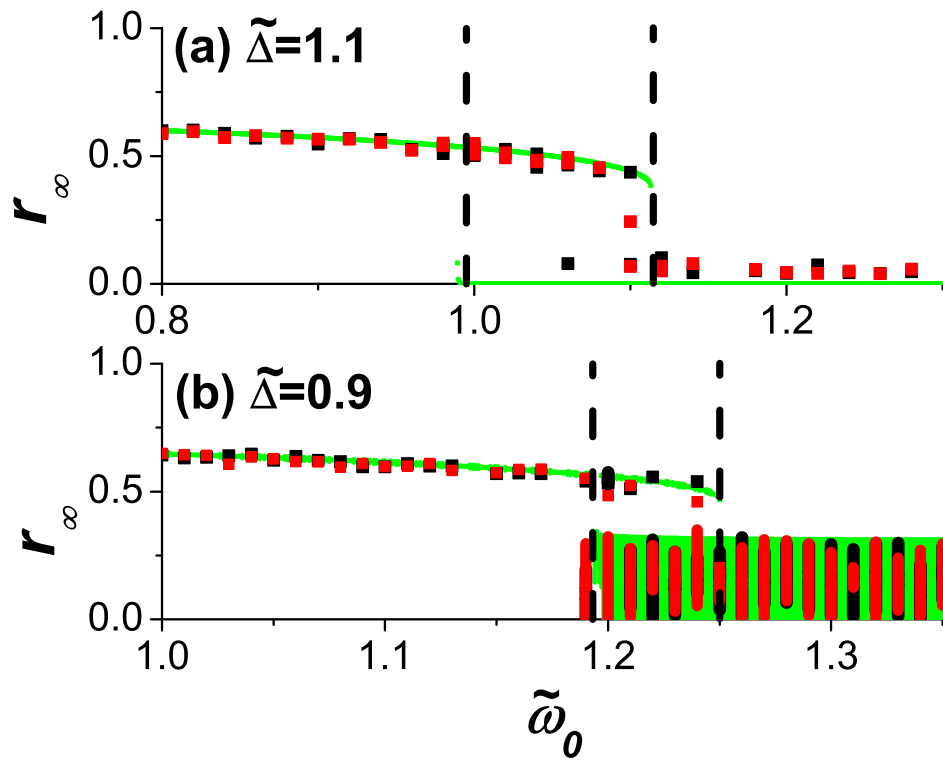
Figure 2.14: Two of the graphs from Fig. 2.11 re-plotted to include simulations done on the Erdös-Renyi network (red) introduced in Sec. 2.2.2.

especially at larger values of r, our ensemble formulation reproduces the dynamics of the theta formulation. This result was obtained using a time step ten times larger than that used for each theta formulation simulation, thus drastically reducing runtime. At small values of r, our results suggest that the noise inherent to the theta formulation simulations is dominant over the dynamics. Thus, to obtain usable data in this regime with the theta formulation simulations would require averaging multiple runs. In contrast, ensemble formulation simulations are effectively noiseless, requiring no averaging.

(ii) *In certain cases the reduced ensemble description is amenable to analysis that can enhance understanding and facilitate approximate quantitative results.* In Sec. 2.3.3, we solve our ensemble formulation equations for the case of steady state, yielding an exact transcendental solution [Eq. (2.20)] describing the coherent fixed points in the unimodal system for $k > k_c$. In Sec. 2.3.4, we apply the maximum eigenvalue approximation [Eq. (2.24)] to our network connectivity matrices to obtain simplified results which agree well with theta and ensemble formulation simulations to the extent that the maximum eigenvalue approximation is valid (see Fig. 2.6).

(iii) *For the special case of networks with uniform in-degree, the reduced ensemble description leads to a massive reduction in dimensionality from $\mathcal{O}(N)$ to $\mathcal{O}(1)$.* In Sec. 2.3.5, by applying the ansatz of Eq. (2.30) we reduce our number of equations from N to 1, obtaining a generalization of Eq. (10) of Ref. [8] [Eq. (2.32)]. Figure 2.8 lends support to the validity of this ansatz, showing

that the dynamics match, and that our ensemble formulation system rapidly converges on the manifold described by Eq. (2.30). Exploring the case of a bimodal frequency distribution, in Sec. 2.4.2, applying a similar ansatz to Eq. (2.30) reduces our system of equations from $2N$ complex ODEs to 2 real ODEs. Interestingly, the results using our reduced bimodal ensemble formulation [Eqs. (2.51) and (2.52)] match not only our theta formulation results for the uniform in-degree network, but, as shown in Fig. 2.14, the results for our Erdös-Renyi network as well.

Chapter 3:   Lyapunov Spectrum of the Kuramoto Model

3.1   Overview

We compute and analyze the Lyapunov spectrum of the Kuramoto model. We find that the behavior of most of the exponents in the spectrum is well-described as arising from the motion of single oscillators subject to the system's mean field. We believe that similar behavior should occur generally for other large systems with mean-field-type coupling.

3.2   Introduction

In the study of coupled oscillator systems, perhaps the simplest and most common model is one developed by Kuramoto [3–7]. In its original form, each oscillator i is represented by a phase angle $\theta_j \in [0, 2\pi)$ whose dynamics are given by

$$\frac{d\theta_j(t)}{dt} = \omega_j + \frac{k}{N} \sum_{l=1}^{N} \sin\left(\theta_l(t) - \theta_j(t)\right), \qquad (3.1)$$

where ω_j is each oscillator's "natural frequency." The basic phase oscillator description of the Kuramoto model has been adapted in a myriad of ways, including the introduction of network coupling, as described in Chapter 2, external global drive [42], time delayed coupling [24], excitable dynamics [20], noise [21], bimodal frequency

distributions [22], phase resetting [25] and discrete-time dynamics [43], and it has been used to study systems as diverse as London's Millennium bridge [17], circadian rhythm [18], neuronal population interactions [16], birdsong [15], Josephson junctions [19], and chimera states [28–33], and its global dynamics have been well studied [8]. This chapter is focused on characterizing the microscopic behavior of the system, Eq. (3.1), by computation and analysis of its Lyapunov spectrum. This topic has previously been addressed by Popovych, Maestrenko and Tass, who looked at the high-dimensional dynamics for an equally-spaced distribution of natural frequencies [44], and by Wolfrum and Omel'chenko, who investigated in the conext of chimera states for the Kuramoto model with phase lag and globally equal natural frequencies [45]. In this chapter we consider systems with natural frequencies selected randomly from a distribution $g(\omega)$. We will mostly consider cases where $g(\omega)$ is Lorentzian, that is, of the form

$$g(\omega) = \frac{1}{\pi} \frac{\Delta}{(\omega - \Omega))^2 + \Delta^2}, \tag{3.2}$$

but we will also show that our results are applicable to other frequency distributions as well, namely ones of Gaussian form. Our focus will also be on the case where $N >> 1$, a regime where the macroscopic dynamics were analytically described in Ref. [8]. One of our main results is that, past the critical synchrony coupling point, most of the exponents in the Lyapunov spectrum can be well-described as arising from the dynamics of individual oscillators forced by the mean field. We believe that this result should be fairly universal in the sense that it should hold generally for many large systems of heterogeneous dynamical units that interact via

mean-field-type coupling.

Our chapter is organized as follows. Section 3.3 reviews background on the macroscopic dynamics of the Kuramoto system. Section 3.4 presents and discusses our results on the Lyapunov spectrum. Section 3.5 discusses our analytical mean-field approach to calculating Lyapunov exponents and compares it with the numerical results. Conclusions are listed in Sec. 3.6.

3.3   Macroscopic Description

The Kuramoto model can characterized in terms of a complex "order parameter" R,

$$R \equiv \rho e^{i\Theta} \equiv \frac{1}{N} \sum_{j=1}^{N} e^{i\theta_j}. \tag{3.3}$$

Reference [8] showed that for $N >> 1$, and $g(\omega)$ given by Eq. (3.2) (which is the case we usually consider) with suitable initial conditions, the macroscopic dynamics are described by

$$\frac{d\rho}{dt} = -\Delta\rho - \frac{k}{2}\left(\rho^3 - \rho\right), \tag{3.4}$$

and

$$\frac{d\Theta}{dt} = \Omega. \tag{3.5}$$

The fixed points of Eq. (3.4) correspond to steady state solutions for the global level of synchrony. The first fixed point $\rho = 0$ corresponds to a completely incoherent state where the the distribution of oscillator phase angles is uniform and where the motion of each oscillator is uncorrelated with that of every other. For coupling strength k above the critical coupling strength $k_c = 2\Delta$, a second solution exists

where $\rho > 0$,

$$\rho = \sqrt{1 - \frac{2\Delta}{k}} \text{ for } k > 2\Delta \equiv k_c, \tag{3.6}$$

corresponding to a partially synchronized state, with oscillator angles clustered together to a degree characterized by ρ.

For trajectories where ρ is fixed, we consider perturbations of the form $\vec{v} = (\delta\rho, \delta\Theta)^T \exp(ht)$ and find that the Lyapunov exponents and vectors for Eqs. (3.4)-(3.5) are

$$\vec{v}_0 = \begin{pmatrix} 0 \\ 1 \end{pmatrix} \Rightarrow h_0 = 0, \tag{3.7}$$

which corresponds to a perturbation which uniformly shifts the phase angle while leaving the level of synchrony constant, and

$$\vec{v}_L = \begin{pmatrix} 1 \\ 0 \end{pmatrix} \Rightarrow h_L(\rho) = -\Delta - \frac{k}{2} \left(3\rho^2 - 1\right), \tag{3.8}$$

which corresponds to a perturbation where the level of synchrony changes but Θ remains fixed. Evaluating Eq. (3.8) for the two fixed points of Eq. (3.4), the nonzero Lyapunov exponent corresponding to the incoherent solution $\rho = 0$ is

$$h_L^I = \frac{k}{2} - \Delta = \frac{1}{2}\left(k - k_c\right), \tag{3.9}$$

while, for the partially synchronized state with ρ given by Eq. (3.6),

$$h_L^S = 2\Delta - k = k_c - k \text{ for } k > 2\Delta = k_c. \tag{3.10}$$

The exponent h_L^S is negative for its entire range of validity, indicating that the partially synchronized state, when it exists, is always stable and attracting; the

incoherent state is stable ($h_L^S < 0$) for $k < k_c$ and unstable ($h_L^S > 0$) for $k > k_c$.

In Fig. 3.1 a system of $N = 10^5$ oscillators is initialized close to the incoherent state and allowed to evolve. After a short initial period, $t \lesssim 0.5$, the rate at which ρ initially diverges from the incoherent state is given by h_L^I (dashed line in Fig. 3.1a), and as the system approaches the partially coherent state, the rate at which it converges is given by h_L^S (dashed line in Fig. 3.1b).

3.4   Microscopic Lyapunov Spectrum

The Jacobian of Eq. (3.1) is

$$J_{mn}(\vec{\theta}) = \frac{k}{N} \begin{cases} -\sum_{j \neq m} \cos\left(\theta_j(t) - \theta_m(t)\right) & , n = m, \\ \cos\left(\theta_n(t) - \theta_m(t)\right) & , n \neq m, \end{cases} \tag{3.11}$$

where $d\delta\vec{\theta}/dt = J\delta\vec{\theta}$. The rows of J each sum to zero, thus guaranteeing for all trajectories $\vec{\theta}(t)$ that the vector

$$\vec{v}_0 \equiv \frac{1}{\sqrt{N}} \left(1, 1, 1, 1, ..., 1\right)^T, \tag{3.12}$$

is a Lyapunov vector for the system associated with the Lyapunov exponent $h = h_0 \equiv 0$. Physically, this perturbation points in the direction of a uniform rotation of all oscillators in the system and matches the description of the Lyapunov vector $\vec{v}_0$ described in Sec. 3.3.

Numerical results for the other $N - 1$ exponents for a range of coupling strengths k were computed. This was done by evolving a matrix V, whose columns span the entire N-dimensional phase space, forward in time by the equation of motion $dV/dt = JV$ [46,47], and periodically orthonormalizing the columns of V using

52
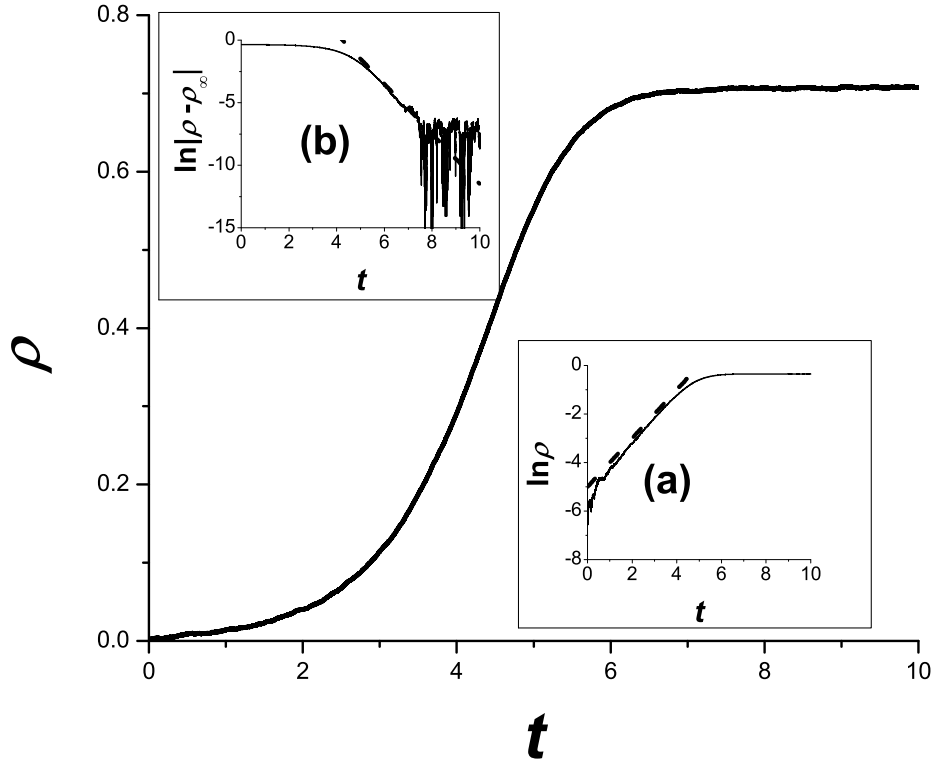
Figure 3.1: The magnitude ρ of the order parameter R vs. time t for a system of $N = 10^5$ oscillators whose natural frequencies $\{\omega_j\}$ were selected from a Lorentzian distribution of width $\Delta = 1$ (so $k_c = 2$) and center $\Omega = 0$. The coupling strength was set to $k = 4 = 2k_c$. The system was initialized in a random (incoherent) state and was evolved according to Eq. (3.1). Insets show on a log-linear scale the distance of the system from the two steady-state solutions: (a) the unstable incoherent state $\rho = 0$ and (b) the stable coherent state $\rho = 1/\sqrt{2}$, as calculated from Eq. (3.6). The slopes of the dashed lines correspond to the predicted Lyapunov exponents h_L^I and h_L^S.

the QR decomposition [48]. After a sufficiently long run time, the decomposition of this matrix, $V = QR$, provides the Lyapunov exponents of the dynamics as the diagonal elements of the upper-triangular matrix R, $h_n = R_{nn}$, and the Lyapunov vectors associated with each exponent as the columns of the orthonormalized matrix Q ($\vec{v}_n$ is the nth column of Q).

Figure 3.2 plots these exponents for a particular random realization of the natural frequencies, for k varied in the range $0 < k < 10$, in a system of $N = 200$ oscillators. Tracing single Lyapunov exponents in Fig. 3.2 (solid curves) as k is increased, we find that the exponents appear to have a common asymptotic relation with k (except for the single exponent whose value is always zero and whose associated direction is given by Eq. (3.12)). As k decreases, we find that most exponents increase monotonically to near zero, at which point they remain near zero for all k less than that value. The dependence of the nth largest exponent h_n as it approaches zero and the critical k value below which h_n is near zero are each different for different n. We will explore these properties further in Sec. 3.5.

3.4.1 Average Lyapunov Spectrum

Averaging over 2500 realizations (different initial conditions and selections for $\{\omega_j\}$), Fig. 3.3 (dark colored curves) shows the distributions of Lyapunov exponents in this spectrum for $k = 1.0 < k_c$, $k = 2.0 = k_c$, and two values for $k > k_c$: $k = 4$ and $k = 10$. For $k > k_c$ the predominant features of these distributions is the presence of two peaks: one peak centered around $h = 0$ and another peak centered
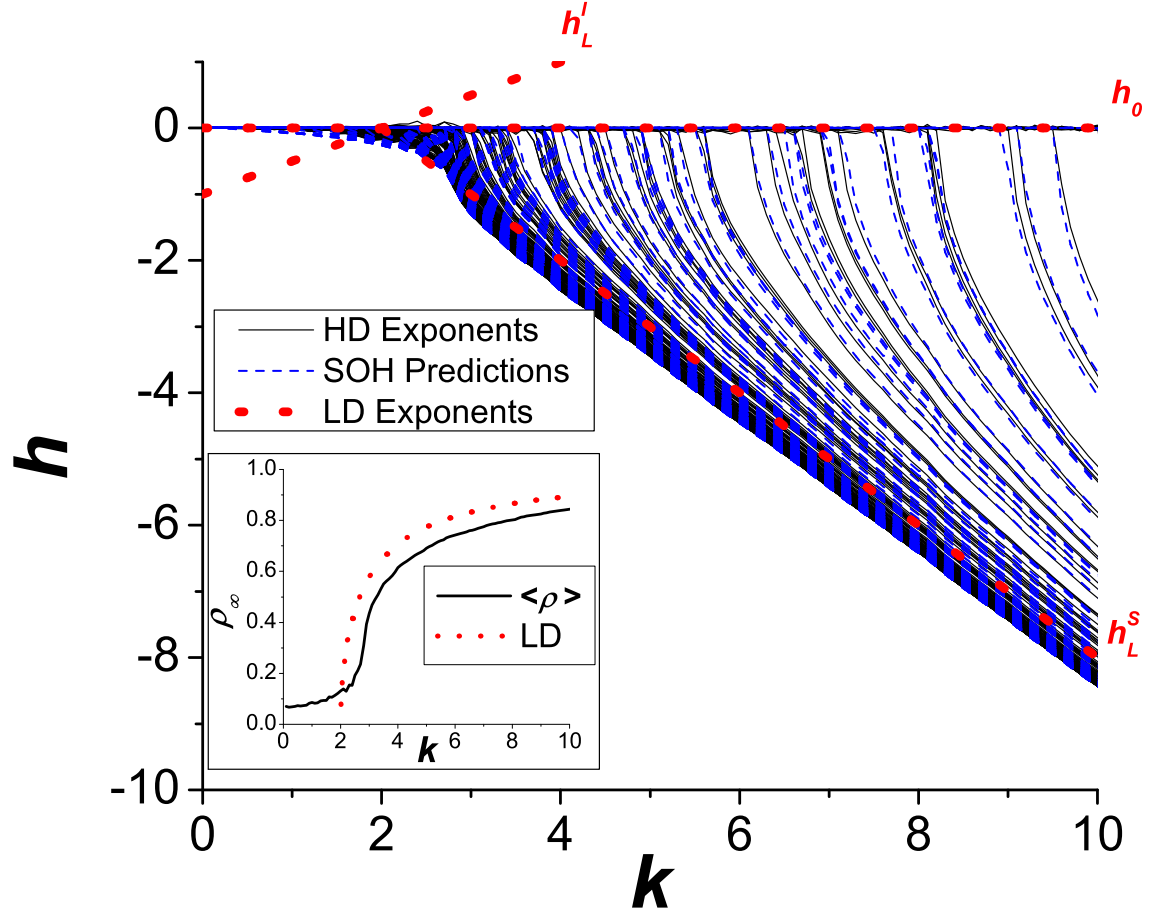
Figure 3.2: The Lyapunov spectrum plotted vs. coupling strength k for one realization of a system of $N = 200$ oscillators whose natural frequencies were sampled randomly from a Lorentzian distribution with width $\Delta = 1$. Black solid curves: the computed Lyapunov spectrum based on the evolution of Eq. (3.1). Blue dashed curves: the Lyapunov spectrum as predicted using Eq. (3.19) of Sec. 3.5. Red dotted lines: the low dimensional spectrum, Eqs. (3.7), (3.9) and (3.10). Inset: Long-time values of the magnitude ρ of the order parameter R plotted vs. k. Black solid curve: average long-time value of ρ of the system as calculated using Eq. (3.3). Red dots: Eq. (3.6) as the synchronized steady state solution to the low-dimensional equation, Eq. (3.4).
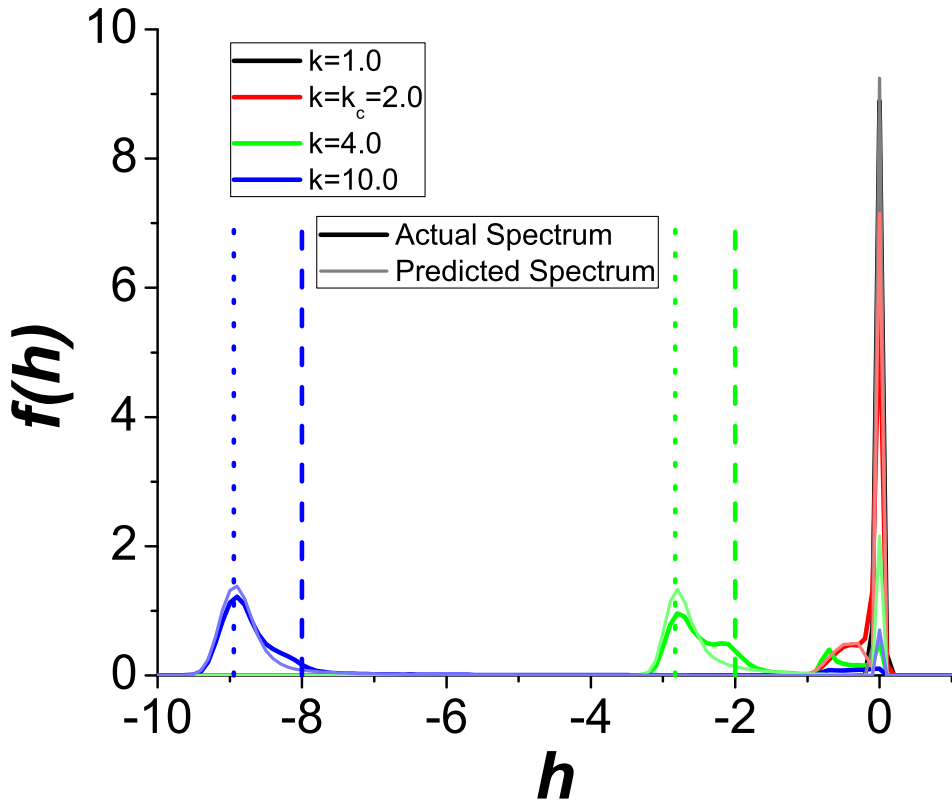
Figure 3.3: Histograms of the average Lyapunov spectra for approximately 2500 realizations of our system (different values of ω_j each time). Separate curves are plotted for four values of the coupling strength k: $k = 1$ (black), which is below k_c, $k = 2 = k_c$ (red), $k = 4$ (green), which is twice k_c, and $k = 10$ (blue), which is much larger than k_c. Histograms for the expected Lyapunov exponents according to the single oscillator hypothesis of Sec. 3.5 are plotted in faded colors. The vertical dashed lines indicate the locations of the low-dimensional Lyapunov exponent h_L^S (Eq. (3.10)) for each curve, $k > k_c$, while the vertical dotted lines indicate the locations of the asymptotic value h_∞ (Eq. (3.21)).
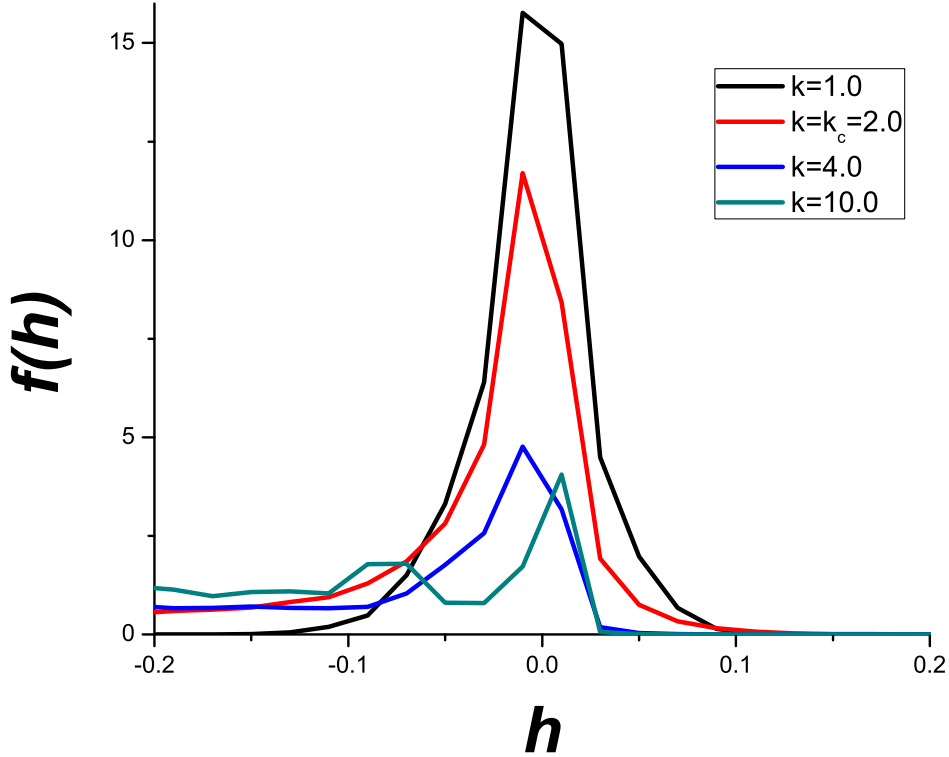
Figure 3.4: Figure 3.3 enlarged around $h = 0$ using a smaller bin size.

around a negative value, whose magnitude increases with k. For $k = 4$, we also note the presence of a smaller peak in the distributions around values of h that are less negative than the primary nonzero peak. Also, for $k = 10$, similar to the $k = 4$ result, we note the hint of an enhanced population component around a values of h that is less negative than the h value at the negative peak, but this enhancement is evidently not strong enough to produce another peak.

3.4.2 Near-Zero Exponents

While the macroscopic dynamics of the Kuramoto model are stable around the partially synchronized fixed point, Fig. 3.4 enlarges Fig. 3.3 around $h = 0$ and
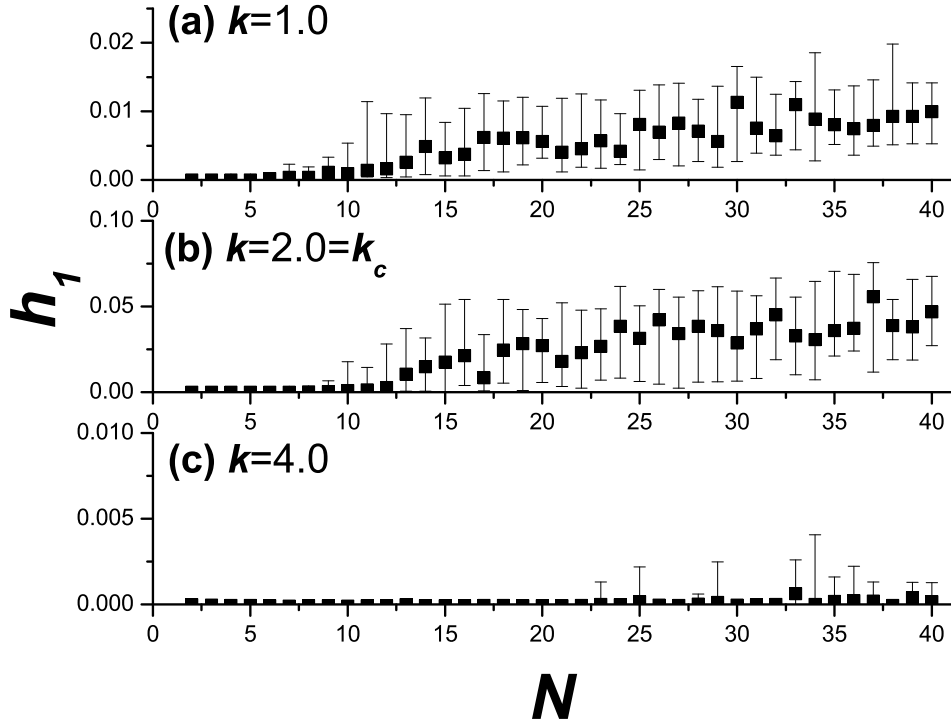
Figure 3.5: Median values of h_1 plotted vs. number of oscillators N for an ensemble of realizations, at three values of coupling strength: (a) $k = 1 < k_c$, (b) $k = 2 = k_c$ and (c) $k = 4 > k_c$. Positive error bars correspond to the range between the second and third quartiles, negative error bars to between the first and second.

shows that for all four k-values investigated, a considerable fraction of exponents are greater than zero, corresponding to chaos in the microscopic dynamics (we have verified that the curves in Fig. 3.4 are stable to increases or decreases in the run times used to calculate the Lyapunov exponents).

Figure 3.5 presents results showing the relationship between the largest Lyapunov exponent h_1 and the system size N for $k = 1 < k_c$, $k = 2 = k_c$ and $k = 4 > k_c$. Specifically, the plotted points and error bars, respectively, show the median h_1 value and the extent of the two middle quartiles obtained from numerical nuns using a
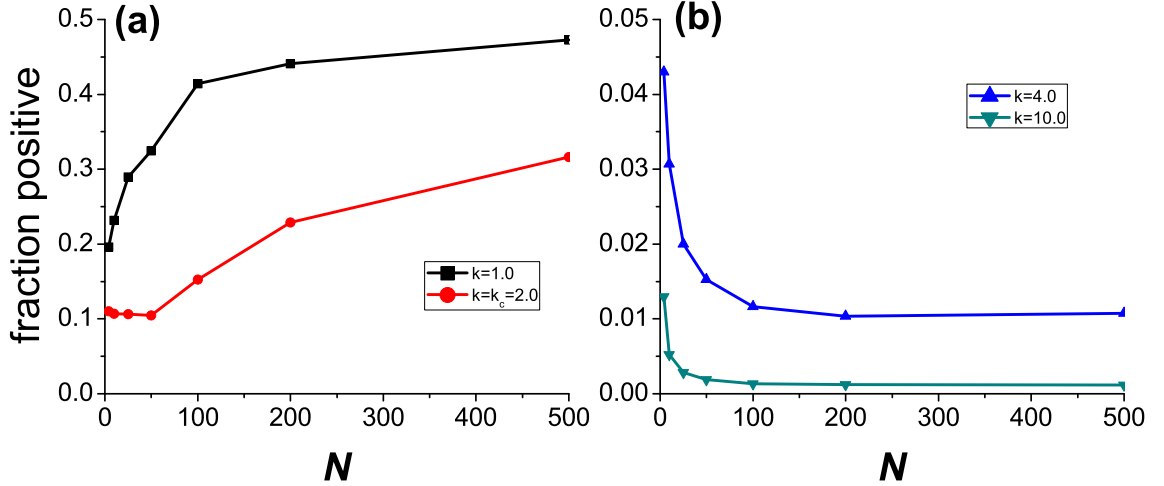
Figure 3.6: Fraction of positive Lyapunov exponents, $h > 0$, for large ensembles of realizations of our system for various values of N at four values of coupling strength k.

large number of realizations of the oscillator frequencies $\{\omega_i\}$. For the case $k = 1$ (Fig. 3.5a), we note that while there is much variation in the values observed for the largest exponent, the negative correlation between system size and largest exponent observed by Popovych and Maistrenko [44] for their system below criticality is not observed. This negative correlation between system size and h_1 was also observed by Wolfrum and Omel'chenko [45] in their study of chimera states in a Kuramoto model with phase lag and equal natural frequencies for all oscillators. In contrast, while we observe that the median value of h_1 grows initially with N, it does not grow significantly for $N \gtrsim 15$. The same behavior is seen for $k = k_c$ (Fig. 3.5b). In Fig. 3.5c, where $k > k_c$, the median value of h_1 is near zero, with no discernible relation between h_1 and system size [49].

In addition, for Popovych and Maistrenko [44] and Wolfrum and Omel'chenko

[45] each found for their systems that the proportion of Lyapunov exponents which were positive was consistent as system size was varied, up to $N = 80$ for Popovych and Maistrenko, and up to $N = 50$ for Wolfrum and Omel'chenko. In Fig. 3.6, we show that the fraction of Lyapunov exponents observed to be positive over large ensembles changed dramatically in the range $N < 100$: the fraction of positive exponents increases with system size for $k \leq k_c$ (Fig. 3.6a), leveling off only for $N \gtrsim 200$, and the fraction decreases with system size for $k > k_c$ (Fig. 3.6b), where the fraction is constant for $N \gtrsim 100$.

3.4.3 Comparison with Macroscopic Dynamics

While there is no *a priori* general reason to expect a precise correspondence between the perturbation dynamics obtained from the microscopic and macroscopic descriptions of a system, it is still of interest to compare them. As we have already noted, an h_0 corresponding to a uniform rotation of all the oscillator phases may be obtained as an eigenvalue of the Jacobian for both the low dimensional system of equations (Eqs. (3.4)-(3.5)) and the high dimensional system (Eq. (3.1)). As for h_L^I given by Eq. (3.9), we observe for $k < k_c$ from Fig. 3.2 that it is substantially more negative than the microscopic Lyapunov exponents (for $k < k_c$), and the microscopic and macroscopic Lyapunov numbers have qualitatively different behavior. However, considering h_L^S for $k > k_c$, given by Eq. (3.10), Fig. 3.2 shows that for large k, the value of h_L^S scales with k at the same rate as the bulk of the microscopic spectrum. On the other hand, in Fig. 3.3, we see that h_L^S is significantly less negative than the

bulk of the nonzero exponents.

To investigate further, we seek to characterize how "macroscopic" each high-dimensional Lyapunov vector is. Given a perturbation $\delta\vec{\theta}$, we may linearize Eq. (3.3) to find the effect such a perturbation on the complex order parameter:

$$\delta R = \frac{1}{N} \sum_{j=1}^{N} e^{i\theta_j} i \delta\theta_j. \tag{3.13}$$

To compare the relative effect on R from perturbations in the directions of the Lyapunov vectors, we will thus compare the magnitudes of the quantities $\sum_{j=1}^{N} e^{i\theta_j} v_{nj}$. Using $\vec{v}_0$ given by Eq. (3.12) as a point of reference, we thus define the "macroscopicness" μ_n of a Lyapunov vector $\vec{v}_n$ to be:

$$\mu_n = \frac{|\sum_{j=1}^{N} e^{i\theta_j} v_{nj}|}{|\sum_{j=1}^{N} e^{i\theta_j} v_{0j}|} = \frac{|\sum_{j=1}^{N} e^{i\theta_j} v_{nj}|}{\rho\sqrt{N}} \tag{3.14}$$

Figure 3.7 plots μ_n for each Lyapunov vector vs. its associated Lyapunov exponent for a single system of $N = 500$ oscillators at $k = 4 > k_c$, showing that the only significantly macroscopic perturbation of the system is the zero vector, with the largest nontrivial μ having a value of only about 0.2. Additional numerical calculations have shown this value to be a finite size effect, and (aside from the vector $\vec{v}_0$ with $h = 0$, $\mu \equiv 1$) the largest μ varies roughly inversely with N. Furthermore, we note the general trend that, as h becomes more negative, μ decreases, with the least macroscopic vectors corresponding to the most negative Lyapunov exponent. Together with Fig. 3.3, this leads to conclusion that the trend we observed between h_L^S and the bulk of the microscopic Lyapunov exponents for large k is coincidental and that Lyapunov vectors with exponents around this value have no greater connection to the macroscopic dynamics than any other vectors.
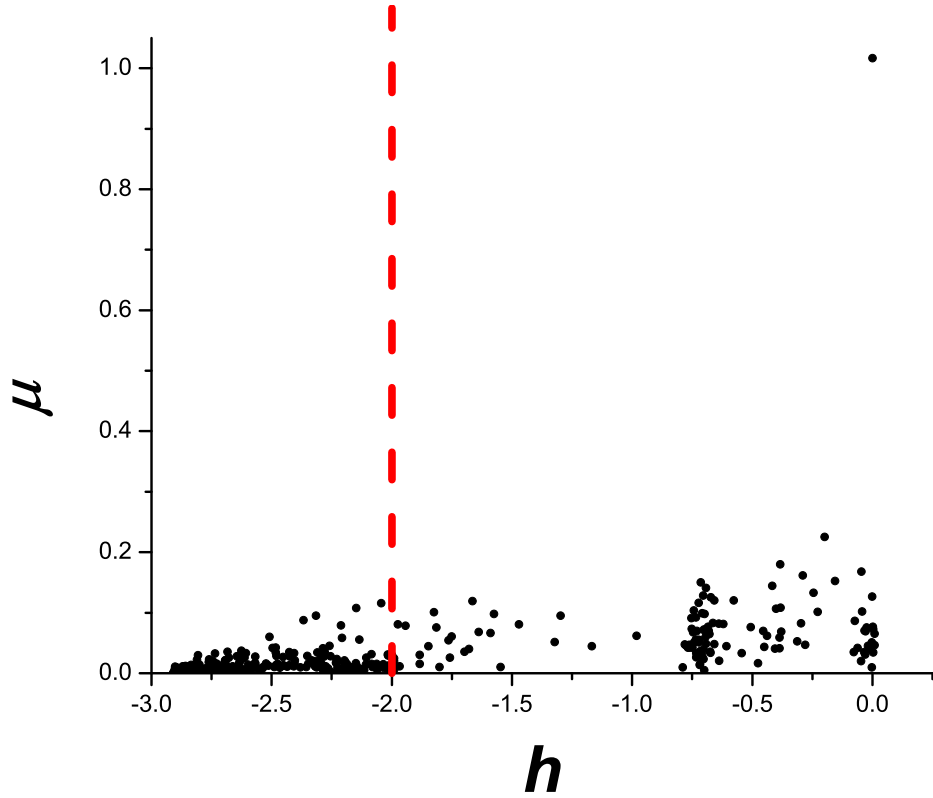
Figure 3.7: Scatterplot showing the macroscopicness of each Lyapunov vector, as computed from Eq. (3.14), vs. each vector's associated Lyapunov number h_i for a single realization of a system of $N = 500$ oscillators with coupling strength $k = 4$. The dashed red line correspond to the low dimensional Lyapunov exponent h_L^S.

3.5 Single Oscillator Approximation of Lyapunov Vectors and Exponents Based on the Behavior in the Mean Field

Equation (3.1) may be rewritten as

$$\frac{d\theta_j(t)}{dt} = \omega_j + k\rho(t)\sin\left(\Theta(t) - \theta_j(t)\right).$$
(3.15)

From Eqs. (3.4)-(3.5), we expect that at long times, ρ will be fixed and Θ will vary with a constant rate. Thus, seeking values of θ_j for which

$$\Omega = \frac{d\Theta}{dt} = \frac{d\theta_j}{dt} = \omega_j + k\rho\sin\left(\Theta - \theta_j\right).$$
(3.16)

We call oscillators for which $k\rho > |\omega_j - \Omega|$ "locked," and these oscillators have solutions to Eq. (3.16) given by

$$\theta_j^0 = \sin^{-1}\left(\frac{\omega_j - \Omega}{k\rho}\right) + \Theta$$
(3.17)

while "unlocked" oscillators have $\theta_j(t)$ either increasing or decreasing monotonically with time at a constant average rate. We now show that, for $N \gg 1$, most of the Lyapunov exponents correspond to perturbations of single oscillators forced by the mean field and represented by the Lyapunov vectors $\{\vec{v}_j^{SOH}\}$ with one entry of unity and the rest zero:

$$\vec{v}_j^{SOH} = \left(\delta_{1j}, \delta_{2j}, \delta_{3j}, \delta_{4j}, ..., \delta_{Nj}\right)^T.$$
(3.18)

Figures 3.8(a,b) show, via greyscale heat maps, the extent to which these predicted Lyapunov vectors match the actual Lyapunov vectors of the system. The vertical and horizontal axes are indices n of Lyapunov vectors ordered so that
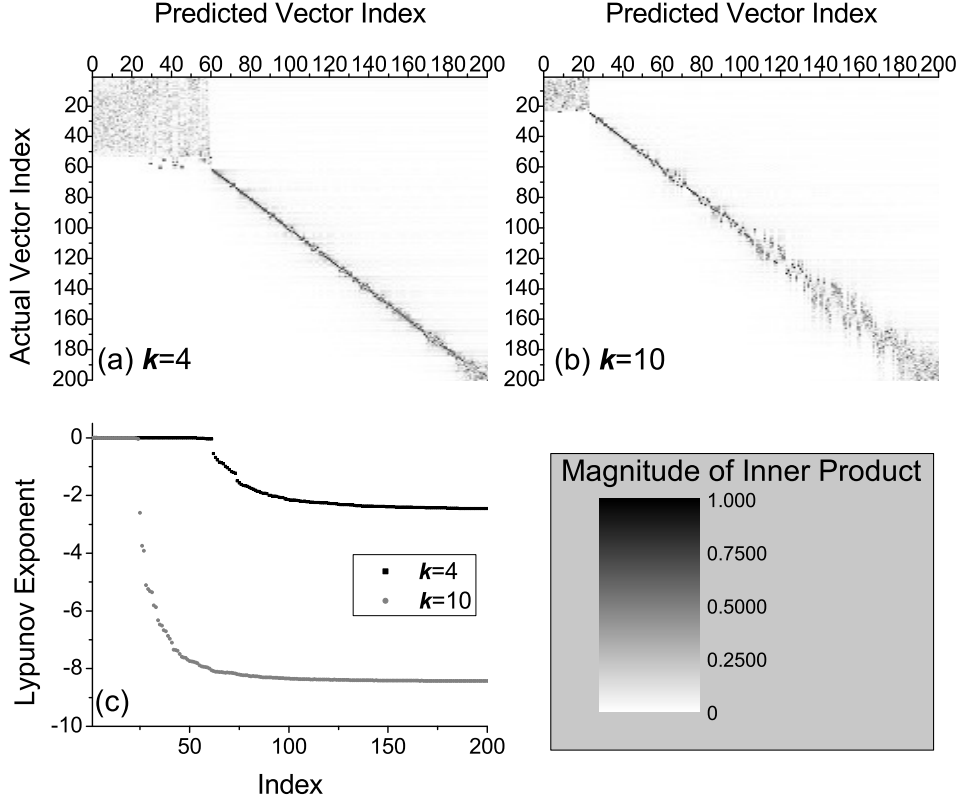
Figure 3.8: (a) Grayscale heat map showing the magnitudes of the inner products (darker color indicates greater magnitude) of each of the $N + 1$ predicted Lyapunov vectors—$\vec{v}_0$ corresponding to Eq. (3.12) and $\vec{v}_1^{SOH}$-$\vec{v}_N^{SOH}$ corresponding to Eq. (3.18)—with the N Lyapunov vectors of our system of $N = 200$ oscillators for a coupling strength of $k = 4$. Each set of vectors was ranked by their corresponding Lyapunov exponent, $h_n > h_{n+1}$. (b) Same as (a) but for $k = 10$. (c) The values of the Lyapunov exponents associated with each of the Lyapunov vectors of the system for (a) and (b). In both cases, $V(0)$, the initial matrix for our algorithm, was generated by selecting $\{V_{mn}(0)\}$ randomly and uniformly from the range $[-1, 1]$, and the calculation runtime was 500 time units.

$h_n > h_{n+1}$, where the h_n's for the vertical scale are from our previously described computations of the Lyapunov spectrum of Eq. (3.1), and the h_n's for the horizontal scale are obtained from the single oscillator hypothesis (Eq. (3.19)). In both cases plotted in Figs. 3.8(a,b), $k = 4$ and $k = 10$, a proportion of the corresponding Lyapunov exponents (plotted in Fig. 3.8(c)) are near zero, and thus that part of the spectra is nearly degenerate. Consequently, the upper-left corners of the Fig. 3.8(a,b) are blocks of seemingly random values. In addition, as seen best in Fig. 3.8(b), the bottom-right corner is somewhat degenerate as well, due to the fact that the most negative Lyapunov exponents have values that are very close to each other as they approach their predicted common asymptotic value observed in Fig. 3.2. In between, however, most of the actual Lyapunov vectors agree well with their corresponding predicted Lyapunov vector $\vec{v}_j^{SOH}$. The lack of perfect agreement is probably due, at least partially, to the fact that the single oscillator hypothesis provides only an approximate solution to the dynamics, since, although $N >> 1$, it is still finite. That being said, we believe that some of the discrepancy observed may also be due to numerical limitations of the algorithm—to differentiate between the nearly degenerate most-negative Lyapunov exponents, our algorithm would have to be run for an extremely long time [50].

Linearizing Eq. (3.15) with respect to θ_j and evaluating at θ_j^0 we obtain a prediction for the Lyapunov exponent of a locked state oscillator j,

$$h_j^{SOH} \simeq -\sqrt{k^2\rho^2 - (\omega_j - \Omega)^2} \ , \ k\rho > |\omega_j - \Omega|. \tag{3.19}$$

Again we note that this is an approximate equation which ignores the finite-N noisy

fluctuations of ρ and Θ. For $k\rho < |\omega_j - \Omega|$, Eq. (3.16) has no solution. In that case, $\theta_j - \Theta$ will be monotonically increasing or decreasing, and since Eq. (3.16) is one-dimensional, the Lyapunov exponent in that case will be

$$h_j^{SOH} = 0 \text{ for } k\rho < |\omega_j - \Omega|. \tag{3.20}$$

The Lyapunov spectrum as predicted by the single oscillator hypothesis was also plotted in Fig. 3.2 (dashed blue curves) and in 3.3 (faded color curves), showing that the majority of exponents are well predicted by the single oscillator hypothesis. The values $h_j(k)$ agree well with those predicted by Eqs. (3.19)-(3.20), and the critical values of k below which $h_i \simeq 0$ are given by $|\omega_j - \Omega|/\rho$. We also find that it is the *single oscillator hypothesis*, not the low dimensional theory, that gives us the asymptotic value for h_i for large k: Inserting the value of ρ given by by Eq. (3.6) into Eq. (3.19), we find the asymptotic value of h_j in the limit $k\rho >> |\omega_j - \Omega|$:

$$h_\infty = \sqrt{k(k_c - k)}. \tag{3.21}$$

Figure 3.3 showed h_∞ as a dotted vertical line, showing that the main nonzero peak for the distributions of Lyapunov exponents is centered around this value h_∞. The width of this peak is a finite size effect, and as the number of oscillators is increased, this peak becomes narrower. This is reflected by comparing Fig. 3.3 and Fig. 3.9, which shows the distribution of Lyapunov exponents for a system of $N = 500$ oscillators.

As a final demonstration, Fig. 3.10 applies the single oscillator hypothesis to the analysis of a system where the natural frequency distribution is Gaussian in form rather than Lorentzian. As expected, the hypothesis does just as well in this
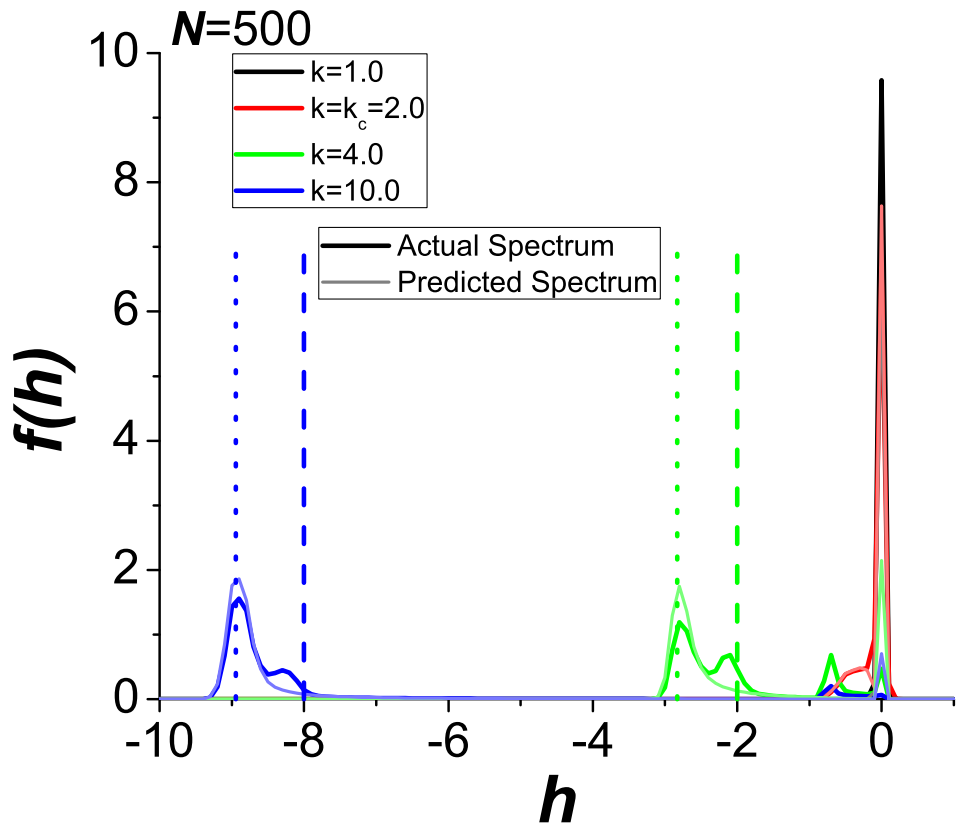
Figure 3.9: Same as Fig. 3.3 but for approximately 1000 realizations of a system of 500 oscillators.
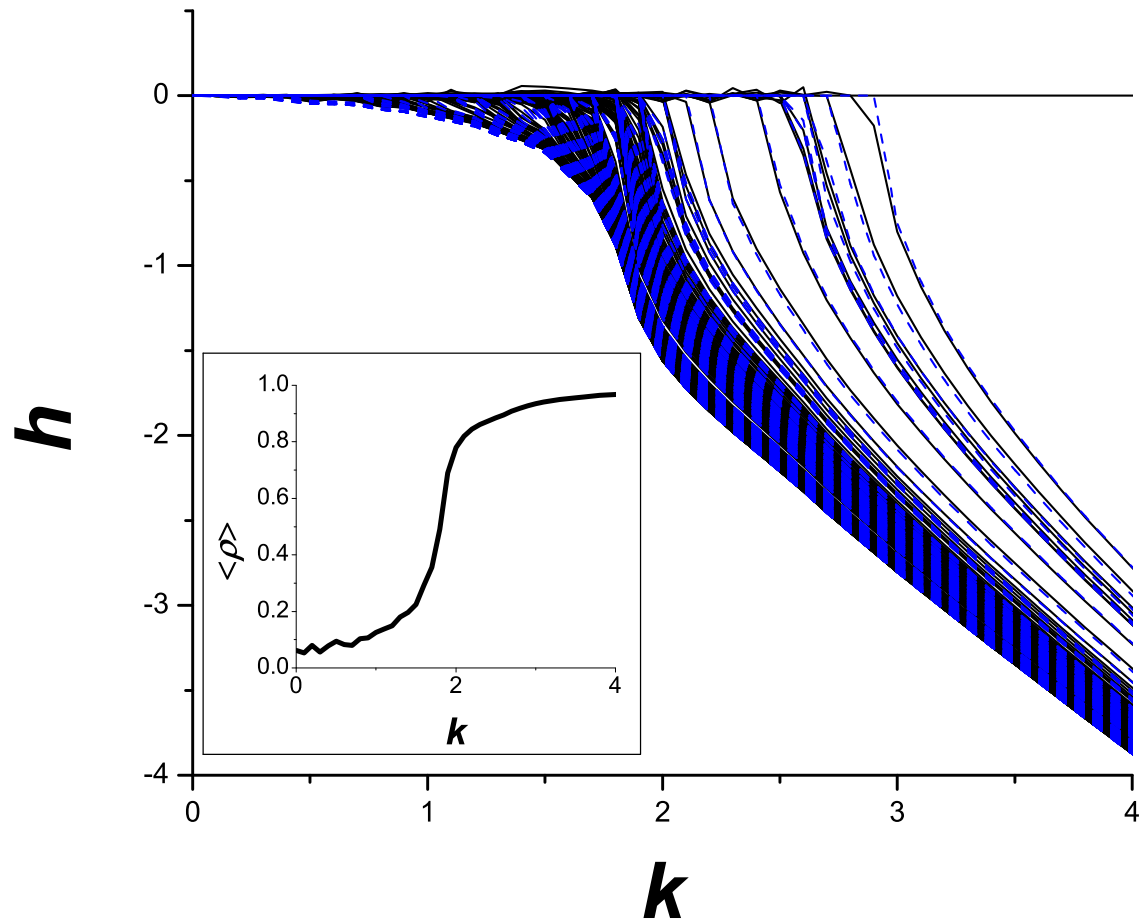
Figure 3.10: The Lyapunov spectrum for a system of $N = 200$ oscillators with natural frequencies sampled randomly from a Gaussian distribution with width $\sigma = 1$ plotted vs. coupling strength k. Black solid: the high dimensional spectrum based on the evolution of Eq. (3.1). Blue dashed: the high dimensional spectrum as predicted using the single oscillator hypothesis Eq. (3.19). Inset: Long-time average values of ρ as calculated using Eq. (3.3), plotted vs. k.

case as for the Lorentzian, Eq. (3.2), predicting the critical values of k below which h_j is near zero, the asymptotic behavior for $k\rho >> |\omega_j - \bar{\omega}|$ (where $\bar{\omega}$ is the center of the Gaussian distribution) and the intermediate values $h_j(k)$.

3.6   Conclusion

We summarize our conclusions as follows:

(i) For large N and $k > k_c$, Lyapunov exponents with appreciably negative values can be well approximated as resulting from specific individual "locked oscillators" (*i.e.*, oscillators with $|\omega_j| < k\rho$) that are forced by the mean field. The complementary nonlocked oscillators contribute a spectral component of Lyapunov exponents with values near zero, some of which are slightly negative and some slightly positive (corresponding to chaotic dynamics). These latter oscillators are smaller in number for larger k/k_c, and we show how the number of positive exponents scales with N and k.

(ii) We believe that our finding in (i) (that many of the Lyapunov exponents in the spectrum can be well described by examination of the perturbation dynamics of individual oscillators forced by the mean field) should have general applicability to many large systems of heterogeneous dynamical units that are coupled by a mean field.

(iii) Chaos of the finite N system as characterized by the largest Lyapunov exponent h_1 has been found to be approximately independent of the system size N. This finding contrasts with the N^{-1} scaling of h_1 found in Refs. [44, 45] which

investigate somewhat different situations. Thus it appears that the scaling of h_1 with N can be different under different circumstances, and that universality in the saling of h_1 with N is unlikely.

Chapter 4: The Stability of Adaptive Synchronization

of Chaotic Systems

4.1 Overview

We consider an adaptive scheme for maintaining the synchronized state in a network of identical coupled chaotic systems in the presence of *a priori* unknown slow temporal drift in the couplings. Stability of this scheme is addressed through an extension of the master stability function technique to include adaptation. We observe that noise and/or slight nonidenticality between the coupled systems can be responsible for the occurrence of intermittent bursts of large desynchronization events (bubbling). Moreover, our numerical computations show that, for our adaptive synchronization scheme, the parameter space region corresponding to bubbling can be rather substantial. This observation becomes important to experimental realizations of adaptive synchronization, in which small mismatches in the parameters and noise cannot be avoided. We also find that, for our coupled systems with adaptation, bubbling can be caused by a slow drift in the coupling strength.

4.2 Introduction

It has been shown [37, 38, 51] that, in spite of their random-like behavior, the states $x_i(t)$ ($i = 1, 2, ..., N$) of a collection of N interacting chaotic systems that are identical can synchronize (i.e., be attracted toward a common chaotic evolution, $x_1(t) = x_2(t) = ... = x_N(t)$) provided that they are properly coupled. This phenomenon has been the basis for proposals for secure communication [52–54], system identification [55–58], data assimilation [59, 60], sensors [61], information encoding and transmission [62, 63], multiplexing [64], combatting channel distortion [65], etc. In all of these applications it is typically assumed that one has accurate knowledge of the interaction between the systems, allowing one to choose the appropriate coupling protocol at each node (here we use the network terminology, referring to the N chaotic systems as N nodes of a connected network whose links (i, j) correspond to the input that node i receives from node j). In a recent paper [66], an adaptive strategy was proposed for maintaining synchronization between identical coupled chaotic dynamical systems in the presence of *a priori* unknown, slowly time varying coupling strengths (e.g., as might arise from temporal drift of environmental parameters). This strategy was successfully tested on computer simulated networks of many coupled dynamical systems in which, at each time, every node receives only one aggregate signal representing the superposition of signals transmitted to it from the other network nodes. In addition, the strategy has also been successfully implemented in an experiment on coupled optoelectronic feedback loops [67]. Furthermore, a more generalized adaptive strategy, suitable for sensor applications, has

also been proposed [61].

In past works, various other schemes for adaptive synchronization of chaos have also been proposed [68–77]. So far, in all these studies, when the question of stability of the considered adaptive schemes has been studied, the question has been addressed using the Lyapunov function method (see e.g., [70, 71, 73, 75]), which provides a sufficient but not necessary condition for stability. While this technique has the advantage that it can sometimes yield global stability conditions, it also has the disadvantages that its applicability is limited to special cases, and its implementation, when possible, requires nontrivial system specific analysis. In this chapter, we address the stability of adaptive synchronization for the example of the scheme discussed in Ref. [66]. In particular, our analysis will extend the previously developed stability analysis of chaos synchronization by the master stability function technique [37, 38] to include adaptation. We will observe that the range in which the network eigenvalues are associated with stability, is dependent on the choice of the parameters of the adaptive strategy. The type of analysis we present, while for a specific illustrative adaptive scheme, can be readily applied to other adaptive schemes (e.g., those in [76, 77]).

As compared to the Lyapunov technique, master stability techniques are much more generally applicable but they provide conditions for local, rather than global stability. We also note that, within that context, the master stability technique allows one to distinguish between stability of typical chaotic orbits and stability of atypical orbits within the synchronizing chaotic attractor (i.e., stability to 'bubbling' [6, 78–80, 82, 83]; see Secs. 4.4 and 4.5).

In Sec. 4.3 we review the adaptive synchronization strategy formulation of Ref. [66], which applies to a network of chaotic systems with unknown temporal drifts of the couplings. In Sec. 4.4, we present a master stability function approach to study linear stability of the synchronized solution in the presence of adaptation; we also consider a generalized formulation of our adaptive strategy and study its stability. Numerical simulations are finally presented in Sec. 4.5. Our work in Sec. 4.5 highlights the important effect of bubbling in the dynamics.

4.3 Adaptive strategy formulation

As our example of the application of the master stability technique to an adaptive scheme, we consider the particular scheme presented in Ref. [66]. To provide background, in this section we present a brief exposition of a formulation similar to that in Ref. [66], as motivated by the situation where the couplings are unknown and drift with time. We consider a situation where the dynamics at each of the network nodes is described by,

$$\dot{x}_i(t) = F(x_i(t)) + \gamma\Gamma[\sigma_i(t)r_i(t) - H(x_i(t))], \qquad i = 1, ..., N, \qquad (4.1)$$

where, x_i is the m-dimensional state of system $i = 1, ..., N$; $F(x)$ determines the dynamics of an uncoupled ($\gamma \to 0$) system (hereafter assumed chaotic), $F : R^m \to R^m$; $H(x)$ is a scalar output function, $H : R^m \to R$. We take Γ to be a constant m-vector, $\Gamma = [\Gamma_1, \Gamma_2, ..., \Gamma_m]^T$, with $\sum_i \Gamma_i^2 = 1$, and the scalar γ is a constant characterizing the strength of the coupling. The scalar signal each node i receives

from the other nodes in the network is,

$$r_i(t) = \sum_j A_{ij}(t) H(x_j(t)). \tag{4.2}$$

The quantity $A_{ij}(t)$ is an adjacency matrix whose values specify the strengths of the couplings from node j to node i. We note that if

$$\sigma_i(t) = [\sum_j A_{ij}]^{-1} \tag{4.3}$$

then Eq. (4.1) admits a synchronized solution,

$$x_1(t) = x_2(t) = ... = x_N(t) = x_s(t), \tag{4.4}$$

where $x_s(t)$ satisfies

$$\dot{x}_s(t) = F(x_s(t)), \tag{4.5}$$

which corresponds to the dynamics of an isolated system. We regard the $A_{ij}(t)$ as unknown at each node i, while the only external information available at node i is its received signal (4.2). The goal of the adaptive strategy is to adjust $\sigma_i(t)$ so as to maintain synchronism in the presence of slow, *a priori* unknown time variations of the quantities $A_{ij}(t)$. That is, we wish to maintain approximate satisfaction of Eq. (4.3). For this purpose, as discussed in Ref. [66], our scheme can be extended to the case where the output function is ℓ-dimensional, $H : R^m \to R^\ell$, where $\ell < m$ and Γ is an $\ell \times m$ dimensional matrix. For simplicity we consider $\ell = 1$. We assume that each node independently implements an adaptive strategy. At each system node i, we define the exponentially weighted synchronization error $\psi_i = \langle (\sigma_i r_i - H(x_i))^2 \rangle_\nu$, where

$$\langle G(t) \rangle_\nu = \int^t G(t') e^{-\nu(t'-t)} dt', \tag{4.6}$$

and we evolve $\sigma_i(t)$ so as to minimize this error (a slightly more general approach is taken in [66]). We then set $\partial \psi_i / \partial \sigma_i$ equal to zero to obtain

$$\sigma_i(t) = \frac{\langle H(x_i(t)) r_i(t) \rangle_\nu}{\langle r_i(t)^2 \rangle_\nu} = \frac{p_i(t)}{q_i(t)}. \tag{4.7}$$

By virtue of $d \langle G(t) \rangle_\nu / dt = -\nu \langle G(t) \rangle_\nu + G(t)$, we obtain the numerator and the denominator on the right-hand side of Eq. (4.7) by solving the differential equations,

$$\dot{p}_i(t) = -\nu p_i(t) + r_i(t) H(x_i(t)), \tag{4.8a}$$

$$\dot{q}_i(t) = -\nu q_i(t) + r_i(t)^2. \tag{4.8b}$$

Since we imagine the dynamics of $A_{ij}(t)$ occur on a timescale which is slow compared to the other dynamics in the network, we can approximate $A_{ij}(t)$ as constant A_{ij}. This essentially assumes that we are dealing with perturbations from synchronization whose growth rates (in the case of unstable synchronization) or damping rates (in the case of stable synchronization) have magnitudes that substantially exceed $|A_{ij}^{-1}(t) dA_{ij}/dt|$. Under this assumption, we note that Eqs. (4.1), (4.7), and (4.8) admit a synchronized solution, given by Eqs. (4.4), (4.5), and

$$\dot{p}_i^s = -\nu p_i^s + (\sum_j A_{ij}) H(x^s)^2, \quad i = 1, ..., N, \tag{4.9a}$$

$$\dot{q}_i^s = -\nu q_i^s + (\sum_j A_{ij})^2 H(x^s)^2, \quad i = 1, ..., N. \tag{4.9b}$$

To simplify the notation, in what follows, we take $DF^s(t) = DF(x^s(t))$, $H^s(t) = H(x^s(t))$, and $DH^s(t) = DH(x^s(t))$; e.g., we can now write,

$$p_i^s = k_i \langle (H^s)^2 \rangle_\nu, \tag{4.10}$$
$$q_i^s = k_i^2 \langle (H^s)^2 \rangle_\nu,$$

where $k_i = (\sum_j A_{ij})$. If the synchronization scheme is locally stable, we expect that the synchronized solution Eqs. (4.4), (4.5) and (4.9) will be maintained under slow time evolution of the couplings $A_{ij}(t)$.

4.4 Stability analysis

4.4.1 Linearization and master stability function

Our goal is to study the stability of the reference solution Eqs. (4.4), (4.5) and (4.9). By linearizing Eqs. (4.1) and (4.8) about Eqs. (4.5), and (4.9), we obtain,

$$
\delta\dot{x}_i = DF^s\delta x_i + \gamma\Gamma\left\{DH^s\left[k_i^{-1}\sum_j A_{ij}\delta x_j - \delta x_i\right] + \frac{H^s}{k_i^2\left\langle(H^s)^2\right\rangle_\nu}\epsilon_i\right\}, \quad i = 1, ..., N,
$$

(4.11a)

$$
\dot{\epsilon}_i = -\nu\epsilon_i - H^sDH^sk_i\left[\sum_j A_{ij}\delta x_j - k_i\delta x_i\right], \quad i = 1, ..., N,
$$

(4.11b)

where we have introduced the new variable $\epsilon_i(t) = k_i\delta p_i(t) - \delta q_i(t)$.

Equations (4.11) constitute a system of $(m+1)N$ coupled equations. In order to simplify the analysis, we seek to decouple this system into N independent systems, each of dimension $(m + 1)$. For this purpose we seek a solution where δx_i is in the form $\delta x_i = c_i\bar{x}(t)$, where c_i is a time independent scalar that depends on i and $\bar{x}(t)$ is a m-vector that depends on time but not on i. Substituting in Eqs. (4.11a),(4.11b),

we obtain,

$$\dot{\bar{x}} = DF^s\bar{x} + \gamma\Gamma\left[\frac{\sum_j A_{ij}c_j}{k_ic_i} - 1\right]DH^s\bar{x} + \frac{\gamma\Gamma H^s}{c_ik_i^2\langle(H^s)^2\rangle_\nu}\epsilon_i, \quad i = 1, ..., N, \quad (4.12a)$$

$$\dot{\epsilon}_i = -\nu\epsilon_i - k_i\left[\sum_j A_{ij}c_j - k_ic_i\right]H^sDH^s\bar{x}, \quad i = 1, ..., N. \quad (4.12b)$$

To make Eqs. (4.12) independent of i, we consider $\beta(t) = \epsilon_i(t)/[c_ik_i^2(\alpha - 1)]$ and

$\sum_j A_{ij}c_j = \alpha k_ic_i$, where α is a quantity independent of i. Namely, the possible

values of α are the eigenvalues, $A'\vec{c} = \alpha\vec{c}$, corresponding to linearly independent

eigenvectors $\vec{c} = [c_1, c_2, ..., c_N]^T$, where $A' = \{A'_{ij}\} = \{k_i^{-1}A_{ij}\}$. This gives,

$$\dot{\bar{x}} = DF^s\bar{x} - \gamma(1 - \alpha)\left[\Gamma DH^s\bar{x} + \Gamma\frac{H^s\beta}{\langle(H^s)^2\rangle_\nu}\right], \quad (4.13a)$$

$$\dot{\beta} = -\nu\beta - H^sDH^s\bar{x}, \quad (4.13b)$$

which is independent of i, but depends on the eigenvalue α. Considering the typ-

ical case where there are N distinct eigenvalues of the $N \times N$ matrix A', we see

that Eqs. (4.12) constitute N decoupled linear ordinary differential equations for

the synchronization perturbation variables $\bar{x}$ and β. All the rows of A' sum to 1.

Therefore A' has at least one eigenvalue $\alpha = 1$, corresponding to the eigenvector

$c_1 = c_2 = ... = c_N = 1$. Furthermore, since $A'_{ij} \geq 0$ for all (i, j), we have by the

Perron-Frobenius theorem that $\alpha \leq 1$, and thus $(1 - \alpha) \geq 0$. For $\alpha = 1$, Eq. (4.13a)

becomes,

$$\dot{\bar{x}} = DF^s\bar{x}. \quad (4.14)$$

This equation reflects the chaos of the reference synchronized state (Eq. (4.5)) and

(because all the c_i are equal) is associated with perturbations which are tangent to

the synchronization manifold and are therefore irrelevant in determining synchro-

nization stability. Stability of the synchronized state thus demands that Eqs. (4.12) yield exponential decay of $\bar{x}$ and β for all the $(N-1)$ eigenvalues α, excluding this $\alpha = 1$ eigenvalue.

It thus becomes possible to introduce a master stability function [37,38], $M(\xi)$, that associates the maximum Lyapunov exponent of system (4.13) with $\xi = \gamma(1-\alpha)$. In so doing, one decouples the effects of the network topology (reflected in the eigenvalues α and hence the relevant values of $\xi = \gamma(1-\alpha)$) from the choices of F, H, ν. In general an eigenvalue, and hence also ξ, can be complex. For simplicity, in our discussion and numerical examples to follow, we assume that the eigenvalues are real (which is for instance the case when the adjacency matrix is symmetric). For any given value of γ stability demands that $M(\xi) < 0$ for all those values of $\xi = \gamma(1-\alpha)$ corresponding to the eigenvalues $\alpha \neq 1$.

Following Refs. [84–87], we now introduce the following definition of *synchronizability*. Let us assume that the master stability function $M(\xi)$ is negative in a bounded interval of values of ξ, say $[\xi^-, \xi^+]$. Then, in order for the network to synchronize, two conditions need to be satisfied, (i) $\xi^- < \gamma(1 - \alpha_{min})$, and (ii) $\xi^+ > \gamma(1 - \alpha_{max})$, where α_{min} (α_{max}) is the smallest (largest) network eigenvalue over all the eigenvalues $\alpha \neq 1$. The network synchronizability is defined as the width of the range of values of γ, for which $M(\xi) < 0$. Assuming that α_{min} and α_{max} are assigned (e.g., the network topology is given), then the network synchronizability increases with the ratio ξ^+/ξ^-. In what follows, we will compare different adaptive strategies in terms of their effects on the synchronizability ratio ξ^+/ξ^-.

In our analysis above, since we divide by k_i, we have implicitly assumed that

all the $k_i \neq 0$, i.e., that every node has an input. There is, however, a case of interest where this is not so, and this case requires separate consideration. In particular, say there is one and only one special node (which we refer to as the maestro or sender) that has no inputs, but sends its output to other nodes (which interact with each other), and we give this special node the label $i = N$. Since node N receives no inputs, we do not include adaption on this node, and we replace Eq.(1) for $i = N$ by $\dot{x}_N(t) = F(x_N(t))$. In addition, when investigating the stability of the synchronized state, it suffices to set $\delta x_N(t) = 0$ (i.e., not to perturb the maestro). Following the steps of our previous stability analysis, we again obtain Eqs. (4.12) and (4.13), but with important differences. Namely, Eqs. (4.12) now apply for $i = 1, ..., N - 1$, the values of α in Eqs. (4.13) are now the eigenvalues of the $(N - 1) \times (N - 1)$ matrix $\{A'_{ij}\} = \{k_i^{-1} A_{ij}\}$ for $i, j = 1, 2, ..., (N - 1)$; i.e., only the interactions between the nodes $i, j \leq (N - 1)$ are included in this matrix. Note that k_i is still given by $\sum_{j=1}^{N} A_{ij}$, still including the input A_{iN} from the maestro node. Also since $\delta x_N = 0$, all of the eigenvalues represent transverse perturbations and are therefore relevant to stability. (This is in contrast to the case without a maestro in which we had to exclude an eigenvalue, i.e., $\alpha = 1$ corresponding to $c_1 = c_2 = ... = c_N = 1$. For a similar discussion for the case of the standard master stability problem with no adaptation, see [88].) The simplest case of this type (used in some of our subsequent numerical experiments) is the case $N = 2$, where there is one receiver node ($i = 1$) and one sender/maestro node ($i = 2$). Since there is only one receiver node whose only input is received by the sender, A reduces to the scalar $A = 0$ and $\alpha = 0$, yielding $\xi \equiv \gamma$.

As stated above, $x_s(t)$ in (4.4) is an orbit of the uncoupled system (4.4). In general, two types of orbits $x_s(t)$ are of interest: (i) a typical chaotic orbit on the relevant chaotic attractor of (4.4), and (ii) the orbit that is ergodic on the maximally synchronization-unstable invariant subset embedded within the relevant chaotic attractor of (4.4). Here, by 'relevant chaotic attractor' we mean that, if the system (4.4) has more than one attractor, then we restrict attention to that attractor on which synchronized motion is of interest. Also, in (i), by the word 'typical', we mean orbits of (4.4) that ergodically generate the measure that applies for Lebesgue almost every initial condition in the attractor's basin of attraction. In this sense, the orbit in (ii) is not typical. In general the criterion for stability as assessed by (ii) is more restrictive than that assessed by (i). Conditions in which the synchronized dynamics is stable according to (i), but unstable according to (ii), are referred to as the 'bubbling' regime [6, 78–80, 82]. In previous work on synchronization of chaos [6, 78–80, 82, 83], it has been shown that, when the system is in the bubbling regime, small noise and/or small 'mismatch' between the coupled systems can lead to rare, intermittent, large deviations from synchronism, called 'desynchronization bursts' [81]. By small system mismatch we mean that, for each node i, the functions F in (4.1) are actually different, $F \rightarrow F_i$, but that these differences are small (i.e., $|F_i(x) - F(x)|$ is small, where $F(x)$ now denotes a reference uncoupled system dynamics; e.g., F_i averaged over i). With reference to our adaptive synchronization problem (4.1), we shall see that, in addition to small noise and small mismatch in F, bursting can also be induced by slow drift in the unknown couplings $A_{ij}(t)$. From the practical, numerical perspective, the complete and rigorous application

81

of the stability criterion (ii) is impossible, since there will typically be an infinite number of distinct invariant sets embedded in a chaotic attractor, and, to truly be sure of stability, each of these must be found and numerically tested. In practice, therefore, as done previously by others, we will evaluate stability for all the unstable periodic orbits embedded in the attractor up to some specified period. This will give a necessary condition for stability according to (ii), and furthermore, it has been argued and numerically verified in Ref. [82] that stability, as assessed from a large collection of low period periodic orbits (and embedded unstable fixed points, if they exist in the relevant attractor), will extremely often yield the true delineation of the parameters of the bubbling regime, or, if not, an accurate approximation of it. Our numerical results of Sec. IV lend further support to this idea.

4.4.2   Generalized adaptive strategy

We now analyze a generalization of our adaptive strategy. Namely, we replace Eq. (4.8b) by,

$$\dot{p}_i(t) = -\nu p_i(t) + [q_i(t)/p_i(t)]H(x_i(t))^2 Q\left(\frac{p_i(t)r_i(t)}{q_i(t)H(x_i(t))}\right), \qquad (4.15)$$

where $Q(z)$ is an arbitrary function of z, normalized so that $Q(1) \equiv 1$. The key point is that at synchronism $\sigma_i r_i = H(x_i(t))$, corresponding to $p_i r_i = q_i H(x_i(t))$; and thus, since we take $Q(1) = 1$, the synchronized solution is unchanged. The stability analysis for this generalization is given in the Appendix I and results in the

following master stability equations,

$$\dot{\bar{x}} = DF^s\bar{x} - \xi\left[\Gamma DH^s\bar{x} + \Gamma\frac{H^s\beta'}{\langle(H^s)^2\rangle_\nu}\right], \tag{4.16a}$$

$$\dot{\beta}' = -\nu\beta' + (\phi - 1)\frac{(H^s)^2}{\langle(H^s)^2\rangle_\nu}\beta' + (\phi - 2)H^s DH^s\bar{x}, \tag{4.16b}$$

where $\phi = Q'(1)$, and $Q'(1)$ denotes $dQ(z)/dz$ evaluated at $z = 1$. We then intro-
duce a master stability function $M(\xi, \phi)$, that associates the maximum Lyapunov
exponent of system (4.16) with $\xi = \gamma(1 - \alpha)$ and ϕ.

Thus we expect that, when our modified adaptive scheme is stable, it will again
relax to the desired synchronous solution. The difference between the stability of the
modified scheme (Eqs. (4.13)) and the stability of the original scheme (corresponding
to Eqs. (4.16) with $\phi = 1$), is that, by allowing the freedom to choose the value
of ϕ, we can alter the stability properties of the synchronous state. We anticipate
that, by properly adjusting ϕ, we may be able to tailor the stability range to better
suit a given situation.

In the case of $\phi = 2$, Eq. (4.16b) reduces to,

$$\dot{\beta}' = \left[\frac{(H^s)^2}{\langle(H^s)^2\rangle_\nu} - \nu\right]\beta', \tag{4.17}$$

which has a Lyapunov exponent $\lambda = \lambda_0 - \nu$, where λ_0 is the time average of
$(H^s)^2/\langle(H^s)^2\rangle_\nu$, $\lambda_0 \geq 0$. For $\nu > \lambda_0$, Eq. (4.17) implies that β' decays to zero.
Thus, if we choose a large enough value of ν, stability of the synchronized state
is determined by (4.16a) with β' set equal to zero, and Eq. (4.16a) reduces to the
master stability function for the determination of the stability of the system without
adaptation [37]. Therefore, in the case of $\phi = 2$, $\nu > \lambda_0$, the stable range of γ is

independent of ν and is the same as that obtained for the case in which adaptation is not implemented ($\sigma \equiv 1$).

4.5 Numerical experiments

In our numerical experiments we consider the example of the following Rössler equation, for which, $m = 3$, $x(t) = (u(t), v(t), w(t))^T$,

$$F(x) = \begin{bmatrix} -v - w \\ u + av \\ b + (u - c)w \end{bmatrix},$$
(4.18)

with the parameters $a = b = 0.2$, and $c = 7$, and we use $H(x(t)) = u(t)$, and $\Gamma = [1, 0, 0]^T$. In Fig. 4.1 the master stability functions $M(\xi)$ calculated from Eq. (4.13) for the adaption scheme of Sec. II are plotted for three different values of ν, i.e., $\nu = 0.1, 2, 6$ (dashed, dashed/dotted, and dotted curves, respectively). In addition, for comparison, we also plot the result of $M(\xi)$ computations for the case in which no adaptation is introduced, corresponding to the reduced system $\dot{\bar{x}} = [DF^s + \gamma(\alpha - 1)\Gamma DH^s]\bar{x}$ (solid curves). The master stability function is shown in black (respectively, grey) for the cases that $x_s(t)$ is a typical chaotic orbit in the attractor (respectively, the maximally unstable periodic orbit embedded in the attractor for periodic orbits of period up to four surface of section piercings; see Appendix II for a brief account of how the unstable periodic orbits were obtained). We say that synchronization is 'high quality' stable in the range of ξ for which $M(\xi)$ for all orbits (i.e., including the periodic orbits) is negative. As can be seen,

by changing the parameter ν, the ξ-range of stability can be dramatically modified. The bubbling range is given by the values of ξ for which $M(\xi) < 0$ for a typical orbit but $M(\xi) > 0$ for the maximally unstable periodic orbit embedded in the attractor.
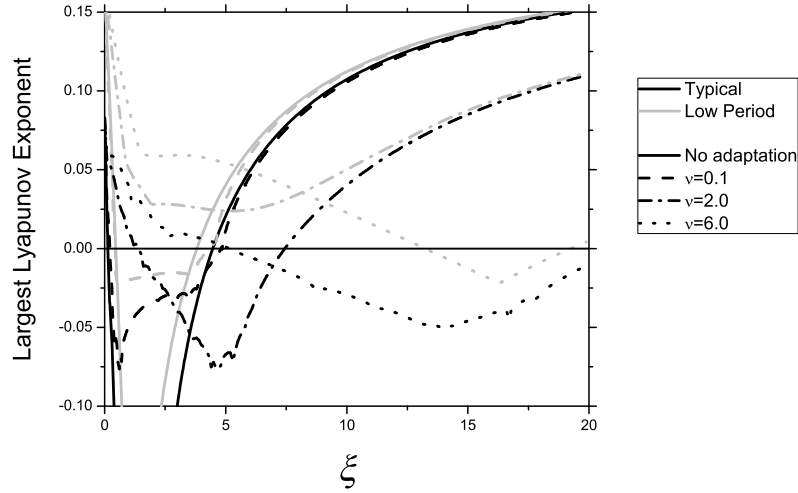
Figure 4.1: The plot shows the master stability function $M(\xi)$ versus ξ for the case in which no adaptation was introduced, corresponding to $\sigma \equiv 1$ (black continuous line) and for three different values of ν, i.e., $\nu = 0.1, 2, 6$ (dashed and dotted lines). The master stability functions obtained by choosing $x_s(t)$ to be a typical chaotic orbit in the attractor (respectively, the maximally unstable periodic orbit embedded in the attractor of period up to four) are in black (respectively, grey). $F(x)$ is the Rössler equation (4.18), $H(x(t)) = u(t)$, and $\Gamma = [1, 0, 0]^T$.

Figure 4.2 is a $\xi - \nu$ level curve plot of the values assumed by the master stability function M evaluated for $x_s(t)$ being a typical chaotic orbit. In the figure, the area of stability (corresponding to $M < 0$) is delimited by the thick 0-level contour line. From the figure, we see that the width of the range of stability increases

with ν. In Figs. 4.3(a,b) a comparison between the areas of stability is given, for the cases in which $x_s(t)$ is a typical chaotic orbit in the attractor, and for the case that $x_s(t)$ is the maximally unstable periodic orbit embedded in the attractor of period up to four. The thick solid (respectively, dashed) curves bound the area in which the master stability function $M(\xi, \nu)$ is negative for $x_s(t)$ corresponding to a typical chaotic orbit in the Rösller attractor (respectively, for $x_s(t)$ corresponding to the maximally unstable periodic orbit embedded in the attractor of period up to four). The bubbling area falls between the dashed and the continuous contour lines.

Interestingly, we see that for $1.2 \lesssim \nu \lesssim 3.2$, high-quality stability can never be achieved for any ξ, while, in contrast, stability with respect to typical chaotic orbits (i.e., with bubbling) is achievable. Let $\xi_t^+, \xi_t^-, \xi_p^+, \xi_p^-$ denote the upper $(+)$ and lower $(-)$ values of ξ at the borders of the stability regions with respect to a typical (t) chaotic orbit and with respect to unstable periodic orbits (p) in the synchronizing attractor. E.g., high-quality synchronism applies for $\xi_p^+ > \xi > \xi_p^-$ and the bubbling regime corresponds to $\xi_p^- > \xi > \xi_t^-$ or $\xi_t^+ > \xi > \xi_p^+$. In terms of these quantities, useful measures for assessing the possibility of achieving stable synchronism for a given network topology are the 'synchronizability' ratios [84–87],

$$s_t = \frac{\xi_t^+}{\xi_t^-}, \qquad s_p = \frac{\xi_p^+}{\xi_p^-}.$$ (4.19)

In what follows, where convenient, we drop the subscripts t and p with the understanding that the discussion may be taken to apply to stability based on either typical or periodic orbits. Noting that synchronism is stable for $\xi^+ > \xi > \xi^-$, and that $\xi = \gamma(1 - \alpha)$, we consider the coupling network topology-dependent ra-

tio $(1 - \alpha^-)/(1 - \alpha^+)$ where α^+ (α^-) denotes the maximum (minimum) eigenvalue of the adjacency matrix (not including the eigenvalue $\alpha = 1$ corresponding to the eigenvector $(1, 1, ..., 1)^T$). Recall that $(1 - \alpha) \geq 0$. Since $\xi^+ > \xi > \xi^-$ for stability, if

$$s > \frac{1 - \alpha^-}{1 - \alpha^+}, \tag{4.20}$$

then the system can be made stable by adjustment of the constant γ, but, if $s < (1 - \alpha^-)/(1 - \alpha^+)$, then it is impossible to choose a value of γ for which $M(\xi) < 0$ for all the relevant eigenvalues α, and stability is unachievable. Figure 4.3(c) shows plots of s_t and s_p versus ν for the same parameters as used in Figs. 4.3(a,b). Note that, for these computations, the values of s without adaption (i.e., $s_t = 23.5$ and $s_p = 10.5$) always exceed the corresponding values with adaption. We have also found this to be true for the generalized adaptive scheme of Sec. III B (which includes the additional adaption parameter ϕ). However, we do not know whether this is general, or is limited to our particular example (Eq. (4.18) with $H(x) = u$, and our choices of the parameters a,b, and c).

To test our linear results in Fig. 4.3, we have also performed fully nonlinear numerical simulations for a simple network consisting of a sender system (labeled 1) connected to a receiver (labeled 2). In this case Eq. (1) becomes

$$\dot{x}_1(t) = F(x_1(t)), \tag{4.21a}$$

$$\dot{x}_2(t) = F(x_2(t)) + \gamma \Gamma [\sigma(t) A(t) H(x_2(t)) - H(x_1(t))], \tag{4.21b}$$

and $A(t)$ is a scalar. Each data point shown in Figs. 4.3(a,b) corresponds to a run, where the sender was given a random initial condition and random values for ν

87
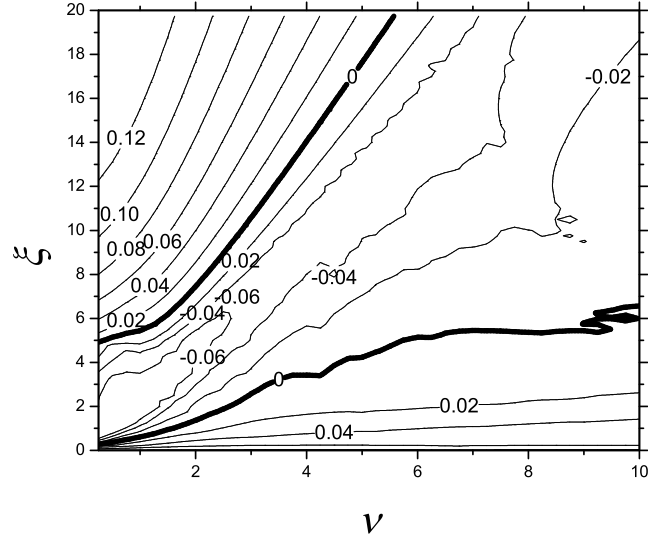
Figure 4.2: The figure is a level curve plot in ξ-ν space of the values assumed by the master stability function M, evaluated for $x_s(t)$ being a typical chaotic orbit. The area of stability (corresponding to $M < 0$) is delimited by the thick 0-level contour line. $F(x)$ is the Rössler equation (4.18), $H(x(t)) = u(t)$, and $\Gamma = [1, 0, 0]^T$.

and ξ were chosen in the plotted range. After waiting sufficient time to ensure that the sender state is essentially on the attractor, the u-variable of the receiver state was initialized by a displacement of 10^{-8} from the u-variable of the sender state. A step-size of 10^{-4} was used for a run time of 10^5 time units, over which we recorded the normalized synchronization error,

$$E(t) = \frac{|u_1(t) - u_2(t)|}{\langle (u_s - \langle u_s \rangle)^2 \rangle^{1/2}}, \tag{4.22}$$

where $\langle ... \rangle$ indicates a time average and the subscript s denotes evolution on the synchronous state (i.e., using dynamics from Eq. (4.4)). If, in that time span, E never converged to 0 and, at some point, exceeded 0.1, the run was considered to be

unstable (corresponding to an $\times$ in the figure). If E converged to 0, a 1% mismatch

in the Rössler parameter a was introduced to the receiver, and the run of duration 10^5

time units was repeated with an initial separation of 0. If, at any time during the run,

E ever exceeded 0.1, the run was considered to be bubbling (corresponding to a green

circle in the figure), otherwise the run was considered to be stable (corresponding

to a red triangle in the figure). We see that the master stability computations of

the high-quality stable, bubbling, and unstable regions (the solid and dashed lines)

correspond well with these results. We also did a sampling of points up to period

5 and did not find that this altered our results. From Fig. 4.3(a), we observe the

presence of a few green circles (i.e, bubbling) within the high-quality synchronization

area, delimited by the dashed line. In reference to this observation, we note that (i)

for the case in which a small parameter mismatch is present, the synchronization

error is expected to vary smoothly with parameter variation, and there is no sharp

transition from the stable to the bubbling regime; and (ii) our computations show

that close to the dashed line, the master stability function associated with the most

unstable invariant set embedded in the attractor is rather small. Facts (i) and (ii)

explain our difficulty in using our nonlinear computations to clearly separate the

bubbling from the stable regions about the dashed line in Fig. 4.3(a). An important

point concerning Figs. 4.3(a,b) is that the area associated with bubbling in Fig.

4.3(a) is rather substantial. This observation would become particularly important

in experimental realizations of adaptive synchronization, since small mismatches in

the parameters and noise cannot be avoided in experiments.

Figure 4.4 shows a sample plot of the normalized synchronization error $E(t)$,

versus t. We implemented our adaptive strategy with values of $\nu = 2.5$ and $\gamma = 5$, corresponding to the bubbling regime (see Fig. 4.3), $A(t) = 1$, and the receiver has 0.1% mismatch in the parameter a. The two insets are zooms showing phase-space projections in the plane (u_2, v_2), over two different time intervals. Inset (b) corresponds to a range of time between bursts $(E(t) < 5 \times 10^{-2})$ and shows that during this time the orbit is essentially that of a typical chaotic orbit. Inset (a) shows the orbit trajectory for a range of time during which a burst is growing. It is seen from inset (b) that during the time range of the growing burst the orbit closely follows a period 4 orbit embedded in the attractor. The burst is evidently caused by the instability of this period 4 orbit to perturbations that are transverse to the synchronization manifold.

We have also performed numerical master stability computations for our generalized adaptive strategy, presented in Sec. IIIb. This is shown in Fig. 4.5, where the $\xi^+(\phi)$ and $\xi^-(\phi)$ curves, corresponding respectively to the largest (smallest) values of ξ for which $M(\xi, \phi) > 0$ ($M(\xi, \phi) < 0$), are plotted versus ϕ for three different values of $\nu = [0.1, 2.0, 6.0]$ for typical chaotic orbits. For small ν (e.g., $\nu = 0.1$ in the figure), the range of stability $[\xi^-, \xi^+]$ is almost independent of ϕ, while for larger values of ν the choice of ϕ can significantly affect the ξ-range of stability. As expected, at $\phi = 2$, $\xi^+(\phi)$ and $\xi^-(\phi)$ are independent of ν.

Finally, we investigated whether, for our coupled systems with adaptation, bubbling can be caused by a slow drift in the coupling strength. For this purpose

we now take the parameter $A(t)$ in Eq. (4.21) to have a slow time drift,

$$A(t) = 1 + 0.2\sin(2\pi \times 10^{-3}t). \tag{4.23}$$

We implemented our adaptive strategy with values of $\nu = 1$ and $\gamma = 2$, corresponding to the bubbling regime (see Fig. 4.3). For most of the time there is good synchronization between the sender and the receiver, but we also observed the intermittent occurrence of short, intense desynchronization bursts. Figure 6 shows the synchronization error $E(t)$ versus t. Note that in the absence of parameter drift (A constant), the synchronization error would eventually become zero. This simulation shows that, similarly to the previously reported burst-inducing effect of small parameter mismatch or noise, drift also promotes the continuous intermittent occurrence of bursting.

4.6   Conclusion

This chapter is concerned with the study of stability of adaptive synchronization of chaos in coupled complex networks (e.g., sensor networks). As an example addressing this issue, we consider a recently proposed adaptive scheme for maintaining synchronization in the presence of *a priori* unknown slow temporal drift in the couplings [66]. In contrast with previous approaches (e.g., [70, 71, 73, 75]), based on system specific use of the Lyapunov function technique, we present a master stability analysis which predicts the exact ranges of stability for the synchronized state. We observe that the stable range of synchronism can be sensitively dependent on the adaption parameters. Moreover, we are able to predict the onset of bubbling, which

occurs when the synchronized state is stable for typical chaotic orbits but is unstable for certain unstable periodic orbits within the synchronized chaotic attractor. We define stability to be *high quality* when the synchronized state is stable with respect to all the orbits embedded in the attractor and numerically find the regions of 'high quality stability' for a given system of interest. We also found that, for our coupled systems with adaptation, bubbling can be caused by a slow drift in the coupling strength, in addition to small noise and small mismatch in F. We emphasize that, since parameter mismatch, noise and drift are ubiquitous in experimental situations, and since (e.g., Fig. 4.3(a)) bubbling can occupy substantial regions of parameter space, consideration of bubbling can be expected to be essential for determining the practical feasibility of chaos synchronization applications.
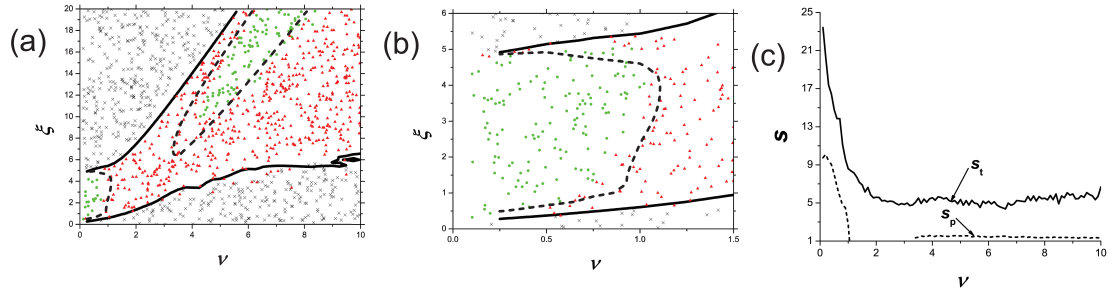
Figure 4.3: In plot (a), thick solid curves (thick dashed curves) bound the area in which the master stability function $M(\xi, \nu)$ is negative for $x_s(t)$ corresponding to a typical chaotic orbit in the Rössler attractor (for $x_s(t)$ corresponding to the maximally unstable periodic orbit embedded in the attractor of period up to four), $F(x)$ is the Rössler equation (4.18), $H(x(t)) = u(t)$, and $\Gamma = [1, 0, 0]^T$. Each data point shown in the figure is the result of a simulation involving a sender (maestro) system connected to a receiver, where the receiver state was initialized by a displacement of 10^{-8} from the sender state. A step-size of 10^{-4} was used for a run time of 10^5 time units. If, in that time span, the synchronization error E never converged to 0 and, at some point, exceeded 0.1, the run was considered to be unstable ($\times$ symbols). If E converged to 0, a 1% mismatch in the Rössler parameter a was introduced to the receiver, and the run was repeated with an initial separation of 0. Then, if E ever exceeded 0.1, the run was considered to be bubbling (green circles), otherwise the run was considered to be stable (red triangles). Plot (b) is a blow up of the lower left corner of plot (a). Plot (c) shows the synchronizability ratios s_t (solid curve) and s_p (dashed curve) versus ν. The missing data for the dashed curve are a result of the low period orbits not having a range of stability for those values of ν. The synchronizability ratios for the nonadaptive case were found to be equal to those in the limit $\nu \to 0$.

93
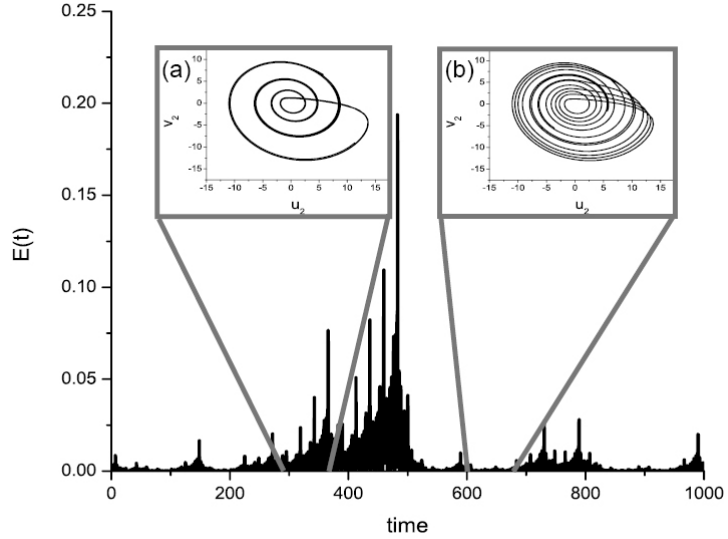
Figure 4.4: The figure shows the synchronization error $E(t)$ versus t for a simple network consisting of a sender connected to a receiver (Eqs. (4.21)), $F(x)$ is the Rössler equation (4.18), $H(x(t)) = u(t)$, $\Gamma = [1, 0, 0]^T$, $\gamma = 5$, $\nu = 2.5$, $A(t) = 1$, $dt = 10^{-3}$. The receiver has a 0.1% mismatch in the parameter a. The two insets are zooms showing phase-space projections in the plane (u_2, v_2), over two different time intervals. Inset (b) corresponds to a typical chaotic orbit for which the synchronization error is small, i.e., $E(t) < 5 \times 10^{-2}$, while inset (a) corresponds to an unstable period 4 periodic orbit embedded in the attractor, for which $E(t)$ is eventually large (i.e., a burst occurs).
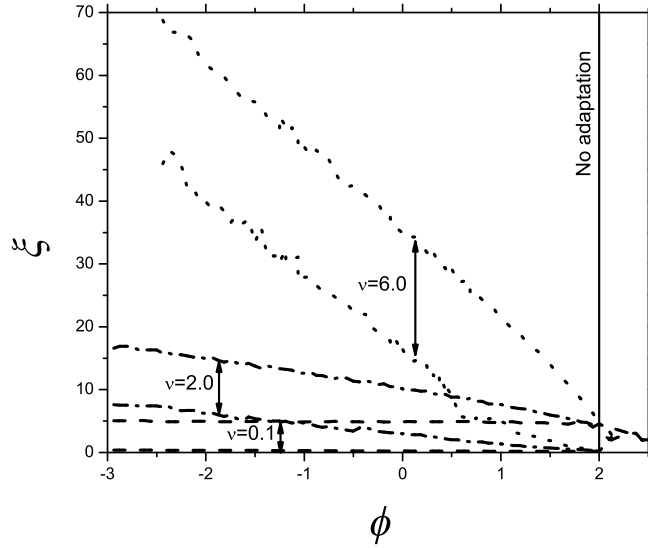
Figure 4.5: The plot shows the area in the parameter space (ϕ, ξ) in which $M(\xi, \phi)$ obtained from (4.16) is negative, for three different values of $\nu = [0.1, 2.0, 6.0]$; $F(x)$ is the Rössler equation (4.18), $H(x(t)) = u(t)$, and $\Gamma = [1, 0, 0]^T$. The stability areas are upper and lower bounded by the ξ^+ curve and the ξ^- curve, plotted as function of ϕ. As the figure shows, at $\phi = 2$, ξ^+ and ξ^- are independent of ν, corresponding to the case of no-adaptation.
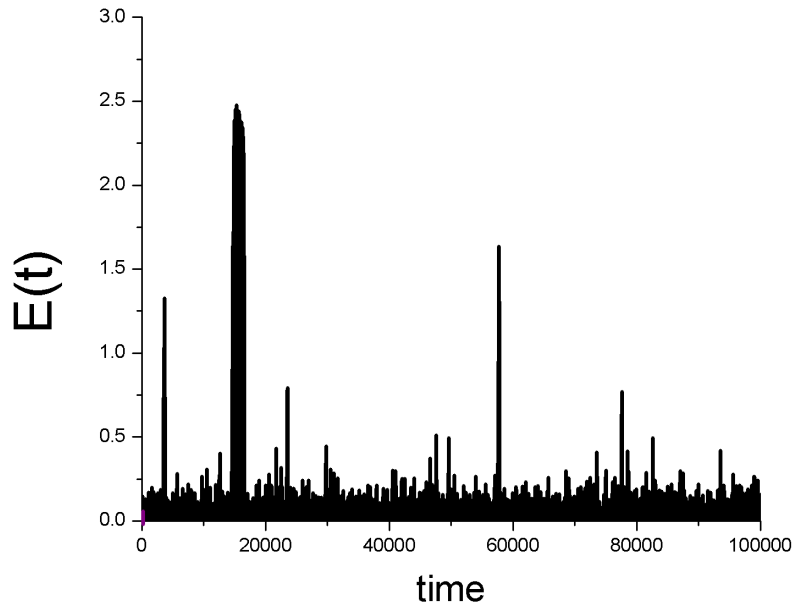
Figure 4.6: The figure is a plot of the synchronization error $E(t)$ (defined in Eq. (4.22)) versus t for a simple network consisting of a sender connected to a receiver (Eqs. (4.21)), $F(x)$ is the Rössler equation (4.18), $H(x(t)) = u(t)$, $\Gamma = [1, 0, 0]^T$, $\nu = 1$, $\gamma = 2$, $A(t) = 1 + 0.2 \sin(2\pi \times 10^{-3}t)$, $dt = 10^{-3}$. As can be seen, the dynamics of $E(t)$ exhibits intermittent bursting.

Chapter A: Stability of the generalized adaptive strategy

We note that the function $Q([p_i(t)r_i(t)]/[q_i(t)H(x_i(t))])$ in Eq. (4.15), when evaluated about (4.9), is equal to one. Then, by linearizing Eqs. (4.1), (4.8a), and (4.15) about (4.9), we obtain,

$$\delta\dot{x}_i = DF^s\delta x_i + \gamma\Gamma\left\{DH^s\left[k_i^{-1}\sum_j A_{ij}\delta x_j - \delta x_i\right] + \frac{H^s}{k_i^2\langle(H^s)^2\rangle_\nu}\epsilon_i\right\}, \quad i = 1, ..., N,$$

(A.1a)

$$\dot{\epsilon}_i = -\nu\epsilon_i + (\phi - 1)\frac{(H^s)^2}{\langle(H^s)^2\rangle_\nu}\epsilon_i + (\phi - 2)H^sDH^s\left[k_i\sum_j A_{ij}\delta x_j - k_i^2\delta x_i\right], \quad i = 1, ..., N.$$

(A.1b)

As in our derivation of Eqs. (4.13), we again set $\delta x_i = c_i\bar{x}(t)$, where c_i is a constant scalar that depends on i and $\bar{x}(t)$ is a vector that depends on time but not on i. Equations (A.1), then become

$$\dot{\bar{x}} = DF^s\bar{x} + \gamma\Gamma\left[\frac{\sum_j A_{ij}c_j}{k_ic_i} - 1\right]DH^s\bar{x} + \frac{\gamma\Gamma H^s}{c_ik_i^2\langle(H^s)^2\rangle_\nu}\epsilon_i, \quad i = 1, ..., N,$$

(A.2a)

$$\dot{\epsilon}_i = -\nu\epsilon_i + (\phi - 1)\frac{(H^s)^2}{\langle(H^s)^2\rangle_\nu}\epsilon_i + (\phi - 2)H^sDH^s\left[k_i\sum_j A_{ij}c_j - k_i^2c_i\right]\bar{x}, \quad i = 1, ..., N.$$

(A.2b)

To make Eqs. (A.2) independent of i, we again consider $\beta'(t) = \epsilon_i(t)/[c_i k_i(\alpha - 1)]$ and take α to be the eigenvalues of $\mathbf{A}' = \{A'_{ij}\} = \{k_i^{-1} A_{ij}\}$, resulting in Eqs. (4.16).

Chapter B: Determination of unstable periodic orbits

To account for the phenomenon of bubbling, it is necessary to look not just at typical (that is, chaotic) orbits of the uncoupled oscillator, but the periodic orbits embedded in the chaotic attractor as well. As there are a (countably) infinite number of such orbits, it is impossible to account for them all. However, as shown by Hunt and Ott, the optimal periodic orbits of maximal transverse instability tend to be those of low period [82]. Thus, for our analysis, it was found to be sufficient to consider only those orbits with a period less than some appropriately chosen limit.

To find these low-period orbits for the Rössler attractor, we initialized an uncoupled oscillator with random initial conditions, waited for it to settle onto the attractor, then recorded its orbits for some suitable length of time at high temporal precision. We then noted each piercing of the surface of section $u = 0$ in the positive-u direction ($\dot{u} > 0$). To a high degree of approximation, the (v, w) coordinates of these points were found to lie a curve, thus suggesting that it is possible to reduce the three-dimensional flow to a one-dimensional map. We then plotted $v(i + n)$ vs. $v(i)$; that is, the v coordinate of the $(i + n)^{\text{th}}$ piercing versus the v coordinate of the ith. Each intersection of this curve with the line $v(i + n) = v(i)$ represents the

v coordinate of an initial condition for an orbit that starts on the surface of section and returns to its original position after n piercing of the surface of section. With two coordinates (namely u and v) known, all that remains is to find the value of w such that $(0, v, w)$ lies on the attractor.

Of course, for $n > 1$, many of these intersections will be redundant, as every period n orbit pierces the surface of section n times, thus producing n intersections on the curve. In addition, each curve will have intersections corresponding to orbits of any period that is a factor of n. As an example, consider the curve $v(i + 4)$ vs. $v(i)$. The Rössler system used in this paper has three Period 4 orbits, one Period 2 orbit and one Period 1 orbit. Thus, the number of times $v(i + 4)$ vs. $v(i)$ will intersect $v(i + 4) = v(i)$ is $3 \times 4 + 1 \times 2 + 1 \times 1 = 15$.

As these orbits are inherently unstable, error accumulated through numerical integration can result in a trajectory leaving the periodic orbit after only a small number of periods. Thus, for the long term computation of Lyapunov exponents to obtain the master stability function, it is advisable to compute the trajectory for only a single period, then return the oscillator to its initial position (u, v, w), and repeat as often as needed.

Bibliography

[1] S. Boccaletti, V. Latora, Y. Moreno, M. Charles, D.-U. Wang, "Complex networks: Structure and dynamics," Phys. Rpts. **424**,175 (2006).

[2] A.E. Motter, M.A. Matias, J. Kurths and E. Ott, "Dynamics on Complex Networks and Applications," Physica D **224**, vii (2006).

[3] Y. Kuramoto in *International Symposium on Mathematrical Problems in Theoretical Physics*, Lecture Notes in Physics, edited by H. Araki (Springer-Verlag, Berlin 1975), vol. 39.

[4] Y. Kuramoto, *Chemical Oscillators, Waves and Turbulence* (Springer, New York, 1984).

[5] S.H. Strogatz, "From Kuramoto to Crawford: exploring the onset of synchronization in populations of coupled oscillators," Physica D **143**, 1 (2000).

[6] E. Ott, *Chaos in Dynamical Systems* (Cambridge University Press, second edition, 2002).

[7] J.A. Acebron, L.L. Bonilla, C.J.P. Cincente, R. Ritort and R. Spigler, "The Kuramoto model: A simple paradigm for synchronization phenomena," Rev. Mod. Phys. **77**, 137 (2005).

[8] E. Ott and T.M. Antonsen, "Low dimensional behavior of large systems of globally coupled oscillators," Chaos **18**, 037113 (2008).

[9] E. Ott and T.M. Antonsen, "Long time evolution of phase oscillator systems," Chaos **19**, 023117 (2009).

[10] J. Stout, M. Whiteway, E. Ott, M. Girvan and T.M. Antonsen, "Local synchronization in complex networks of coupled oscillators," Chaos **21**, 025109 (2011).

[11] J. Gomez-Gandeñes, Y. Moreno and A. Arenas, "From scale-free to Erdos-Rnyi networks," Phys. Rev. E **73**, 056124 (2006).

[12] M. Brede, "Locals vs. global synchronization in networks of non-identical Kuramoto oscillators," Eur. Phys. J. B **62**, 87 (2008).

[13] J.G. Restrepo, E. Ott and B.R. Hunt, "Onset of synchronization in large networks of coupled oscillators," Phys. Rev. E **71**, 036151 (2005); Physica D **224**, 114 (2006).

[14] T. Ichimoiya, "Frequency synchronization in a random oscillator network," Phys. Rev. E **70**, 026116 (2004).

[15] L. M. Alonso, J.A. Allende and G.B. Mindlen, "Dynamical origin of complex motor patterns," Eur. Phys. J. D **60**, 361 (2010).

[16] A. Ghosh, D. Roy and V.K. Jirsa, "Simple model for bursting dynamics of neurons," Phys. Rev. E **80**, 041930 (2009).

[17] M.M. Abduelreheme and E. Ott, "Low dimensional description of pedestrian-induced oscillation of the Millennium Bridge," Chaos **19**, 013129 (2009).

[18] L.M. Childs and S.H. Strogatz, "Stability diagram for the forced Kuramoto model," Chaos **18**, 043128 (2008).

[19] S.A. Marvel and S.H. Strogatz, "Invariant submanifold for series arrays of Josephson junctions," Chaos **19**, 013132 (2009).

[20] L.F. Lafuerza, P. Colet and R. Toral, "Nonuniversal Results Induced by Diversity Distribution in Coupled Excitable Systems," Phys. Rev. Lett. **105**, 084101 (2010).

[21] K.H. Nagai and H. Kori, "Noise-induced synchronization of a large population of globally coupled nonidentical oscillators," Phys. Rev. E **81**, 065202 (2010).

[22] E.A. Martens, E. Barreto, S.H. Strogatz, E. Ott, P. So and T.M. Antonsen, "Exact results for the Kuramoto model with a bimodal frequency distribution," Phys. Rev. E **79**, 026204 (2009).

[23] D. Pazó and E. Montbrió, "Existence of hysteresis in the Kuramoto model with bimodal frequency distributions," Phys. Rev. E 80, 046215 (2009).

[24] W.S. Lee, E. Ott and T.M. Antonsen, "Large Coupled Oscillator Systems with Heterogeneous Interaction Delays," Phys. Rev. Lett. **103**, 044101 (2009).

[25] Z. Levajic and A. Pikovsky, "Phase resetting of collective rhythm in ensembles of oscillators," Phys. Rev. E **82**, 056202 (2010).

[26] P. So, B.C. Cotton and E. Barretto, "Synchronization in interacting populations of heterogeneous oscillators with time-varying coupling," Chaos **18**, 037114 (2008).

[27] Y. Kawamura, H. Nakao, K. Arai, H. Kori and Y. Kuramoto, "Phase synchronization between collective rhythms of globally coupled oscillator groups: Noiseless nonidentical case," Chaos **20**, 043110 (2010).

[28] A. Pikovsky and M. Rosenblum, "Partially Integrable Dynamics of Hierarchical Populations of Coupled Oscillators," Phys. Rev. Lett. **101**, 264103 (2008).

[29] C.R. Lang, "Chimera states in heterogeneous networks," Chaos **19**, 013113 (2009).

[30] C.R. Laing, "The dynamics of chimera states in heterogeneous Kuramoto networks," Physica D **238**, 1569 (2009).

[31] E.A. Martens, "Bistable chimera attractors on a triangular network of oscillator populations," Phys. Rev. E **82**, 016216 (2010).

[32] G. Borydugov, A. Pikovsky and M. Rosenblum, "Self-emerging and turbulent chimeras in oscillator chains," Phys. Rev. E **82**, 035205 (2010).

[33] E.A. Martens, "Chimeras in a network of three oscillator populations with varying network topology," Chaos **20**, 043122 (2010).

[34] M.E.J. Newman, "The Structure and Function of Complex Networks" SIAM Review **45**, 167 (2003) Sec. 4.2.1.

[35] J.G. Restrepo, E. Ott and B.R. Hunt, "Approximating the largest eigenvalue of network adjacency matrices," Phys. Rev. E **76**, 056119 (2007).

[36] S. Chauhan, M. Girvan, E. Ott, "Spectral properties of networks with community structure," Phys. Rev. E 80, 056114 (2009).

[37] L. Pecora and T. L. Carroll, "Master Stability Functions for Synchronized Coupled Systems," Phys. Rev. Lett. 80, 2109 (1998).

[38] H. Fujisaka and T. Yamada, "Stability Theory of Synchronized Motion in Coupled-Oscillator Systems," Prog. Theor. Phys. **69**, 32 (1983).

[39] In Fig. 2.10 we have omitted a curve on which there is a transcritical bifurcation from one fixed point to another (*i.e.*, an interchange of stability and instability as the two fixed points pass through each other). In this case there is a single SS attractor on *both* sides of the bifurcation. The omitted bifurcation curve is a 90° arc of the radious one circle centered at $(\tilde{\omega}_0, \tilde{\Delta}) = (0, 1)$ and extends from point c to the origin.

[40] A simulation length of $2,000$ time units (with time averaging done over the last $1,000$ units) is far more than is usually required. It was usually sufficient to run the simulations for 500 time units with time averaging done over the last 100 units. The overly long simulations were done to ensure maximum accuracy.

[41] M.I. Freidlin, A.D. Wentzell and J. Szucs, *Random Perturbations of Dynamical Systems* (Springer-Verlag, New York, 1998).

[42] T. M. Antonsen, Jr., R. T. Faghih, M. Girvan, E. Ott and J. Platig, "External periodic driving of large systems of globally coupled phase oscillators" Chaos **18** 037112 (2008).

[43] G. Barlev, M. Girvan and E. Ott, "Map model for synchronization of systems of many coupled oscillators," Chaos **20**, 023109 (2010).

[44] O. Popovych, Y. Maistrenko, P. Tass, "Phase chaos in coupled oscillators," Phys. Rev. E **71**, 065201 (2005).

[45] M. Wolfrum, O. Omel'chenko, "Chimera states are chaotic transients," Phys. Rev. E **84**, 015201 (2011).

[46] I. Shimada and T. Nagashima, "A numerical approach to ergodic problem of dissipative dynamical systems," Prog. Theoret. Phys. **61**, 1605 (1979).

[47] K. Ramasubramanian and M.S. Sriram, "A comparative study of computation of Lyapunov spectra with different algorithms," Physica D **139** 72 (2000).

[48] QR decomposition was performed using the LAPACK routine `xGEQR2P`, which uses Householder reflections while guaranteeing positive entries for the diagonal terms of the matrix R. See J. Demmel, M. Hoemmen, Y. Hida and E.J. Riedy,

"Nonnegative Diagonals and High Performance on Low-Profile Matrices from Householder QR," SIAM Journal on Scientific Computing, **31** 2832 (2009).

[49] We have reproduced the results of Ref. [44] using our Lyapunov exponent computation code. Thus, the difference between our results and those of Ref. [44] are not due to coding differences, but rather reflect the different situations treated.

[50] The single oscillator hypothesis presents a small problem: it overdescribes the system by one vector, since there are N oscillators which should each have a corresponding Lyapunov vector $\vec{v}_j^{SOH}$, but there is also the rotation vector $\vec{v}_0$, specified by Eq. (3.12). From a practical perspective, the issue is moot due to the degeneracy of the Lyapunov spectrum: for small values of k, there are multiple predicted Lyapunov exponents extremely near zero, any one of which could be "missing," and at large k, the Lyapunov vectors converge to h_∞ (Eq. (3.21)) so closely that they are nearly degenerate.

[51] V. S. Afraimovich, N. N. Verichev, and M. I. Rabinovich, "Stochastic synchronization of oscillations in dissipative systems," Inv. VUZ Radiofiz. RPQAEC **29**, 795 (1986).

[52] K. M. Cuomo and A. V. Oppenheim, "Circuit implementation of synchronized chaos with applications to communications," Phys. Rev. Lett. **71**, 65 (1993).

[53] A. Argyris, M. Hamacher, K. E. Chlouverakis, A. Bogris, and D. Syvridis, "Photonic Integrated Device for Chaos Applications in Communications," Phys. Rev. Lett. **100**, 194101 (2008).

[54] M. Feki, "An adaptive chaos synchronization scheme applied to secure communication," Chaos, Solitons and Fractals **18**, 141 (2003).

[55] H. D. I. Abarbanel, D. R. Creveling, and J. M. Jeanne, "Estimation of parameters in nonlinear systems using balanced synchronization," Phys. Rev. E **77**, 016208 (2008).

[56] D. R. Creveling, P. E. Gill, and H. D. I. Abarbanel, "State and parameter estimation in nonlinear systems as an optimal tracking problem," Phys. Lett. A **372**, 2640 (2008).

[57] J. C. Quinn, P. H. Bryant, D. R. Creveling, S. R. Klein, and H. D. I. Abarbanel, "Parameter and state estimation of experimental chaotic systems using synchronization," Phys. Rev. E **80**, 016201 (2009).

[58] F. Sorrentino and E. Ott, "Using synchronization of chaos to identify the dynamics of unknown systems," Chaos **19**, 033108 (2009a).

[59] P. So, E. Ott, and W. P. Dayawansa, "Observing chaos: Deducing and tracking the state of a chaotic system from limited observation," Phys. Rev. E **49**, 2650 (1994).

[60] G. S. Duane, J. J. Tribbia, and J. B. Weiss, "Synchronicity in predictive modelling: a new view of data assimilation," Nonlinear processes in Geophysics **13**, 601 (2006).

[61] F. Sorrentino and E. Ott, "Using synchronism of chaos for adaptive learning of time-evolving network topology," Phys. Rev. E **79**, 016201 (2009b).

[62] S. Hayes, C. Grebogi, and E. Ott, "Communicating with chaos," Phys. Rev. Lett. **70**, 3031 (1993).

[63] V. Dronov, M. Hendrey, T. M. Antonsen, and E. Ott, "Communication with a chaotic traveling wave tube microwave generator," Chaos **14**, 30 (2004).

[64] L. S. Tsimring and M. M. Sushchik, "Multiplexing chaotic signals using syncrhonization," Phys. Lett. A **213**, 155 (1996).

[65] N. Sharma and E. Ott, "Exploiting synchronization to combat channel distortions in communication with chaotic systems," Int. J. Bif. Chaos **10**, 777 (2000).

[66] F. Sorrentino and E. Ott, "Adaptive Synchronization of Dynamics on Evolving Complex Networks," Phys. Rev. Lett. **100**, 114101 (2008).

[67] B. Ravoori, A. B. Cohen, A. V. Setty, F. Sorrentino, T. E. Murphy, E. Ott, and R. Roy, "Adaptive synchronization of coupled chaotic oscillators," arXiv:0907.3894 (2009).

[68] F. Mossayebi, H. K. Qammar, and T. T. Hartley, "Adaptive estimation and synchronization of chaotic systems," Phys. Lett. A **161**, 255 (1991).

[69] C. R. Johnson Jr. and J. S. Thorp, "An adaptive calibration algorithm for synchronized chaos," IEEE Sig. Proc. Lett. **1**, 194 (1994).

[70] U. Parlitz and L. Kocarev, "Multichannel communication using autosynchronization," Int. J. Bif. Chaos **6**, 581 (1996).

[71] C. W. Wu, T. Yang, and L. O. Chua, "On adaptive synchronization and control of nonlinear dynamical systems," Int. J. Bif. Chaos **6**, 455 (1996).

[72] L. O. Chua, T. Yang, G.-Q. Zhong, and C. W. Wu, "Adaptive synchronization of Chua's oscillators," Int. J. Bif. Chaos **6**, 189 (1996).

[73] M. di Bernardo, "An adaptive approach to the control and synchronization of continuous-time chaotic systems," Int. J. Bif. Chaos **6**, 557 (1996).

[74] D. J. Sobiski and J. S. Thorp, "PDMA-1: chaotic communication via the extended Kalman filter," IEEE Trans. Circ. Syst. I **45**, 194 (1998).

[75] T.-L. Liao, "Adaptive syncrhonization of two Lorenz systems," Chaos Solitons Fractals **9**, 1555 (1998).

[76] C. Zhou and J. Kurths, "Dynamical weights and enhanced syncrhonization in adaptive complex networks," Phys. Rev. Lett. **96**, 164102 (2006).

[77] P. De Lellis, M. di Bernardo, and F. Garofalo, "Synchronization of complex networks through local adaptive coupling," Chaos **18**, 037110 (2008).

[78] P. Ashwin, J. Buescu, and I. N. Stewart, "Bubbling of attractors and synchronisation of chaotic oscillators," Phys. Lett. A **193**, 126 (1994a).

[79] P. Ashwin, J. Buescu, and I. N. Stewart, "From attractor to chaotic saddle: a tale of transverse instability," Nonlinearity **9**, 703 (1994b).

[80] S. C. Venkataramani, B. R. Hunt, and E. Ott, "Bubbling transition," Phys. Rev. E **54**, 1346 (1996).

[81] In addition, to desynchronism bursts, it is also possible that a large desynchronization orbit event can result in capture of the system orbit on a desynchronized attractor with a so-called riddled basin of attraction (e.g., see Refs. [6,78–80,89]). This possibility, although a typical occurrence in such situations, did not manifest itself in the particular system used for our numerical studies in Sec. IV. Thus we, henceforth, restrict our discussion to the case that bubbling is associated with bursts.

[82] B. R. Hunt and E. Ott, "Optimal periodic orbits of chaotic systems," Phys. Rev. Lett. **76**, 2254 (1996).

[83] J. G. Restrepo, E. Ott, and B. R. Hunt, "Spatial patterns of desynchronization bursts in networks," Phys. Rev. E **69**, 066215 (2004).

[84] M. Barahona and L. Pecora, "Synchronization in small-world systems," Phys. Rev. Lett. **89**, 054101 (2002).

[85] T. Nishikawa, A. Motter, Y. Lai, and F. Hoppensteadt, "Heterogeneity in oscillator networks: are smaller worlds easier to synchronize?," Phys. Rev. Lett. **91**, 014101 (2003).

[86] M. Chavez, D. Huang, A. Amann, H. Hentschel, and S. Boccaletti, "Synchronization is enhanced in weighted complex networks," Phys. Rev. Lett. **94**, 218701 (2005).

[87] D. Hwang, M. Chavez, A. Amann, and S. Boccaletti, "Synchronization in complex networks with age ordering," Phys. Rev. Lett. **94**, 138701 (2005).

[88] F. Sorrentino, M. di Bernardo, F. Garofalo, and G. Chen, "Controllability of complex networks via pinning," Phys. Rev. E **75**, 046103 (2007).

[89] E. Ott and J. C. Sommerer, "Blowout bifurcations: the occurrence of riddled basins and on-off intermittency," Phys. Lett. A **188**, 39 (1994).